Athermal Optical Phased Array

Constantine Papakonstantinou

A Thesis Submitted to the Faculty of Graduate Studies

In Partial Fulfillment of the Requirements

for the Degree of Master of Science

Graduate Program in Earth and Space

York University

Toronto, Ontario

December 2024

©Constantine Papakonstantinou, 2024

Abstract

Optical phased arrays (OPA) are of growing interest in free space communication systems due to the need for high speed communication. Generally, design of OPAs using the Silicon On Insulator (SOI) platform will rely on the thermo-optic (TO) effect to tune the refractive index, thereby controlling the phase in each channel. However this makes the design sensitive to parasitic heat, and thermal cross-talk at scale. Instead of using thermal control, thermal tolerance is introduced by reducing the TO effect, and leveraging the electro-optic (EO) effect in lieu. Metamaterial techniques for the athermal design of optical waveguides and subwavelength structures are presented for the application of designing an OPA feed network. The design of compact and athermal grating antennas suitable for OPA configurations is also explored.

Acknowledgement

No satellite, perhaps no complex system, is solely dreamed of, designed, and executed only by the direct experience and work of a single mind. In academics and in profession; there are mentors, champions, colleagues and shoulders of giants. This forward is a recognition of gratitude for the community that created the opportunity for this work to exist. Thank you to my supervisor Dr. Regina Lee, for the opportunity to pursue graduate studies. As a graduate student I have valued the freedom to explore ideas, the time and resources to prove them, and the eventual contribution of those ideas that may inspire new minds. Thank you to CMC Microsystems and the SiEPIC program for the training and access to fabrication services that facilitated this research. A final thank you to my wife, Vanessa, who with love supported me in realizing this dream of completing a graduate degree.

Contents

List of Tables

List of Figures

List of Acronyms

AMF Advanced Micro Foundry

ANT Advanced Nano Tools

ASE Amplified Spontaneous Emission

CLI Command Line Interface

CMC Canadian Microelectronics Corporation

CMT Coupled Mode Theory

DAC Digital-to-Analog Converter

DC Duty Cycle

EDRS European Data Relay System

EME Eigenmode Expansion

EMT Effective Medium Theory

ESA European Space Agency

EO Electro-Optic

FDE Finite Difference Eigenmode

FDTD Finite Difference Time Domain

FOV Field of View

GNSS Global Navigation Satellite System

IP Intellectual Property

IR Infrared

ISL Intersatellite Links

JAXA Japan Aerospace Exploration Agency

JDRS Japanese Optical Data Relay System

LCRD Laser Communication Relay Demonstration

LD Laser Diode

LEO Low Earth Orbit

LO Local Oscillator

MMI Multi-Mode Interferometer

MPW Multi Project Wafer

MZI Mach-Zehnder Interferometer

NASA National Aeronautics and Space Administration

OCSD Optical Communications and Sensors Demonstration

OISL Optical Intersatellite Links

OPA Optical Phased Array

PDK Process Design Kit

PIN P-doped, Intrinsic, N-doped semiconductor

PM Polarization Maintaining

PML Perfectly Matched Layer

RF Radio Frequency

RIN Relative Intensity Noise

SiEPIC Silicon Electronic-Photonic Integrated Circuits

SIN Silicon Nitride

SOI Silicon on Insulator

SWG Subwavelength Waveguides

TE Transverse Electric

TEM Transverse Electromagnetic

TFLN Thin-Film Lithium Niobate

TM Transverse Magnetic

TMM Transfer Matrix Method

TO Thermo-Optic

TOC Thermo-Optic Coefficient

UV Ultraviolet

WDM Wavelength Division Multiplexing

List of Symbols

Symbol	Definition
$\int_S \, dS$	Integral of a surface with surface element dS
$\int_V \, dV$	Integral of a volume with volume element dV
AF	Array Factor
$\vec{H}$	Magnetic Field
C	Coupling coefficient
C_{TE}	Thermal expansion coefficient
DC	Grating duty cycle
$\vec{E}$	Electric Field
E_{eg}	Excitonic band gap
Γ	Mode Confinement
L	Length of a waveguide
Λ	Grating pitch
M	Diffraction order
N_e	Number of electrons
N_h	Number of holes
P_S	Power of the signal
P_{LO}	Power of the local oscillator
R	Responsivity of photodetector
T	Temperature
V_π	Modulation efficiency
W	Energy Density
W_1	Grating high index width
W_2	Grating low index width
a	Grating length - high index region
b	Grating length - low index region
d	Pitch of the array
k_0	Free space wave vector

Symbol	Definition
n	Refraction coefficient
n_{eff}	Effective refractive index
$\bar{n}$	Complex refractive index
v_p	Phase velocity
y_{wg}	Waveguide width
z_r	Interface roughness
z_{wg}	Waveguide thickness
α	Absorption coefficient
β	Propagation/Phase Coefficient
ε	Relative permittivity
μ	Permeability
κ	Extinction coefficient
λ	Wavelength
λ_0	Free space wavelength
ω	Angular frequency
ω_0	Free space angular frequency

1 Introduction

1.1 Intersatellite Links

Intersatellite Links (ISL) are used commonly in the space communication infrastructure, traditionally Radio Frequency (RF) bands are used for free space communication[1]. However, optical links are an established topic of research [2] and the advantages of optical links are well known. For example,Sebacher, Lambert, Pautler, *et al.* analyzed laser Optical Intersatellite Links (OISL) noting distinct theoretical advantages [3]. For example increase of data rate, which is expected due to larger bandwidths in the optical spectrum. As well as jamming immunity due to narrow beam widths and small receiving Field of View (FOV). Marshalek, Mecherle, and Jordan note implementation advantages for optical links in the areas of aperture size, terminal weight and recurring cost [4]. While Williams, Collins, Boroson, *et al.* predict the advantage of lower power consumption [5]. Recently, optical technology has matured and optical links are moving from research to application to realize the theoretical advantages [6], [7] such as broad bandwidths, interference immunity and unregulated spectrum. Similar survey literature shows that missions are trending towards implementing satellite communication links in the optical spectrum [8]–[10].

OISLs leveraging laser communication terminals are currently being used by major space agencies, having passed the barrier from research to practical application. The European Space Agency (ESA) European Data Relay System (EDRS) [11] is active with demonstration of the Sentinel satellites [12]. The Japan Aerospace Exploration Agency (JAXA) Japanese Optical Data Relay System (JDRS) [13] is also active with successful demonstrations of the ALOS satellites [14], [15]. Significant advances have also been made in the area of space-to-ground links. For example the National Aeronautics and Space Administration (NASA) Optical Communications and Sensors Demonstration (OCSD) program successfully demonstrated optical downlink with a cubesat platform [16]. While NASA's Laser Communication Relay Demonstration (LCRD) program [17] is successfully using optical terminals [18] with planned use cases of space-to-space links and space-to-ground links. OISL is being proposed for next generation Global Navigation Satellite System (GNSS) [19]–[21]. With the OISL design actively being demonstrated in laboratory [22]. There are a number of ventures using constellations of OISL [23], [24] for applications like internet in space. For example in 2024 the Toronto-based Kepler satellite system [25] has

moved over a terabyte of data using optical terminals in a system of Low Earth Orbit (LEO) satellites[26], [27]. While also in 2024, SpaceX's starlink constellation had nearly 6000 satellites in orbit [28] using OISL [29]. Telesat's Lightspeed constellation [30] is planned to launch in 2026 [31].

Toyoshima reviewed trends and noted the exhaustion of RF channels as well as increasing data rate requirements in time [6]. These issues are shown to be addressed by optical links. As OISL have higher data rate capacities, and less channel restrictions due to being in unregulated communication bands. However, OISLs generally require higher pointing accuracy requirements due to the narrower radiation beam widths and receiving FOV [32], [33]. One method for control of pointing a laser terminal is the use of gimbals, for example Iwamoto, Nakao, Ito, *et al.* propose the use of small gimbals to achieve the pointing requirements [34]. Similarly, Carrizo, Knapek, Horwath, *et al.* have a coarse pointing assembly embedded in their optical terminal design [24]. However Optical Phased Array (OPA)s can be used in lieu of Gimbals [35] as OPAs are an alternate means of addressing control of pointing for optical links and are superior in terms of size and weight. As phased arrays can be pointed electronically without the need for external mechanics.

1.2 Optical Phased Arrays

Silicon on Insulator (SOI) is a material platform currently being explored for the realization of OPAs [35]–[44]. These phase sensitive silicon photonic systems require active or passive suppression of unintended thermal heating because of the large Thermo-Optic (TO) effect in silicon. In particular, the capability of an OPA to control the emitted beam shape depends on the precision of phase control on each emitter in its feed network. Since phase control is associated with heating in silicon, thermal management is often part of OPA design. Both active and passive techniques for mitigation of thermal transients were reviewed by Yepez et al. [45], [46].

Yepez et al. compare the the addition of mechanical structures such as air trenches, or vias and heat shunts into the substrate for thermal management of the photonic circuit, and specifically for OPAs. Yepez et al. in studying air trenches and heat shunts [46] note there is a trade off for air trenches. The reduction in cross talk distances, and the improvements in heat dissipation compete and are related to the trench depth. Heat shunts are proposed as a mean to improve heat dissipation. They conclude an order of magnitude reduction in the distance at which temperature rise is limited to a safe distance using this scheme compared with

non-trenched chips.

Yepez et al. in studying heat shields made of vias [45] concluded that typical modulator-to-modulator distances of 20 μm could be reduced to 3 μm by the use of vias for heat distribution without significantly changing the cross talk. The associated change in the temperature gradient across the waveguides with this scheme was similarly reduced by an order of magnitude, with the same scale in reduction of the phase error due to cross talk.

Other realizations of similar enhancements are present in recent literature. For example, Wang, Liang, Chen, *et al.* [47] demonstrated the combined use of graphene to improve dispersion of heat in the substrate, and air trenches to thermally isolate the OPA elements. Wang et al. present a design with negligable cross talk at 10 μm waveguide pitch. At 3 μm with air trenches, the temperature gradient is comparable with the results from Yepez et al. [45].

Ostensibly, thermal management for OPAs has been associated strongly to temperature control [45]–[47]. Thermal management is often focused on solving thermal control challenges in the system design [39], [48], [49]. However, few literature discusses reducing the thermal sensitivity of an OPA by means of changing the Thermo-Optic Coefficient (TOC) [50]. For example Lee, Jin, Chun, *et al.* [50] design an OPA using Silicon Nitride (SIN) for the device layer due to its lower TOC compared with silicon. While no literature to this authors knowledge discusses reducing the thermal sensitivity of an OPA using a silicon device and athermal design methods which leverage the cladding.

Athermal photonic designs with silicon are possible, for example, the TO effect in a silicon waveguide can be countered by a polymer cladding [51]–[54]. This concept can be extended to more complicated photonic systems with a network of silicon waveguides. Podmore, Scott, Cheben, *et al.* passively stabilized a spectrometer from thermo-optic effects [55] using the same polymer cladding used by Schmid et al. [52], [53] and Ibrahim, Schmid, Aleali, *et al.* [54] in their demonstration of athermal subwavelength waveguides. For a phase modulated device such as an OPA, athermal waveguides imposes a restriction on the ability to use the TO effect for phase modulation, as phase modulation depends on dynamically adjusting the refractive index. With reduction of the TOC in a waveguide, care must be taken to design the phase modulator as the TO effect may no longer be viable. For example Lee, Jin, Chun, *et al.* heterogeneously integrate polymer waveguides for the heaters to account for the low TOC of their OPA [50]. While Lee,

Kwon, Kim, *et al.* are able to use Electro-Optic (EO) modulators with an SIN platform by heterogeneously integrating Thin-Film Lithium Niobate (TFLN) [56]. With athermal waveguides, phase modulation may still be achieved by use of the EO effect [57] and many OPA designs feature EO phase shifters [58] [43].

There is a gap in literature for OPA designs. To the best of the authors knowledge, the combined use of athermal SOI waveguides with EO phase shifters to realize a phase stable OPA in the presence of thermal fluctuations remains undemonstrated.

1.3 Research Objectives

The implementation OISL is challenging as satellite communication systems require strict pointing requirements; while in a vibrating [32], [33], [59] and thermally changing environment. The thermal range over an orbit is typically stabilized in a range aligned with industrial and military grade electronic survival limits [60]. Using an OPA implemented on SOI as an OISL technology in such a temperature range risks loss of pointing during a temperature slew if temperature is not actively controlled at the silicon device layer.

The allowable pointing disturbance for a constellation of LEO satellites with OISLs is not a general value, it is a specific value determined by the link budget parameters for the constellation. However, it can be inferred from case studies what order of magnitude modern LEO systems such as SpaceX Starlink or Telesat Lightspeed require. For example Carrizo, Knapek, Horwath, *et al.* cite the alignment and tracking stability of their optical terminals as 1 μrad. Which is 1 order of magnitude less than their beam divergence [24]. While Iwamoto, Nakao, Ito, *et al.* designed their link with an acceptable disturbance of 10 μrad, which is also an order of magnitude less than their beam divergence [34].

While control techniques are possible to account for environmental state change [61]. The goal of the following research is the exploratory design of an OPA capable of operating within a thermally changing environment without loss of pointing due to disruption of phase in the array channels. This was partially achieved by making design consideration for the thermal sensitivity of the phased array architecture at the systems level, i.e. by using optical phase symmetry. Additionally by making considerations for the thermal sensitivity at the component level, i.e. such as design of waveguides and antennas. See Section 2.

In this work, polymer cladded waveguides were used to reduce the TOC with respect to silicon, thus reducing the temperature sensitivity when temperature change across the channels is not symmetric. Lateral PIN junctions were used for phase modulation via the EO effect. The Intellectual Property (IP) for the modulator designs was released by Canadian Microelectronics Corporation (CMC) and the Silicon Electronic-Photonic Integrated Circuits (SiEPIC) program. Finally, the optical phase symmetry for linear arrays was exploited to reduce temperature sensitivity when the temperature change across the channels is symmetric.

1.4 Research Contributions

This research explored the athermal design of waveguides by means of using a polymer with a positive TOC for the cladding of an SOI OPA with open-oxide specification over the waveguides. The use of the cladding in SOI for the purpose of designing athermal waveguides has been thoroughly demonstrated in literature [51]–[54], [62]–[64]. However, for subwavelength waveguides, no extension of the confinment model from Ye, Michel, and Kimerling [51] is derived for periodic structures such as Bragg gratings. A semi-analytic expression inspired by Effective Medium Theory (EMT) was derived for Bragg gratings and was consistent with Finite Difference Time Domain (FDTD) simulations [65]. Details of this derivation are repeated in section 3.2. This technique was applied to the design of optical antennas based on gratings, demonstrating increased bandwidth in optical antennas compared with a reference SOI design; shown in Section 4.3.

An SOI OPA was fabricated with lateral PIN junctions for phase modulation, this has also been thoroughly demonstrated in literature [41], [43], [58], [66]. However, to the best of our knowledge, not with the combined use of athermal waveguides. The addition of such waveguides in this work reduced the temperature sensitivity of the OPA by an order of magnitude with respect to SOI. To the best of our knowledge, passively thermally stabilized OPAs were not previously demonstrated in literature. Thermal tolerance of designs in literature focuses on control of thermal effects through thermal dispersion and isolation [45]–[47]. The design and test of this device is presented in Sections 3.3 and 5.

2 Theory and Modelling

2.1 Refractive index

The refractive index of a material is a fundamental parameter for optical component design. A full account of the modelling of the refractive index is available from Ghosh [67]. Modern database distribution of refractive index data is also readily available from Polyanskiy [68]. Fundamentally, the complex refractive index, by its real and imaginary parts describe the delay and attenuation of the medium respectively [67].

$$\bar{n} = n + i\kappa \tag{2.1}$$

$$\alpha = \frac{4\pi\kappa}{\lambda} \tag{2.2}$$

$$\beta = n\, k_0 = \frac{2\pi n}{\lambda} \tag{2.3}$$

$$\varepsilon_r = (n^2 - \kappa^2) + i2n\kappa \tag{2.4}$$

The extinction coefficient, κ, defines the absorption and is related to the absorption coefficient, α, by the relation in Equation 2.2. The refraction coefficient, n, defines the delay and is related to the phase coefficient, β, by the relation in equation 2.3. It denotes the wave vector for refractive index of the material. The real and imaginary parts of the refractive index are directly related with the relative permittivity, ε_r, of the material; Equation 2.4. Substitutions of this type are often used to model electromagnetic materials, such as with Rytov's formula [69]. Commonly for non-magnetic materials the substitution can be simplified, $n^2 = \varepsilon$.

The variation of the refractive index with wavelength is referred to as dispersion. The dispersive relation of the refractive index is often captured by the Sellmeier coefficients [67]. The Sellmeier coefficient A

accounts for contributions to the refractive index for energies above the band gap. The coefficients B and C are associated with Ultraviolet (UV) absorptions, while the coefficients D and E are associated with Infrared (IR) absorption. Using Equation 2.5, is applicable between UV and near IR. Alternatively the Lorentz-Lorenz model [70], Equation 2.6, may be used consistently between many simulations tools [71].

$$n^2(\lambda) = A + \frac{B\lambda^2}{\lambda^2 - C} + \frac{D\lambda^2}{\lambda^2 - E} \tag{2.5}$$

$$n^2(\lambda) = \varepsilon + \frac{\varepsilon_{Lorentz}\omega_0^2}{\omega_0^2 - 2i\partial_0\omega - \omega^2} \tag{2.6}$$

The refractive index is not constant over temperature. The variation of the refractive index with temperature at constant pressure is called the Thermo-Optic Coefficient (TOC). The change in the refractive index with temperature may be modelled as constant over a limited temperature range. Generally, the TOC has a dispersive relationship to wavelength and temperature and is not constant. This is pronounced over temperature ranges on the order of hundreds of Kelvin. However, it can be assumed to be constant over small temperature intervals, up to tens of Kelvin. The approximate change in TOC with temperature interval about a reference temperature of 293K is based on Li[72], this data was used in this study to calculate the change in TOC shown in Table 2.

$$n(T) = n(T_0) + \frac{dn}{dT}\Delta T \tag{2.7}$$

$$2n\frac{dn}{dT} = (n^2 - 1)\left(-3C_{TE}R - \frac{1}{E_{eg}}\frac{dE_{eg}}{dT}R^2\right) \tag{2.8a}$$

$$2n\frac{dn}{dT} = GR + HR^2 \tag{2.8b}$$

To perform calculations that express the TOC as a function of temperature, Ghosh presents the dependencies of the TOC through Equation 2.8a. It relates the TOC with the thermal expansion coefficient,

C_{TE}, and the optical band gap, E_{eg}. Ghosh shows the possibility of the TOC to be negative or positive in magnitude is the competition of these two physical factors in the material. In Ghosh's model, Equation 2.8b, the parameter G is related to the thermal expansion coefficient, H is related to the temperature coefficient of the optical band gap, and R is the normalized dispersive wavelength.

Ghosh validates the modelling of the TOC with references to the canonical literature [67]. For example, Ghosh cites Li [72], who reviewed measurement data for the refractive index and TOC of silicon. The measurements cover, but are not limited to, optical telecom c-band and a temperature range of 100 - 750K. Ghosh's model for silicon is applicable to this data and the temperature ranges bound typical environmental conditions for Low Earth Orbit (LEO) satellites. Which is often in the range of electronic survival limits, -40 to +80C, or better.

$Interval\ (K)$	Average $\lvert\Delta(\frac{dn}{dT})\rvert$
293.0 ± 5.0	1.392e-06
293.0 ± 10.0	2.784e-06
293.0 ± 30.0	8.351e-06
293.0 ± 50.0	1.405e-05

Table 2: Average change in thermo-optic coefficient as a function of temperature interval.

2.2 Silicon On Insulator

2.2.1 Waveguides

Silicon photonics is typically implemented using Silicon on Insulator (SOI). SOI is a layered, composite material. The process for design of SOI devices is accounted by Chrostowski and Hochberg [71].Two refractive indices are available through this process and material stack n_1 = Si, $n_2 = SiO_2$. Oxide open designs have flexibility to introduce a material with a third refractive index but supplying n_3 is not a standard process from the foundry.

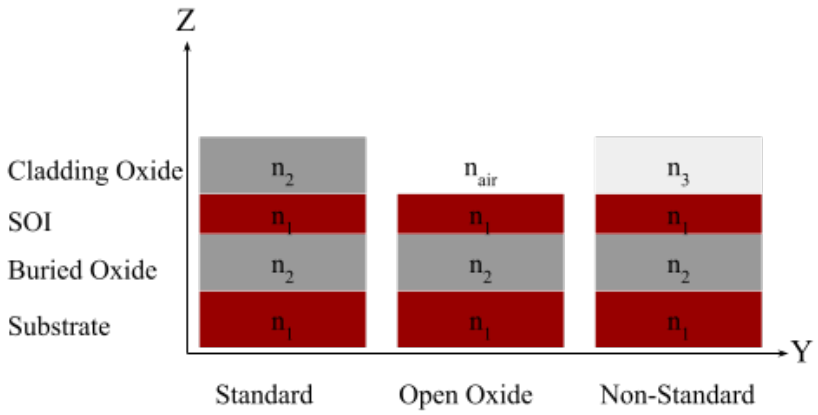

Figure 1: Silicon on Insulator material stack. n_1 is silicon and n_2 is silicon dioxide

Modifying the cladding by supplying a third material, n_3, will affect the properties of the optical waveguide. A modified cladding is shown in Figure 1. Waveguides will have some part of the electromagnetic field that propagates within the cladding layer. The material properties of the cladding thus have an effect on the resultant properties of the material stack. The refractive index may be engineered by either augmenting the material stack or waveguide geometry. The refractive index in a waveguide will depend on the waveguide geometry. As well as the material dispersion and operating temperature; due to wavelength and thermal dependencies of Silicon, respectively. The first order dependence of the materials at 1550 nm is shown in Table 3.

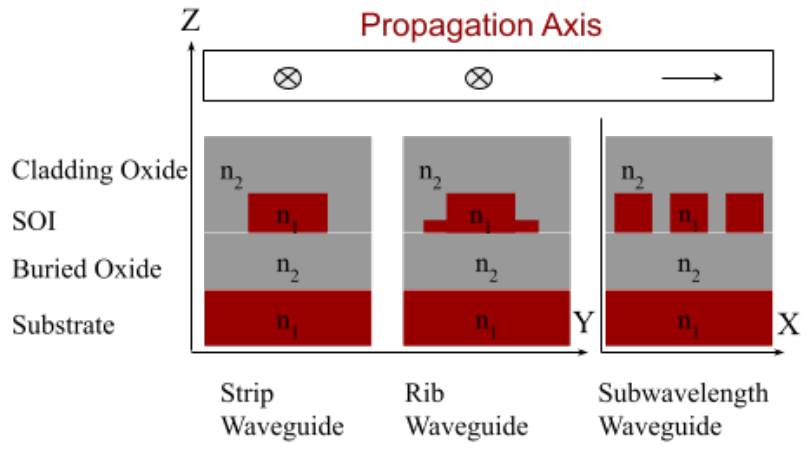

Figure 2: Waveguide geometries for silicon on insulator

n_i	$Material$	n_{eff}	$\frac{dn_{eff}}{d\lambda} nm^{-}1$	$\frac{dn_{eff}}{dT} K^{-}1$
n_1	Si	3.47	$-7.6E-5$	$1.81E-4$
n_2	SiO_2	1.44	$-1.2E-5$	$8.5E-6$

Table 3: First order material properties for silicon on insulator at $\lambda = 1550$ nm

2.2.2 Phase Modulation

For waveguides, the capability to control the optical phase is derived from the change in refractive index. Two conventional methods compatible with the SOI process are Thermo-Optic (TO) effect, or Electro-Optic (EO) effect. The primary figure of merit for phase shifting is the modulation efficiency $V_\pi L$. It describes the voltage length product of the phase shifter to achieve a π phase shift. Including the product of the change of the imaginary component of the refractive index, it also describes the loss efficiency $V_\pi L\alpha$. For broadband devices, operation bandwidth and data rate must also be considered as is natural for any other system component.

$$\Delta\phi(V) = \frac{2\pi}{\lambda}\Delta n_{eff}(V)L \tag{2.9a}$$

$$\pi = \frac{2\pi}{\lambda}\Delta n_{eff}(V_\pi)L \tag{2.9b}$$

$$\Delta n_{eff}(V_\pi) = \frac{dn_{eff}}{dV}V_\pi \tag{2.10}$$

$$V_\pi L = \frac{\lambda}{2\frac{dn_{eff}}{dV}} \tag{2.11}$$

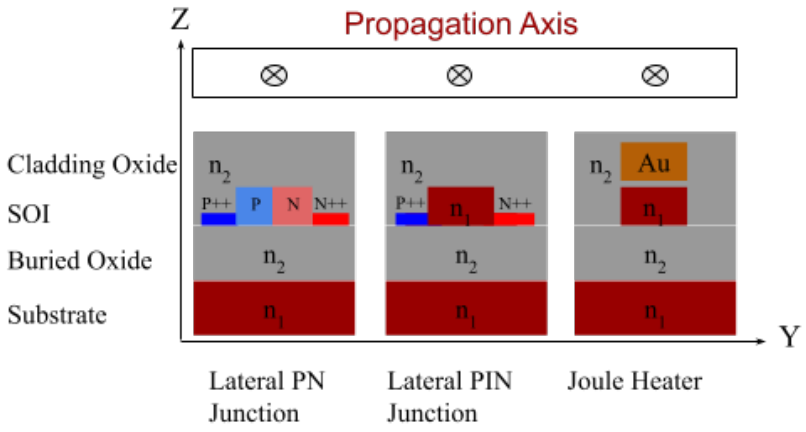

Figure 3: Phase shifter geometries

In Silicon, the TO effect can be modelled with the first order linear term because of the material dependence of Silicon, see Table 3. Silicon does not have a linear electro-optic (Pockels) effect due to its centrosymmetric crystal structure. Instead the implementation of the electro-optic effect in Silicon is hence done by use of the plasma dispersion effect in a semiconductor, which changes the density of the free carriers, and thus the real and imaginary parts of the refractive index. Soref and Bennett experimentally evaluated the absorption curves for the number of electrons (N_e) and holes (N_h) in the optical communication band [73] and produced empirical expressions which can be used in lieu of the Lorenz equations to obtain the change in refractive index and absorption coefficient. Such empirical models for the electro-refraction and electro-absorption were extended to broader IR ranges for silicon by Nedeljkovic, Soref, and Mashanovich [74]. The empirical relations from Soref and Bennett are sufficient at optical C-band with $\lambda = 1.55\mu m$.

$$\Delta n = -[8.8x10^{-22}\Delta N_e + 8.5x10^{-18}\Delta N_h^{0.8}] \tag{2.12}$$

$$\Delta\alpha = 8.5x10^{-18}\Delta N_e + 6.0x10^{-18}\Delta N_h \tag{2.13}$$

There are three primary ways in which manipulation of the free carriers is achieved for the electro-optic effect. Carrier accumulation, and carrier depletion are possible by the addition of a PN junction [57]. While

carrier injection is achieved by a PIN junction [57]. PN junctions have tuning speeds in the GHz range due to being gated by its resistance-capacitance time constant, and lengths in the mm range due to the carrier depletion being a weak effect. PIN junctions have tuning speeds in the MHz range due to being gated by carrier recombination life time, and lengths on the order of hundreds of micrometer due to carrier injection being a strong effect.

The PIN junction is operated in forward bias, or carrier injection mode. The PIN junction has a large depletion region already overlapping the optical mode at equilibrium and does not exhibit significant phase shift in reverse bias or carrier depletion mode. Thus, the optical mode will not be affected by additional carrier extraction with applied voltage. In forward bias, insignificant phase shifts are observed below the a threshold. A π phase shift is observed with relatively small voltages after threshold because of the large number of injected carriers. The large carrier injection also results in a greater loss.

In contrast TO effect can be achieved by either using an N-doped rib waveguide or by placing a conductive wire above the waveguide. Heaters have speeds in the kHz range due to being gated by its resistance-capacitance time constant, and short lengths in the range of hundreds micrometer due to joule heating being a strong effect.

2.3 Waveguide Mode

2.3.1 Maxwell's Equations

The advantage of SOI for photonics waveguides is the refractive index contrast between the silicon core and oxide regions. The index contrast confines light within the silicon layer, allowing it to be routed. The behaviour of light in such a medium is governed by Maxwell's equations. When assuming time-harmonic fields, Maxwell's equations are expressed in their complex form as shown in Equations 2.16a - 2.16d. Where J is the current density and ρ is the charge density. The permittivity and permeability of the materials are defined as in Equations (2.14). The relationship between the wave number in the material and its refractive index is given in Equation (2.15).

$$\varepsilon = \varepsilon_0 \varepsilon_r \tag{2.14a}$$

$$\mu = \mu_0 \mu_r \tag{2.14b}$$

$$k = k_0 n = \omega \sqrt{\varepsilon_0 \mu_0} \sqrt{\varepsilon_r \mu_r} \tag{2.15}$$

$$\nabla \cdot \vec{E} = \frac{\rho}{\varepsilon} \tag{2.16a}$$

$$\nabla \cdot \vec{H} = 0 \tag{2.16b}$$

$$\nabla \times \vec{E} = -i\omega\mu\vec{H} \tag{2.16c}$$

$$\nabla \times \vec{H} = i\omega\varepsilon\vec{E} + \vec{J} \tag{2.16d}$$

Maxwell's equations provide the framework to determine the electric field distributions for propagating waves. In the context of a waveguide, the boundary conditions applied to the media are the edges of the waveguide. The solutions to Maxwell's equations under these boundary conditions are known as the *modes* of the waveguide. As the solution of the waveguide can be expressed as a eigenvalue problem [75]–[79].

The boundary conditions for electromagnetic waves are expressed in Equations (2.17) following the description given by Kawano and Kitoh[77]. Where $\vec{E}_t, \vec{E}_n$ and $\vec{H}_t, \vec{H}_n$ are tangential and normal vectors of the electric and magnetic fields respectively, at the boundary of interfaces 1 and 2. If the material interface is perpendicular to the direction of propagation then the term tangential can be treated interchangeably with transverse.

$$\vec{E_{2t}} - \vec{E_{1t}} = 0 \tag{2.17a}$$

$$\varepsilon_2 \vec{E_{2n}} - \varepsilon_1 \vec{E_{1n}} = \sigma_s \tag{2.17b}$$

$$\vec{H_2} - \vec{H_1} = 0 \tag{2.17c}$$

$$\frac{1}{\mu_2}\vec{H_{2n}} - \frac{1}{\mu_1}\vec{H_{1n}} = J_s \tag{2.17d}$$

For describing the fields, Equations (2.17a) and Equation (2.17c) poses the constraints that the electric and magnetic field must be continuous across the interface, meaning there is no abrupt change in the component of the electric and magnetic fields that cross the interface. Equations (2.17b) and Equation (2.17d) poses the constraint that the normal component of the electric and magnetic fields may be described by the difference in permittivity and permeability of the materials that form the interface. The normal component of the electric and magnetic fields is not necessarily continuous. However, in the case of a dielectric waveguide, the surface charge density, σ_s, and surface current density J_s are assumed zero. The normal component of the electric and magnetic field may be continuous in these cases.

Obtaining the solutions to Maxwell's equations for a waveguide involves solving the wave equation. The wave equation for the electric field can be expressed by taking the curl of Equation (2.16c). Afterwards, applying the identity $\nabla \times \nabla \times \vec{E} = \nabla(\nabla \cdot \vec{E}) - \nabla^2 \vec{E}$. With the assumption $J_s = 0$ and substituting Equation (2.16d), the familiar form of the Helmholtz equation is obtained. Often expressed as function of the refractive index distribution, n(y,z), that defines the waveguide structure; Equation (2.18e).

$$\nabla \times \nabla \times \vec{E} = \nabla \times (i\omega\mu\vec{H}) \tag{2.18a}$$

$$\nabla(\nabla \cdot \vec{E}) - \nabla^2 \vec{E} = i\omega\mu(i\omega\varepsilon\vec{E} + \vec{J}) \tag{2.18b}$$

$$\nabla^2 \vec{E} + \omega^2 \mu\varepsilon\vec{E} = 0 \tag{2.18c}$$

$$\tag{2.18d}$$

$$\nabla^2 \vec{E}(y,z) + k_0^2 n^2(y,z)\vec{E}(y,z) = 0 \tag{2.18e}$$

Often used in solving problems related to Maxwell's equations are the following vector identities: Equation (2.19) and Gauss' theorem Equation (2.20). These general vector identities will be referred to later, and in the context of guided wave problems, they will often be applied over the transverse cross-section of the waveguide.

$$\nabla \cdot (\vec{E} \times \vec{H}) = \vec{H} \cdot (\nabla \times \vec{E}) - \vec{E} \cdot (\nabla \times \vec{H}) \tag{2.19}$$

$$\int_V \nabla \cdot \vec{A}\, dV = \oint_S \vec{A} \cdot d\vec{S} \tag{2.20}$$

2.3.2 Transverse Electric and Transverse Magnetic Modes

Waveguides are typically designed in the Transverse Electric (TE) or Transverse Magnetic (TM) format. The TE and TM conditions are modes where the normal component of the field is suppressed. While pure Transverse Electromagnetic (TEM) modes are possible for some waveguides, they may not supported by dielectric waveguides. Furthermore, in dielectric box waveguides, such as SOI strip waveguides, pure TE and TM modes may not exist. Although the transverse components of the fields dominate when referred to as TE or TM. Consider a hypothetical SOI slab waveguide infinite along the y-axis and oriented as in Figure 4. For a TE mode, the condition is required that $\vec{E}_x = 0$ as described in Table 4. Furthermore, with the SOI slab there is no variation along the transverse axis, $\frac{\partial}{\partial y} = 0$ per the boundary conditions. Maxwell's equations for the electromagnetic fields decouple in this case, as shown in Table 4.

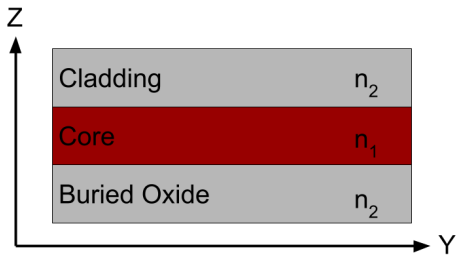

Figure 4: SOI slab waveguide.

Mode Type	Waveguide Type	$\vec{E}_x$	$\vec{E}_y$	$\vec{E}_z$	$\vec{H}_x$	$\vec{H}_y$	$\vec{H}_z$	Boundary Condition
TE	Slab	$=0$	$\neq 0$	$\neq 0$	$\neq 0$	$=0$	$\neq 0$	$\frac{\partial}{\partial y}=0$
TE	SOI Strip	≈ 0	$\neq 0$	≈ 0	$\neq 0$	≈ 0	$\neq 0$	$\frac{\partial}{\partial y}\neq 0$

Table 4: Field components for TE modes in SOI slab and strip waveguides, assuming x as the propagation direction.

To demonstrate this, consider Maxwells equations. Faraday's law, Equation (2.21) can be expanded into its partial derivative form, Equation (2.22). This expansion is treated similarly for Ampere's law, Equation (2.24). Setting the terms $\frac{\partial}{\partial y}=0$ for a slab waveguide decouples the field components. While in the case of an SOI strip waveguide, there are interfaces in both the y and z directions so the electric field must be continuous along the interface in both the y and z directions per the boundary conditions. In this case coupling can occur with each of the field components as the differential quantities are no longer separable.

$$\nabla \times \vec{E} = \begin{bmatrix} \hat{x} & \hat{y} & \hat{z} \\ \frac{\partial}{\partial x} & \frac{\partial}{\partial y} & \frac{\partial}{\partial z} \\ \vec{E}_x & \vec{E}_y & \vec{E}_z \end{bmatrix} \tag{2.21}$$

$$\nabla \times \vec{E} = \left(\frac{\partial \vec{E}_z}{\partial y} - \frac{\partial \vec{E}_y}{\partial z}\right)\hat{x} + \left(\frac{\partial \vec{E}_z}{\partial x} - \frac{\partial \vec{E}_x}{\partial z}\right)\hat{y} + \left(\frac{\partial \vec{E}_y}{\partial x} - \frac{\partial \vec{E}_x}{\partial y}\right)\hat{z} \tag{2.22}$$

$$\frac{\partial \vec{E}_z}{\partial y} - \frac{\partial \vec{E}_y}{\partial z} = -i\omega\mu\vec{H}_x \tag{2.23a}$$

$$\frac{\partial \vec{E}_z}{\partial x} - \frac{\partial \vec{E}_x}{\partial z} = -i\omega\mu\vec{H}_y \tag{2.23b}$$

$$\frac{\partial \vec{E}_y}{\partial x} - \frac{\partial \vec{E}_x}{\partial y} = -i\omega\mu\vec{H}_z \tag{2.23c}$$

$$\frac{\partial \vec{H}_z}{\partial y} - \frac{\partial \vec{H}_y}{\partial z} = i\omega\varepsilon\vec{E}_x \tag{2.24a}$$

$$\frac{\partial \vec{H}_z}{\partial x} - \frac{\partial \vec{H}_x}{\partial z} = i\omega\varepsilon\vec{E}_y \tag{2.24b}$$

$$\frac{\partial \vec{H}_y}{\partial x} - \frac{\partial \vec{H}_x}{\partial y} = i\omega\varepsilon\vec{E}_z \tag{2.24c}$$

Polarization fractions may be used to quantify the hybridization of the mode in either the plane of the mode, or in the direction of propagation. Shown in Equations (2.25) and (2.26), respectively. Continuing to assume x as the propagation axis, then, in former case it describes the purity of the $\vec{E}_y$ component. While in the latter case it describes the purity of the $\vec{E}_x$ component, which is useful for describing the presence of the TE mode.

$$polarization(\vec{E}_y) = \frac{\iint |\vec{E}_y|^2 dydz}{\iint |\vec{E}_y|^2 + |\vec{E}_z|^2 dydz} \tag{2.25}$$

$$polarization(\vec{E}_x) = 1 - \frac{\iint |\vec{E}_x|^2 dydz}{\iint |\vec{E}|^2 dydz} \tag{2.26}$$

2.3.3 Mode Expansion

The electric and magnetic fields may be expressed in terms of their transverse field components and a propagation constant, as shown in Equation (2.27). We assume a structure where the refractive index

distribution does not vary along the propagation axis. The fields represent phasor quantities in the frequency domain with implicit $e^{-i\omega t}$ time dependence. In this formulation $\vec{e}_j$, and β_j are the eigenfunction and eigenvalue corresponding to the guided mode propagating along the x-axis. The transverse field profiles $\vec{e}_j(y,z)$ describe the spatial variation in the transverse plane, while the phase variation along the propagation axis is described by plane wave factor $e^{\beta_j x}$.

$$\vec{E} = \vec{e}_j(y,z)e^{i\beta_j x} \tag{2.27a}$$

$$\vec{H} = \vec{h}_j(y,z)e^{i\beta_j x} \tag{2.27b}$$

In a waveguide, the mode expansion conjecture states that the transverse components of any field may be written as a linear combination of the transverse components of all the waveguide modes at a given frequency. Thus, any possible solution of Maxwell's equations may be expressed as a linear combination of the modes in a constant plane along the propagation axis. The form of mode expansion in Equation (2.28), assumes an invariant structure along the propagation axis. The coefficient, a, denotes the modal amplitude.

$$\vec{E} = \sum_j a_j \vec{e}_j(y,z)e^{-i\beta_j x} \tag{2.28a}$$

$$\vec{H} = \sum_j a_j \vec{h}_j(y,z)e^{-i\beta_j x} \tag{2.28b}$$

2.3.4 Mode Orthogonality

The orthogonality condition relates pairs of guided mode with the transverse components of the modes. It is useful when expressing pairs of modes since it allows the treatment of the total energy associated with each mode as independent and not coupled with the other modes. The derivation here follows the derivation provided by Westerveld and Urbach[79]. The derivation starts with the identity of Equation (2.19). Suppose that identity is expressed for a mode pair, with indices 1 and 2 denoting the modes as in Equation (2.29a). Expanding the results using the laws of Faraday and Ampere, Equation (2.16c) and Equation (2.16d) gives

Equation (2.29b).

$$\nabla \cdot (\vec{E}_1 \times \vec{H}_2^*) = \vec{H}_2^* \cdot (\nabla \times \vec{E}_1) - \vec{E}_1 \cdot (\nabla \times \vec{H}_2^*) \tag{2.29a}$$

$$\vec{H}_2^* \cdot (\nabla \times \vec{E}_1) - \vec{E}_1 (\nabla \times \vec{H}_2^*) = i\omega(\mu \vec{H}_2^* \vec{H}_1 - \varepsilon \vec{E}_2^* \vec{E}_1) \tag{2.29b}$$

Adding the complex conjugate reveals that the right hand side simplifies. This step removes the imaginary components that arise from the cross products of the fields, resulting in an expression that reflects the real energy exchange between the modes. In this case it can be intuited that the time average power exchange between modes do not couple in a way that leads to energy transfer between the modes.

$$\nabla \cdot (\vec{E}_2 \times \vec{H}_1^*) = -i\omega(\mu \vec{H}_2^* \cdot \vec{H}_1 - \varepsilon \vec{E}_2^* \cdot \vec{E}_1) \tag{2.30a}$$

$$\nabla \cdot (\vec{E}_1 \times \vec{H}_2^* + \vec{E}_2^* \times \vec{H}_2) = i\omega(\mu \vec{H}_2^* \cdot \vec{H}_1 - \varepsilon \vec{E}_2^* \cdot \vec{E}_1) - i\omega(\mu \vec{H}_2 \cdot \vec{H}_1^* - \varepsilon \vec{E}_2 \cdot \vec{E}_1^*) \tag{2.30b}$$

$$\nabla \cdot (\vec{E}_1 \times \vec{H}_2^* + \vec{E}_2^* \times \vec{H}_1) = 0 \tag{2.30c}$$

Gauss' theorem, Equation (2.20), can be used to express a form of the mode orthogonality condition. The surface integral of $\vec{E}_1 \times \vec{H}_2^* + \vec{E}_2^* \times \vec{H}_2$ can be related to the volume integral of Equation (2.30c). Shown in Equation (2.31a). Knowing that the divergence of the term is equal to zero, the mode orthogonality condition is expressed as in Equation (2.31b). Meaning there is no energy exchange between the modes.

$$\int_S (\vec{E}_1 \times \vec{H}_2^* + \vec{E}_2^* \times \vec{H}_1) \cdot d\vec{S} = \int_V \nabla \cdot (\vec{E}_1 \times \vec{H}_2^* + \vec{E}_2^* \times \vec{H}_1)\, dV \tag{2.31a}$$

$$\int_S \left(\vec{E}_1 \times \vec{H}_2^* - \vec{E}_2^* \times \vec{H}_1 \right) \cdot d\vec{S} = 0 \tag{2.31b}$$

If the pair of modes is taken to be identical, then it relates the time average power carried in the mode. Assuming the electric and magnetic fields are in phase, which is true for guided modes. The expression for the power carried in the mode is known as the Poynting vector; Equation (2.32).

$$\vec{S} = \vec{E} \times \vec{H} \tag{2.32}$$

The energy density can be found by taking the real part of the Poynting vector, and assuming the time interval is long compared to the mode.

$$S = \Re[\vec{E}] \times \Re[\vec{H}] \tag{2.33a}$$

$$\Re[\vec{E}] = \frac{1}{2}(\vec{E} + \vec{E}^*) \tag{2.33b}$$

$$S_{avg} = \frac{1}{4}\left(\vec{E} \times \vec{H}^* + \vec{E}^* \times \vec{H}\right) \tag{2.33c}$$

Then with the orthogonality of the modes, $\vec{E} \times \vec{H}^* + \vec{E}^* \times \vec{H} = 2\Re[\vec{E} \times \vec{H}^*]$ the expression reduces to Equation (2.34). Which is the time averaged Poynting vector.

$$\vec{S}_{avg} = \frac{1}{2}\Re[\vec{E} \times \vec{H}^*] \tag{2.34}$$

2.3.5 Mode Confinement

The resultant properties of the composite material on a waveguide will depend on a mode's distribution of the electromagnetic energy. The distribution of energy will occupy some part of the core, and some part of the cladding. Waveguides can be classified as high or low confinement. In a highly confined waveguide, the field amplitude of the mode is mostly contained within the core of the waveguide. While in low confinement waveguide, the majority of the field amplitude of the mode is contained within the cladding material.

High-confinement waveguide cores are advantageous for achieving very small bending radii, enabling high density layouts. However, as the core confinement increases, the propagation loss can also rise due to scattering at the rough waveguide sidewalls. This is particularly significant when a sharp discontinuity in the field amplitude of the mode at the waveguide edges results in a greater scattering at the sidewalls. The mismatch in field amplitude at the boundary between the core and cladding is a direct consequence of the

boundary conditions imposed by Maxwell's equations. By contrast, low-confinement waveguides experience less disruption at the core-cladding interface, as a greater portion of the mode intensity propagates through the cladding material. This results in reduced scattering losses and potentially low propagation losses. However, low confinement comes at the cost of weaker confinement of the mode within the core, increasing the likelihood of mode leakage, especially in bent waveguides. Additionally, low-confinement waveguides offer the benefit of supporting single-mode operation over a broader range of wavelengths, which allows for devices with larger optical bandwidths.

The mode confinement Γ defines the ratio of energy which is confined in the core. Related to the confinement is the effective mode area, A_{eff}, it describes an area which is representative of the mode size. The mode confinement is the fraction of the mode area in the core over the total mode area. Generally, the mode confinement is expressed for the j'th mode, per Equations 2.35. The mode confinement is expressed through the Poynting vector, Equation (2.32), which describes the power flow. In waveguide confinement, the interest is to express the energy density along the propagation axis. Throughout this work, x is used as the propagation axis. Furthermore, in this work the mode confinement refers to the fundamental mode, $j = 1$, and may be calculated as in Equation 2.39 using the Poynting vector; Equation (2.32). Since only the fundamental mode is considered, meaning only a single frequency is considered, the time averaged Poynting vector may be used; Equation (2.34). Only the real component of the complex Poynting vector is considered since it describes the propagating energy.

$$\Gamma = \frac{\iint_{A_{core}} \Re(\vec{e}_j \times \vec{h}_j^*) \cdot \hat{x}\, dA}{\iint_{A_\infty} \Re(\vec{e}_j \times \vec{h}_j^*) \cdot \hat{x}\, dA} \tag{2.35}$$

To derive Equation 2.39, first substitute Maxwells equations, Equations (2.16a) and Equation (2.16d) in to the identity for the divergence of a cross product; Equation (2.19). The surface current is assumed zero. The energy density term, Equation (2.37) can be obtained by integrating both sides of the Equation (2.36a) over a volume. Which can be related through Guass' theorem, Equations (2.20). Which may be related to the flux through the waveguide cross section in the direction of propagation as in Equation (2.36b). Then adding the dispersion term, $\frac{d}{d\omega}$ in Equation (2.36c). Where A represents the transverse cross section. This yields the expression for the real energy density in Equation (2.37). Finally quantities such as the mode confinement Equation 2.39 and effective mode area Equation 2.38 can be expressed in terms of the energy

density.

$$\nabla \cdot (\vec{E} \times \vec{H}^*) = -i\omega \left(\varepsilon |\vec{E}|^2 + \mu |\vec{H}|^2 \right) + \vec{E}^* \cdot \vec{J}_s \tag{2.36a}$$

$$\int_V \nabla \cdot (\vec{E} \times \vec{H}^*)\, dV = \int_S \left(\vec{E} \times \vec{H}^* \right) \cdot d\vec{S} \tag{2.36b}$$

$$\int_V \nabla \cdot (\vec{E} \times \vec{H}^*)\, dV = \frac{d}{d\omega} \left(i\omega \int_A \left(\varepsilon |\vec{E}|^2 + \mu_0 |\vec{H}|^2 \right) dA \right) \tag{2.36c}$$

$$W(y,z) = \frac{1}{2} \Re \left[\frac{\omega \varepsilon(y,z)}{d\omega} \right] |\vec{E}|^2 + \mu_0 |\vec{H}|^2 \tag{2.37}$$

$$A_{eff} = \frac{\iint W(y,z)\, dydz}{max(W)} \tag{2.38}$$

$$\Gamma = \frac{\iint_{A_{core}} W(y,z) dydz}{\iint_{A_\infty} W(y,z) dydz} \tag{2.39}$$

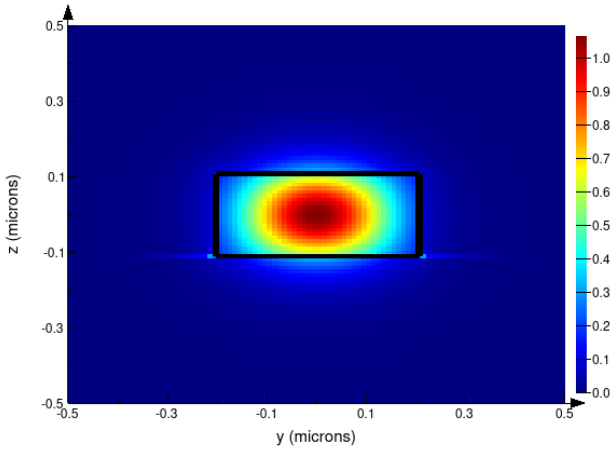

Figure 5: Energy density of mode in cross section of waveguide, arb units. Waveguide dimensions shown as bounding rectangle.

The mode confinement definition, is field confinement For example, Figures 5 show the energy density in a 500x220 nm strip waveguide, where in the core section the mode confinement is approximately 78 %.

2.3.6 Mode Overlap

Mode overlap quantifies the degree of similarity between the spatial distributions of the electromagnetic fields of two modes. It determines the efficiency of power transfer between these modes, both in forward and backward propagation. This is quantified by calculating the overlap integral, which considers both the electric and magnetic field profiles, on a plane defined by the propagation axis. The normalized fraction is related to the amount of power that can propagate between the modes for both forward and backward propagating fields.

$$\text{Mode overlap} = \Re \left| \frac{(\int_S \vec{E}_1 \times \vec{H}_2^* \cdot d\vec{S})(\int_S \vec{E}_2 \times \vec{H}_1^* \cdot d\vec{S})}{(\int_S \vec{E}_1 \times \vec{H}_1^* \cdot d\vec{S})(\int_S \vec{E}_2 \times \vec{H}_2^* \cdot d\vec{S})} \right| \tag{2.40}$$

Mode overlap, Equation (2.40), or the degree to which the optical modes of two waveguides or sections of a waveguide match, is critically related to bending loss. When a waveguide bends, the guided mode shifts and changes shape. If the mode in the bent section does not efficiently overlap with the mode in the straight section of the waveguide, light can be scattered, radiated, or reflected.

2.3.7 Mode Loss

The losses in single mode SOI waveguides at optical c-band was reviewed by Vlasov and McNab [80]. Vlasov and McNab cites Tien [81] and show a model for propagation loss based on the concepts in Tien's work. For straight waveguides, the loss mechanisms are scattering and absorption loss. While in sharply bent waveguides radiation loss can occur [80], [82]. Sakai, Go, and Baba

Vlasov and McNab's relations are shown in Equations 2.41a and 2.41b. Where α is the propagation loss, z_r is the interface roughness between material layers, z_{wg} is the waveguide thickness, k_0 is the free space wave vector, and $\frac{E_s^2}{\int E^2 dx}$ is the normalized field intensity at the core and cladding interface. Vlasov and McNab's model provides insights about the scattering loss.

Equation 2.41a shows the scattering component of the propagation loss will be proportional to the square of the interface roughness. This means strongly confined cores, or modes where the field intensity is

maximum at the sidewalls, may experience greater loss in due to interaction with sidewall roughness. As is the case for TE cores [80]. While scattering losses will be inversely proportional to the waveguide thickness. For example, a thin core may have a more strongly confined mode. However, generally speaking it depends on the mode distribution throughout the interface. Equation 2.41b indicates that the waveguide thickness is treated as related to how strongly confined the mode is at the core cladding interface. The mode confinement will not only be influenced by the geometry of the waveguide but the index contrast of the waveguide. The Vlasov and McNab model states that propagation loss is proportional to Δn^2 where Δn is the difference between the refractive indices of the core and cladding. High index contrast between the core and cladding enables smaller waveguide dimensions but also results in higher propagation losses due to increased interaction of the mode with sidewall surface roughness.

$$\alpha = \frac{4z_r^2 \beta_{core}}{\beta(z_{wg} + 2/\beta_{cladding})} \tag{2.41a}$$

$$\alpha = \frac{z^2 k_0^2 \beta_{core}}{\beta_{eff}} \frac{E_s^2}{\int E^2 dx} \Delta n^2 \tag{2.41b}$$

In a bent waveguide, light can radiate out of the waveguide due to the bend. The bend distorts the waveguide geometry, and the mode can change due to the distortion. The mode can shift towards the edge of the bend leading to increased interaction with the sidewall, radiation, and poor mode overlap. These are three primary contributions for the bend loss, scattering, radiation and mode-mismatch. The radius of the bend is a key geometric parameter affecting light radiation. Sharper bends have more pronounced mode shifts, thus leading to greater radiation losses. Sakai, Go, and Baba studied bending for SOI at optical c-band and concluded the importance of the index contrast in determining the [82]. Bending losses are lower in waveguides with high mode confinement, such as SOI waveguides as the index contrast in SOI waveguides allows for much smaller bending radii compared to silica waveguides [80], [82].

2.3.8 Bloch Modes

Bloch modes describe the propagation for a plane wave in a periodic media. Bloch theory demonstrated that the solution to the wave equation in a periodic medium can be expressed as Equation (2.42). A derivation is

available from Ashcroft [83].

$$\psi_{\beta_x}(x) = e^{-i\beta_x x} \cdot u_{\beta_x}(x) \tag{2.42}$$

$$u_{\beta_x}(x+\Lambda) = u_{\beta_x}(x) \tag{2.43}$$

The wavefunction as written, is not an explicit solution, however, it confines the solution to a set of solutions that can be described by a plane wave modulated by a periodic function for the lattice, meaning the Bloch mode can be calculated for one period of the lattice. For any given wavelength if there are only Bloch modes with $\Re\beta_x \neq 0$ then the wavelength belongs to the band-gap. In a band-gap, no propagative modes exist and any field incident on the structure will be completely reflected as it cannot be coupled with a mode for that structure. This is a useful property for designing mirrors based on periodic media with alternating refractive indices, such as Bragg mirrors [84]. Details of calculating band structures for photonic crystals are given by Bienstman and Baets [76].

One of the practical consequences of Bloch modes is that the band structure for a photonic crystal may be calculated on a unit cell with periodic boundary conditions. Referred to as Bloch boundary conditions. This is a fundamental aspect of Bloch's theorem, as it is based on an infinite media, in which periodic boundary conditions are essential. What are often called Bloch boundary conditions in the study of photonic crystals are related to Born-Von Karman boundary conditions used by Bloch. The approach of a periodic boundary condition permits the study of a whole lattice by considering its unit cell only.

2.4 Effective Medium Theory

Effective Medium Theory (EMT) is modelling technique that is used to study materials, particularly composite materials [85]. The premise is that a composite material property can be calculated by functions defining averages that are representative of the system. EMT provides a way to understand and predict the effective properties of composite materials by averaging known properties of the component materials. For some electromagnetic materials, the effective medium may be expressed by volumetric or electromagnetic field averaging. In the electromagnetic sense, medium is the macroscopic permeability and permittivity

tensors. Examples of anisotropic, crystalline, and uniaxial mediums are shown in Equations 2.44 to 2.46 respectively [78].

$$(Anisotropic)\ \varepsilon = \begin{bmatrix} \varepsilon_{11} & \varepsilon_{12} & \varepsilon_{13} \\ \varepsilon_{21} & \varepsilon_{22} & \varepsilon_{23} \\ \varepsilon_{31} & \varepsilon_{32} & \varepsilon_{33} \end{bmatrix} \mu = \begin{bmatrix} \mu_{11} & \mu_{12} & \mu_{13} \\ \mu_{21} & \mu_{22} & \mu_{23} \\ \mu_{31} & \mu_{32} & \mu_{33} \end{bmatrix} \tag{2.44}$$

$$(Crystal)\ \varepsilon = \begin{bmatrix} \varepsilon_{11} & \varepsilon_{12} & \varepsilon_{13} \\ \varepsilon_{21} & \varepsilon_{22} & \varepsilon_{23} \\ \varepsilon_{31} & \varepsilon_{32} & \varepsilon_{33} \end{bmatrix} \mu = \begin{bmatrix} \mu_0 & 0 & 0 \\ 0 & \mu_0 & 0 \\ 0 & 0 & \mu_0 \end{bmatrix} \tag{2.45}$$

$$(Uniaxial)\ \varepsilon = \begin{bmatrix} \varepsilon_{11} & 0 & 0 \\ 0 & \varepsilon_{22} & 0 \\ 0 & 0 & \varepsilon_{33} \end{bmatrix} \mu = \begin{bmatrix} \mu_0 & 0 & 0 \\ 0 & \mu_0 & 0 \\ 0 & 0 & \mu_0 \end{bmatrix} \tag{2.46}$$

Of practical relevance is the work of Rytov [69]. Rytov's work demonstrates that a layered structure can act as a homogeneous, but anisotropic medium. Meaning that the effective medium is a singly degenerate and has the properties of a uniaxial crystal. This is only applicable in the long-wavelength limit. The long-wavelength condition requires that the wavelength of the electromagnetic radiation be much larger than the size of the material's inhomogeneities, such as the period of a grating. Quantitatively, this means that the structure size should be at the subwavelength scale with respect to the propagating electromagnetic wave. When this condition is met, a complex material can be treated as an equivalent effective medium with spatially averaged properties. The long-wavelength condition is expressed in Equation (2.47).

$$\frac{2\pi\Lambda}{\lambda}|n_{eff}| << 1 \tag{2.47}$$

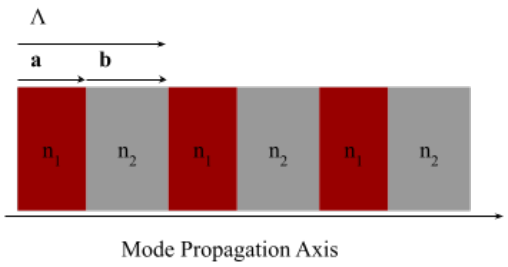

Figure 6: Planar crystal

Consider propagation parallel to the layers, as in Figure 6 for a planar crystal. For this case Rytov gives the expression in Equation 2.48. Where $\varepsilon_1, \varepsilon_2$ are the dielectric constants of the stacked layers and ε_{eff} is the effective dielectric. While a, b, are the lengths of the layers respectively. The more common form for subwavelength optical gratings expresses this formula with the refractive index, and grating period. This is done by substitution. and shown in Equation 2.49c, recalling the relationship between refractive index and permittivity; Equation 2.4.

$$\varepsilon_{eff} = \frac{a\varepsilon_1 + b\varepsilon_2}{a+b} \tag{2.48}$$

$$\varepsilon_r = n^2 \tag{2.49a}$$

$$\frac{a}{a+b} = \frac{a}{\Lambda} \tag{2.49b}$$

$$n_{eff}^2 = \frac{a}{\Lambda} n_1^2 + (1 - \frac{a}{\Lambda}) n_2^2 \tag{2.49c}$$

Rytov's approach is a form of EMT as it directly averages material properties to derive effective parameters, thus simplifying the analysis of complex, layered materials. This means that EMT is a viable approach for defining layered media such as SOI when the feature sizes are at the subwavelength scale. Such as with the modelling of subwavelength gratings. Metamaterials can be invented without augmenting the SOI material stack by using subwavelength gratings. Structuring the core material at the subwavelength scale can be used

to tailor dispersion and other material properties. The special case of a periodic structure at the subwavelength scale defines a uniaxial photonic crystal. Such a device, depending on its period can behave as either a waveguide or an antenna. The subwavelength waveguide case is advantageous since large modal fractions in the cladding can be achieved at low loss compared with strip or rib waveguides [86].

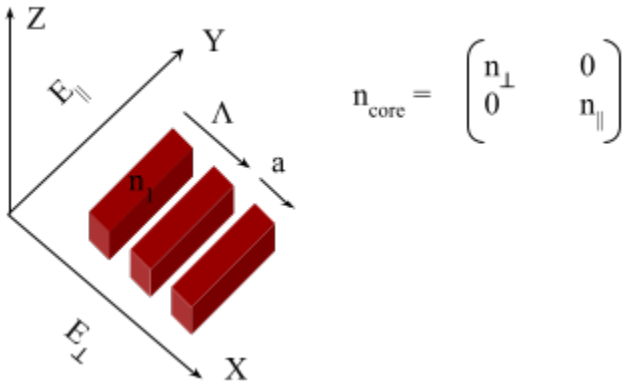

Figure 7: Effective index in core of a uniaxial photonic crystal.

The refractive index tensor shown in Figure 7 can be described by using Rytov's formula. Rytov's formula is expressed for a periodic grating in Equations (2.50) and (2.51).

$$n_{\parallel}^2 = \frac{a}{\Lambda} n_1^2 + (1 - \frac{a}{\Lambda}) n_2^2 \tag{2.50}$$

$$\frac{1}{n_{\perp}^2} = \frac{a}{\Lambda} \frac{1}{n_1^2} + (1 - \frac{a}{\Lambda}) \frac{1}{n_2^2} \tag{2.51}$$

2.5 Coupled Mode Theory

Coupled Mode Theory (CMT) is a mathematical technique which uses solutions to a simpler problem and treats the problem of interest as a perturbation of that soluble problem. The theory expresses the perturbed transverse field in terms of a basis set of modes of the unperturbed waveguide [87]. This technique can be used to model Bragg gratings, and waveguide crosstalk [71].

The derivation of the coupled mode equations here follows the derivation of Jaeger[88]. To derive the

coupled mode equations, first assume the permittivity distribution along the waveguide with perturbations is expressed as in Equation 2.52. The allowed solutions for the unperturbed system are represented as in Equations 2.16. Then the allowed solutions for the perturbed system are represented with E', and H' as in Equation 2.53.

$$\mu = \mu_0 \tag{2.52a}$$

$$\varepsilon' = \varepsilon(y,z) \tag{2.52b}$$

$$\nabla \times \vec{E}' = -i\omega\mu\vec{H}' \tag{2.53a}$$

$$\nabla \times \vec{H}' = i\omega\varepsilon'\vec{E}' \tag{2.53b}$$

To express the relationship between the unperturbed and perturbed systems, the subtraction of the two solutions, Equation 2.54, is used to isolate the perturbation terms, which describe how power is transferred between the modes. The Lorentz reciprocity plays a key role in CMT since it provides the symmetry between the unperturbed and perturbed modes in the system. Using the identity, Equation 2.19 and integrating Equation 2.54 over a volume of V leads to the intermediary Equation 2.55a. Which can be simplified by Guass' Theorem, Equation 2.20 to Equation 2.55b which is known as the Lorentz Reciprocity Theorem. This explains that power exchange is conserved within the volume, neglecting leakage or radiation, and that the modes are coupled through the change in permittivity.

$$\left(\vec{E}^* \cdot \nabla \times \vec{H}' - \vec{H}' \cdot \nabla \times \vec{E}^*\right) - \left(\vec{H}^* \cdot \nabla \times \vec{E}' - \vec{E}' \cdot \nabla \times \vec{H}^*\right) = i\omega(\varepsilon - \varepsilon')\vec{E}^* \cdot \vec{E}' \tag{2.54}$$

$$\int_V \nabla \cdot (\vec{E}^* \times \vec{H}' + \vec{E}' \times \vec{H}^*)\, dV = -i\omega \int_V (\varepsilon' - \varepsilon)\vec{E}^* \cdot \vec{E}'\, dV \tag{2.55a}$$

$$\oint_S (\vec{E}^* \times \vec{H}' + \vec{E}' \times \vec{H}^*) \cdot d\vec{S} = -i\omega \int_V (\varepsilon' - \varepsilon)\vec{E}^* \cdot \vec{E}' dV \tag{2.55b}$$

To solve the relation in Equation 2.55b a waveguide geometry must be assumed. Assume the surface encloses a section of waveguide with faces perpendicular to the propagation axis, with thickness dx and infinite width. This reduces the integral to the form in Equation 2.56. Assuming the perturbation is small,

the perturbed transverse fields of the basis set of modes of the unperturbed waveguide may be expressed as in Equation (2.57), where $\vec{e}_j t$ and $\vec{h}_j t$ are the normalized transverse field distributions of the j'th mode. a_j is the slowly varying mode amplitudes in each mode. Then using Maxwell's equations the full field expansion becomes Equation (2.60) as shown in Equation (2.59). Critically, the perturbation is assumed to be small $\varepsilon/\varepsilon' \approx 1$. Then the full field expansion may be substituted into Equation 2.56, giving Equation (2.61).

$$\int_S \frac{\partial}{\partial x}(\vec{E}_t^* \times \vec{H}_t' + \vec{E}_t' \times \vec{H}_t^*) \cdot \hat{x}\, dS = \int_S (-i\omega(\varepsilon' - \varepsilon)\vec{E}^* \cdot \vec{E}')\, dS \tag{2.56}$$

$$\vec{E}_t'(x,y,z) = \sum_j a_j(x)\vec{e}_{jt}(y,z)e^{-i\beta_{jt}x} \tag{2.57a}$$

$$\vec{H}_t'(x,y,z) = \sum_j a_j(x)\vec{h}_{jt}(y,z)e^{-i\beta_{jt}x} \tag{2.57b}$$

$$\nabla_t \times \vec{e}_{jt} = -i\omega\mu_0\vec{h}_{jx} \tag{2.58a}$$

$$\nabla_t \times \vec{h}_{jt} = i\omega\varepsilon\vec{e}_{jx} \tag{2.58b}$$

$$\vec{E_x}' = \frac{1}{i\omega\varepsilon'}(\nabla_t \times \vec{H_t}') \tag{2.59a}$$

$$\vec{H_x}' = -\frac{1}{i\omega\mu_0}(\nabla_t \times \vec{E_t}') \tag{2.59b}$$

$$\vec{E_x}' = \sum_j a_j(x)\frac{\nabla_t \times \vec{h_{jt}}}{i\omega\varepsilon'}e^{-i\beta_{jt}x} \tag{2.59c}$$

$$\vec{H_x}' = \sum_j a_j(x)\frac{\nabla_t \times \vec{e_{jt}}}{-i\omega\mu_0}e^{-i\beta_{jt}x} \tag{2.59d}$$

$$\vec{E}_x'(x,y,z) = \sum_j a_j(x)\frac{\varepsilon}{\varepsilon'}\vec{e}_{jx}(y,z)e^{-i\beta_j x} \tag{2.59e}$$

$$\vec{H}_x'(x,y,z) = \sum_j a_j(x)\vec{h}_{jx}(y,z)e^{-i\beta_j x} \tag{2.59f}$$

$$\vec{E}'(x,y,z) = \sum_j a_j(x)\vec{e}_j(y,z)e^{-i\beta_j x} \tag{2.60a}$$

$$\vec{H}'(x,y,z) = \sum_j a_j(x)\vec{h}_j(y,z)e^{-i\beta_j x} \tag{2.60b}$$

$$\int_s \frac{\partial}{\partial x}\left[\vec{E_t}^* \times \sum_j a_j(x)e^{-i\beta_j x}\vec{h}_{jt} + \sum_j a_j(x)e^{-i\beta_j x}\vec{e}_{jt} \times \vec{H_t}^*\right] \cdot \hat{x} dS = -i\omega \int_s \left[(\varepsilon' - \varepsilon)\sum_j a_j(x)e^{-i\beta_j x}\vec{e}_{jt} \times \vec{E}^*\right] dS \tag{2.61}$$

Recalling the time average Poynting vector, Equation (2.34), the solutions to Equation (2.61) can be taken for each mode of the unperturbed system, by applying Equations 2.27. Where the eigenfunctions are normalized with respect to the complex Poynting vector as in Equations (2.62). Finally, if each mode in the unperturbed waveguide satisfies the orthogonality condition, then it can be used to simplify the analysis. The orthogonality condition is now expressed such that the normalized eigenfunction relates to the Dirac delta function as given in Equation (2.63). Where δ_{jk} is the Dirac delta function. Applying the normalized eigenfunction and the orthogonality condition, the coupled equations can be written as in Equation (2.64).

$$2\vec{S}_{avg}(k) = \Re \int_S \left[\vec{e^*}_k \times \vec{h}_k\right] \cdot \hat{x}\, dS = \int_S \left[\vec{e^*}_{kt} \times \vec{h}_{kt}\right] \cdot \hat{x}\, dS \tag{2.62a}$$

$$2\vec{S}_{avg}(k) = \Re \int_S \left[\vec{e}_k \times \vec{h^*}_k\right] \cdot \hat{x}\, dS = \int_S \left[\vec{e}_{kt} \times \vec{h^*}_{kt}\right] \cdot \hat{x}\, dS \tag{2.62b}$$

$$\int_S \vec{e_j^*} \cdot \vec{e_n}\, dS = \delta_{jn} \tag{2.63}$$

$$\sum_j \frac{\partial a_j(x)e^{i(\beta_k - \beta_j)x}}{\partial x} \int_S \left[\vec{e^*}_{kt} \times \vec{h}_{jt} + \vec{e}_{jt} \times \vec{h^*}_{kt}\right] \cdot \hat{x}\, dS\, \delta_{jk} = -i\omega \sum_j a_j(x)e^{i(\beta_k - \beta_j)x} \int_S \left[(\varepsilon' - \varepsilon)\vec{e}_j \cdot \vec{e^*}_k\right] dS \tag{2.64}$$

After taking the derivative on the left hand side of Equation (2.64) and applying the Dirac delta. Then the mode expansion can be written as coupled equations, Equation (2.65). Where the coupling coefficient is C_{jk}.

$$\frac{\partial a_k}{\partial x} = -i\sum_j a_j(x)e^{i(\beta_j-\beta_k)x}C_{jk} \tag{2.65}$$

$$C_{jk} = \frac{\omega S_{avg}(k)}{4}\int_S \left[(\varepsilon' - \varepsilon)\vec{e}_j \cdot \vec{e^*}_k\right]\, dS. \tag{2.66}$$

If there are only two modes, and the coupling is periodic, this can lead to strong interaction between forward and backward travelling modes such as with Bragg gratings. With Bragg gratings, it is assumed that there are simultaneous forward and backward travelling modes. The gratings introduce small perturbations that couple the forward and backward going modes. The perturbed transverse field can be expressed in terms of the modes of the unperturbed waveguide. While CMT is a useful approximation, it is not always accurate, particularly for structures with high index contrasts or strong coupling as deriving the coupled mode equations often assumes a small perturbation. In these cases methods such as Transfer Matrix Method (TMM), Eigenmode Expansion (EME) or Finite Difference Time Domain (FDTD) may be required to first estimate the coupling coefficient before applying coupled mode equations [71].

The consideration of two fundamental modes is used in designing waveguide devices such as directional couplers or describing waveguide crosstalk. However, the simplifications in the derivation above may not be suitable for fully describing the coupling in parallel waveguides and more complete models have been derived [89]. As an alternative to perturbation methods for describing waveguide crosstalk of parallel waveguides, the coupling coefficient can be found by supermode analysis. In supermode analysis, the effective indices of the first two eigenmodes of adjacent waveguides may be used to calculate the coupling coefficient for fixed distances between the waveguides. The theory is that crosstalk occurs when the evanescent mode of one waveguide overlaps the evanescent mode of the second waveguide which results in the excitation of a super mode. That is, fundamental modes which propagate in the cladding can overlap and excite a higher order mode. The higher order mode will have a different propagation constant and as the modes travel the field intensity oscillates between the waveguides. The excitation of the higher order mode results in equal suppression of the first mode, leading to transfer of the fundamental mode from the first waveguide to the second waveguide as the modes travel. For two adjacent waveguides with co-directional coupling, the coupling coefficient may be calculated as in Equation 2.67 [71]. However the contra-directional case is more complicated [87]. The coupling length is the length at which this complete

transfer happens. With the two modes co-directional and in phase, the power is localized in the fundamental mode of the first waveguide, after a π phase shift between the modes, the power is fully transferred to the second waveguide. The coupling length may be calculated as in Equation 2.68, and is often referred to as the beat length or crossover length.

$$C = \frac{\beta_1 - \beta_2}{2} \tag{2.67}$$

$$L_\pi = \frac{\pi}{\beta_1 - \beta_2} \tag{2.68}$$

For waveguide crosstalk, it is practical to determine the fraction of power that is transferred from one waveguide to another, based on the coupling coefficient, length of the coupler and the spacing between the waveguides. The transferred power can also be considered as the crosstalk of the waveguides. The fraction of power coupled from one waveguide to the other can be expressed as in Equation 2.69. Where P_0 is the input optical power, P_{cross} is the power coupled across the waveguide. L is the length of the coupler, and C is the coupling coefficient.

$$\frac{P_{crosstalk}}{P_0} = sin\left(\frac{\pi L}{2L_\pi}\right)^2 \tag{2.69}$$

2.6 Transfer Matrix Method

TMM is a technique used to analyze wave propagation in layered and periodic media. It is particularly useful for structures where the refractive index varies along one dimension, such as uniaxial crystals, or waveguide Bragg gratings. TMM calculates the transmission and reflection of light through a structure by representing each layer and interface as a matrix, which may then multiplied together to obtain an overall transfer matrix for the entire structure.

The fundamental relationship of TMM is the transfer matrix, that describes the relationship between the forward and backward propagating waves at the input and output. Equation 2.70 shows the transfer matrix T_{12} for interface between two media shown in Figure 8. Where n_1 and n_1 are the refractive indices of the material, L_1 and L_2 are the lengths of the materials. Assuming normal incidence, the transmission and reflection coefficients can be estimated with the plane wave approximation as the Fresnel coefficients, Equation 2.71. If each material is a uniform section of waveguide with length L, the propagation matrix, P

may be expressed as in Equation 2.72. While for the index step change between two waveguides, T_{12}, the transfer matrix is expressed as in Equation 2.73.

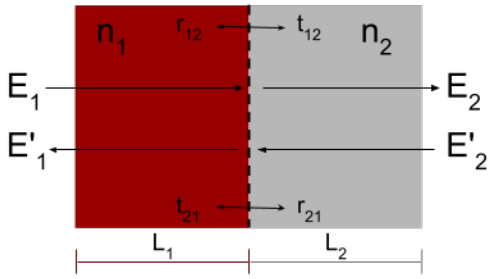

Figure 8: Transmission and reflection at an interface of two dielectric materials.

$$\begin{bmatrix} E_1 \\ E_1' \end{bmatrix} = T_{12} \begin{bmatrix} E_2 \\ E_2' \end{bmatrix} \tag{2.70}$$

$$r_{12} = \frac{n_1 - n_2}{n_1 + n_2} \tag{2.71a}$$

$$r_{21} = \frac{n_2 - n_1}{n_1 + n_2} \tag{2.71b}$$

$$t_{12} = \frac{2n_1}{n_1 + n_2} \tag{2.71c}$$

$$t_{21} = \frac{2n_2}{n_1 + n_2} \tag{2.71d}$$

$$P = \begin{bmatrix} e^{i\beta L} & 0 \\ 0 & e^{-i\beta L} \end{bmatrix} \tag{2.72}$$

$$T_{12} = \frac{1}{t_{12}} \begin{bmatrix} 1 & r_{12} \\ r_{12} & 1 \end{bmatrix} = \begin{bmatrix} \frac{n_1+n_2}{2\sqrt{n_1 n_2}} & \frac{n_1-n_2}{2\sqrt{n_1 n_2}} \\ \frac{n_1-n_2}{2\sqrt{n_1 n_2}} & \frac{n_1+n_2}{2\sqrt{n_1 n_2}} \end{bmatrix} \tag{2.73}$$

To analyze a structure composed of multiple layers and interfaces, the transfer matrices of each layer may be cascaded. Here, assume a third media and second interface is introduced. The expressions for the additional

media and interface can be introduced as before and expressed in transfer matrix form as in Equation 2.74.

$$\begin{bmatrix} E_1 \\ E_1^{'} \end{bmatrix} = T_{12}P_2T_{23} \begin{bmatrix} E_3 \\ E_3^{'} \end{bmatrix} \tag{2.74a}$$

$$P_2 = \begin{bmatrix} e^{i\beta_2 L_2} & 0 \\ 0 & e^{-i\beta_2 L_2} \end{bmatrix} \tag{2.74b}$$

$$T_{23} = \begin{bmatrix} \frac{n_2+n_3}{2\sqrt{n_2n_3}} & \frac{n_2-n_3}{2\sqrt{n_2n_3}} \\ \frac{n_2-n_3}{2\sqrt{n_2n_3}} & \frac{n_2+n_3}{2\sqrt{n_2n_3}} \end{bmatrix} \tag{2.74c}$$

The scattering matrix, S, for the network can be generalized for any number of interfaces as in Equation 2.75. In the case of a periodic structure of two media, such as a Bragg grating with N periods, we can express the generalized form with powers as in Equation 2.76. Where the indices 1, and 2, represent the high and low index regions of the grating respectively. The transmission and reflection coefficients for the Bragg grating may then be expressed as in Equation 2.77.

$$\begin{bmatrix} E_1 \\ E_1^{'} \end{bmatrix} = S \begin{bmatrix} E_N \\ E_N^{'} \end{bmatrix} \tag{2.75a}$$

$$\begin{aligned} S &= P_1T_{12}P_2T_{23}...P_NT_N \\ &= \begin{bmatrix} S_{11} & S_{12} \\ S_{21} & S_{22} \end{bmatrix} \end{aligned} \tag{2.75b}$$

$$S_{bragg} = (P_1T_{12}P_2T_{21})^N \tag{2.76}$$

$$t_{bragg} = \frac{1}{S_{11}} \tag{2.77a}$$

$$r_{bragg} = \frac{S_{21}}{S_{11}} \tag{2.77b}$$

2.7 Finite Difference Eigenmode

The Finite Difference Eigenmode (FDE) formulation solves the eigenvalue matrix equations for electric and magnetic fields. The finite difference equations are approximations for the wave equations. The approximations are formed by taking the difference in field amplitudes over a discrete grid of points to construct the first and second order field derivatives at each grid point. The mode solver then must find a distribution of field amplitudes that satisfy the Helmholtz wave equation. The solution is expressed for a single wavelength, thus numerous simulations are required for studying dispersion. However, mode solutions are useful in the study of waveguide propagation, waveguide bending, reflection coefficients in Bragg gratings (with support of TMM), and even phase modulation [71].

For finite difference methods, there are two important considerations, the size of the mesh, and the extent of the mesh in the solver region. The grid size should be small enough that the refractive index is constant in each cell and the field amplitude at the edge of the grid is negligible. Schemes for construction of the mesh when the geometry is irregular may vary [90]. The field condition may be enforced by Perfectly Matched Layer (PML) boundary conditions [91] or the solver extent can be placed where evanescent modes become negligible.

2.8 Eigenmode Expansion

The EME method is a technique used to analyze the propagation of light by decomposing the field into the modes in discrete positions along the propagation axis. Each discrete slice is a cell, and each cell of the structure may have its mode calculated by FDE. However, the mode solution in the cell calculated by FDE is invariant along the propagation axis. To represents structures which vary along the propagation axis, recall that fields in a cell may represented with their modes, as in Equations (2.27). Furthermore, such modes may be represented with modal decomposition, as in Equation (2.28). However, in this case it is more convenient to represent the expansion with coefficients, a, and b, for the forward and backward propagating modal amplitudes. As in Equation (2.78). The mode expansion may contains coefficients for

both the forward and backward travelling wave, indicating the bidirectional nature of the solution.

$$\vec{E} = \sum_j (a_j + b_j)\vec{e}_j(y,z)e^{-i\beta_j x} \tag{2.78a}$$

$$\vec{H} = \sum_j (a_j + b_j)\vec{h}_j(y,z)e^{-i\beta_j x} \tag{2.78b}$$

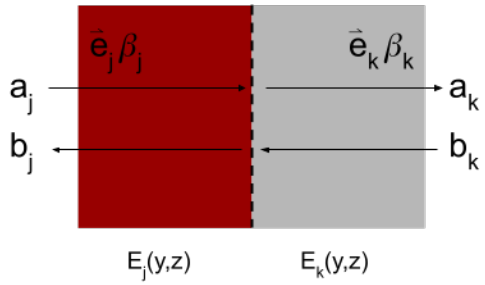

Figure 9: Scattering at material interface with incident modal amplitude a_j, transmitted modal amplitude a_k and reflected modal amplitude b_k.

The differing propagation constants in the modes of each cell set the behaviour along the propagation axis, and the modal amplitudes may be used to describe coupling between cells. The amplitudes of the forward, backward, and transmitted propagating waves are related to the mode overlap between cells. Derivation of this relationship can be found in the sources [76], [79].

$$\begin{bmatrix} a_j \\ b_j \end{bmatrix} = S_{jk} \begin{bmatrix} a_k \\ b_k \end{bmatrix} \tag{2.79}$$

Scattering matrices are generated for each interface in the waveguide structure, and the overall propagation of light through the structure may be determined by progressive multiplication of these scattering matrices. Since an interface need only be defined where there is a change in the index of a slice, individual slices may be very large without affecting accuracy.

2.9 Finite Difference Time Domain

Similar to FDE, in FDTD Maxwell's equations are solved by finite difference equations. However, unlike FDE the electromagnetic field amplitudes at each grid point is solved with a discrete time dimension. As with FDE the mesh size must be small enough to accurately approximate the differential equations. However, with FDTD the time dimension must also be discretized so that errors cannot propagate easily within the mesh. At each time point in FDTD the electric and magnetic field amplitudes are determined by the field amplitude at the current time step and then propagated forward. Having a time dimension makes FDTD suitable for studying photonic crystals, such as subwavelength gratings, which exhibit wavelength dependent properties. A frequency transform of the time-dependent electromagnetic fields of such devices can be used to express the band structure.

2.10 Interconnect

Interconnect is a photonic integrated circuit analysis platform [92]. Interconnect elements are known as compact models. The compact models may be thought of as a scattering matrix, as with EME. Where the matrix describes relationship between input and output ports and modes of the device. Thus the propagation properties of the device in a bidirectional sense. To determine the coupling between multiple devices, For example, coupling coefficients between waveguides. Interconnect can perform overlap integration between two waveguides devices before scattering analysis. Scattering analysis can then be performed by cascading, scattering matrices such as for TMM or EME. However this requires that all the component scattering matrices are known. For devices such as modulators whose scattering matrix depends on external parameter, interconnect may also perform preliminary simulations to determine a scattering matrix based on electrical signal input.

3 Athermal Optical Phased Array

3.1 Constraints

Multi Project Wafer (MPW) runs are a means of distributing costs of a wafer across many project. An advantage with using foundry fabrication for prototyping is access to mature parts through the foundries Process Design Kit (PDK). Allowing monolithic integration for custom devices with other devices whose performance post fabrication is well documented. For designing custom devices, the designer must account that the fabrication process will involve systematic, process drift, and random errors. Loosely this can be thought of as lithography effects, for example variation in the silicon thickness will often be random and due to roughness and material defects while variation in the width of the silicon will also tend be to be systematic as perfectly vertical sidewalls are not often achieved. Specifically, the Advanced Micro Foundry (AMF) process comes with fixed constraints, such as the device thickness, and minimum feature resolution, as well as variations to the specification of the design that occur as part of the lithography process; Table 6. The AMF process constraints design choices. The AMF constraints allow for open oxide regions, and implantation; Table 5. Open oxide regions are necessary for doing athermal design, and implantation is required for using the plasma dispersion effect to get electro-optic phase shifting.

Table 5: Process Constraints - AMF MPW.

Constraint	Design Spec
SOI - Device Layer	220 nm Si
SOI - Buried Oxide	3000 nm SiO2
Minimum Spacing	120 nm
Partial Etching	90 nm, 150 nm
Implants	P++, P+, P, N++, N+, N
Open Oxide	Si feature $\geq 400\ nm$

Table 6: Process Variation - AMF MPW.

Device Layer	Variation
Width	± 25 nm
Thick	± 10 nm
Gaps	± 25 nm
Etch	± 15 nm
Overlay	± 60 nm

All Optical Phased Array (OPA)'s share a common set of features. (1) a splitting tree which is composed of waveguides and power splitters to form channels. The power splitters can be y-branches, Multi-Mode Interferometer (MMI) or directional couplers. (2) A set of phase modulators which control the refractive index in one or more channels of the array. (3) An antenna array which radiates the input signal in each of the channels. Custom waveguides were designed with the constraints of the AMF MPW process. A P-doped, Intrinsic, N-doped semiconductor (PIN) modulator Intellectual Property (IP) was released by Silicon Electronic-Photonic Integrated Circuits (SiEPIC). The MMI's for the splitting tree were selected from the AMF PDK. The grating couplers for the antenna array were also selected from the AMF PDK.

3.2 Waveguides

3.2.1 Athermal Design Process

With the confinement factor and an estimate for the first order thermal dependence of each material, the composite TOC can be calculated for varying waveguide geometries. For strip and rib waveguides, the mode shape is constant along propagation axis, so the material property can be estimated using the mode its cross section as shown in Equation 3.1. While for subwavelength waveguides the process is more complicated.

$$\frac{dn_{eff}}{dT} = \sum_i \Gamma_i \frac{dn_i}{dT} \tag{3.1}$$

Cladding	Material	n	$\frac{dn}{d\lambda}(nm^{-}1)$	$\frac{dn}{dT}(K^{-}1)$	Ref
SiO_2	-	1.44	-1.2E-5	8.5E-6	[67]
SU8	Epoxy	1.57	-3.56E-6	-1.3E-4	[68], [93]
OC-431A	Silicone	1.4378	-5.69E-6	-3.5E-4	[94]

Table 7: Material properties of claddings at λ = 1550nm.

The process for designing an athermal waveguide involves bringing together foundry parameters and free design parameters. Foundry parameters are geometric or material properties which are fixed by the foundry, such as the AMF MPW constraints. While free parameters are material or geometric properties which are open to the designer to choose. The dispersion and TOC of commercial materials are presented in Table 7. The material data for SU8 is available from Polyanski and Mikhail [68] with book definition Microchem SU-8 3000. The material data for OC-431A is available from its data sheet [94]. As shown in Table 5, the AMF MPW has the constraint that silicon structure beneath the open-oxide region is larger than 400 nm. In this case it is advantageous to use materials with a TOC which is both opposite and larger in magnitude than silicon. To weakly confine the mode, that is to have a larger percentage of the mode in the cladding, the core structure size must be decreased. The percentage of the mode required in the cladding will depend on the magnitude TOC of the cladding. The core structure size for athermal waveguides will be larger for materials with a larger and opposite magnitude of TOC. The material OC-431A was selected for its commercial availability, and large magnitude of TOC.

The process for a strip waveguide involves varying the waveguide width to adjust the percentage of the mode in the cladding, for a given cladding material with an opposite thermal dependence with respect to Silicon. Materials with opposite thermal dependence are shown in Table 7.

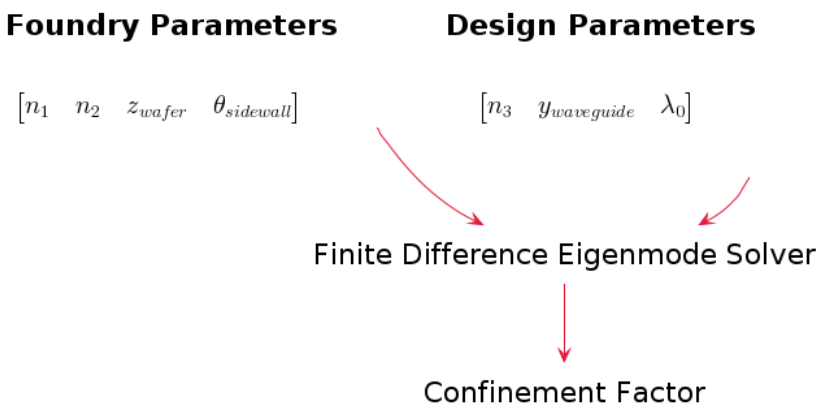

Figure 10: Process for designing athermal strip waveguide.

There is a constraint of fixed parameters from the foundry and free parameters available to the designer, shown in Figure 10. For example, n_1 and n_2 are fixed by the SOI design process; shown in Figure 1. The wafer thickness, z_{wafer} may be limited by the wafer supplier, and process biases, $\theta_{sidewall}$, are fixed by the foundry. The design process then has the freedom to substitute the cladding, n_3, and adjust the waveguide width, $y_{waveguide}$, for the design wavelength λ_0. The design cycle can be repeated to estimate the effects of different cladding materials on the composite materials thermal dependence. Shown in Figure 18 for OC-431A.

The process for a rib waveguide is similar to that of a strip waveguide, but contains an extra free parameter, y_{rib} and y_{slab}, which describes the geometry of the etched and partially etched layers respectively. This is an additional optimization parameter for the designer, due to increased complexity of the geometry.

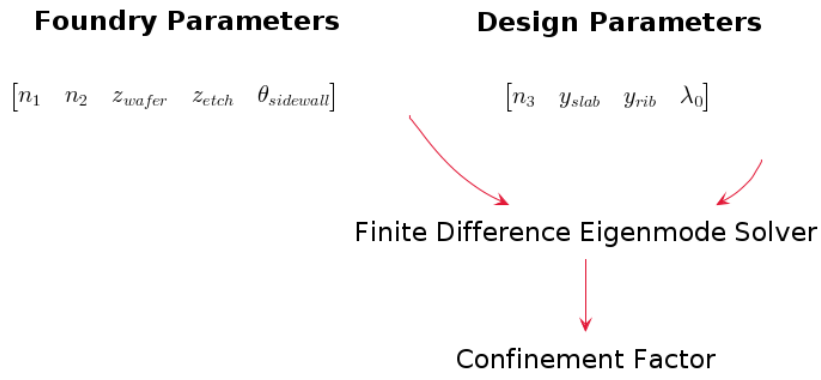

Figure 11: Process for designing athermal rib waveguide.

Estimating the TOC of a subwavelength waveguide is a more tedious process since the Bloch modes cannot be solved directly by FDE. Estimating the Bloch mode requires simultaneously solving the forward and backward propagating modes. It has been shown by the author of this thesis that the TOC of a subwavelength grating may estimated with a similar formulation to Equation 3.1, but with the addition of effective medium theory terms which are specific to the grating [65]. While FDTD may also be used with Bloch boundary conditions to first estimate the band structure.

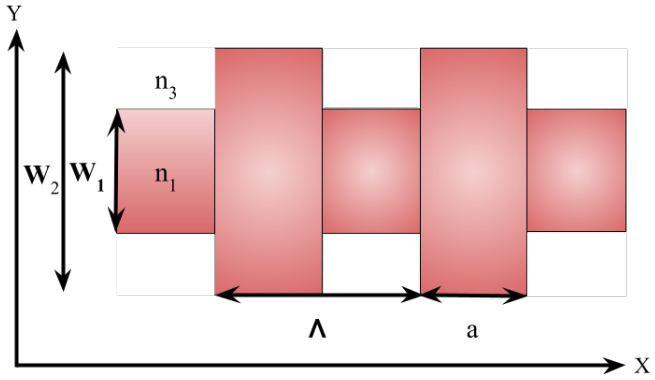

Figure 12: Geometric definition of Bragg grating.

$$\frac{A_{Core}}{A_{Tot}} = \frac{W_2\Lambda}{W_2 a} = DC \tag{3.2}$$

$$\frac{A_{Clad}}{A_{Tot}} = \frac{W_2\Lambda - W_2 a}{W_2 a} = (1 - DC) \tag{3.3}$$

$$\frac{dn_{eff}}{dT} = \left(\Gamma_{W_2}\frac{dn_1}{dT} + (1-\Gamma_{W_2})\frac{dn_3}{dT}\right)DC + \left(\Gamma_{W_1}\frac{dn_1}{dT} + (1-\Gamma_{W_1})\frac{dn_3}{dT}\right)(1-DC) \tag{3.4}$$

In this particular closed form of the series, the contribution of the buried oxide is assumed to be negligible, which is the case for SiO_2 at 1550 nm.

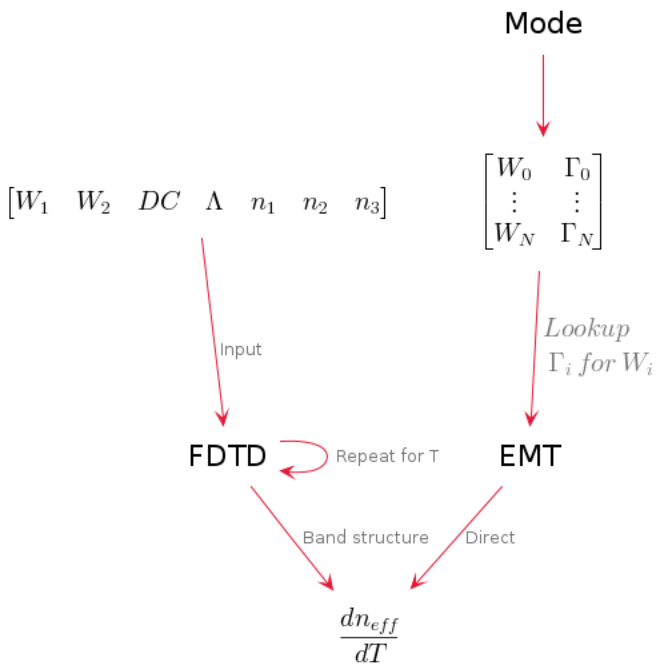

Figure 13: Comparison of methods for predicting the thermo-optic coefficient of a Bragg grating.

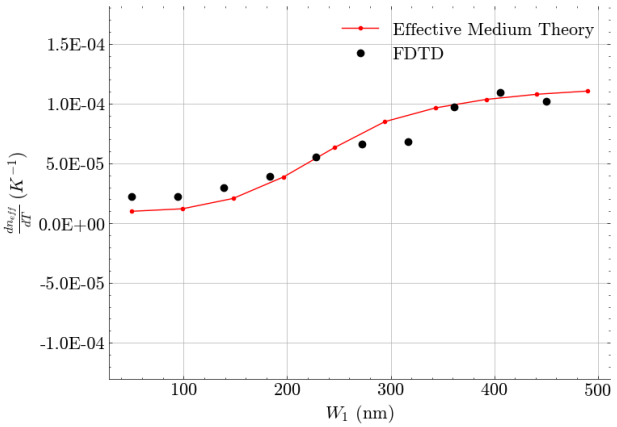

(a) Duty Cycle = 58%

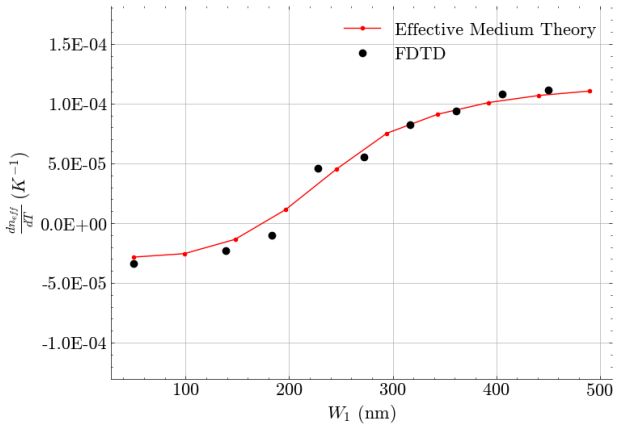

(b) Duty Cycle = 42%

Figure 14: Subwavelength waveguide on 260 nm SOI stack with varying width for cladding SU8. Pitch of 250 nm. Wavelength of 1550 nm.

The process for the discussed techniques of estimating the TOC of a subwavelength waveguide are shown graphically in Figure 13. Each of the methods are used in Figures 14a and 14b. For the EMT approach, the mode solutions of a strip waveguide are first stored in a lookup table then used to solve Equation (3.4). For the FDTD approach, the simulation is solved using Bloch boundary conditions (Section 2.3.8) for each set of geometric and material parameters to study; then repeated for a small perturbation of temperature. In this

study the temperature perturbation was 10 degrees Celsius. EMT directly obtains the TOC unlike FDTD which was used to first obtain the band structures for a set of temperatures. Both the EMT and FDTD methods produce experimental results which are agreeable with each other, although it is expected that FDTD should be more accurate since the EMT method does not consider perturbation of the modes in the lookup table that occur due to coupling between the high and low index region of the grating. To the best of the authors knowledge, the EMT approach for the athermal design of Bragg gratings was not previously available in literature.

3.2.2 Waveguide Design

FDE simulations were used to vary the waveguide width. Study of the waveguide width was used for determining the points at which the waveguide will support single mode TE operation. Single mode waveguides are preferred as they better preserve coherence due to the relation of the mode with a single propagation constant. The simulation was performed using Lumerical FDE and the waveguide models were constructed in the software as SOI waveguides with cladding replaced by the material OC-431A; See Table 7 for the material properties of OC-431A. The convergence of the mesh size and extent were studied for the custom waveguide structures; Figure 15. It was found that with a sufficiently small mesh, less than 10 nm, the refractive index converged to 4 significant figures. While the required mesh extent was 3 μm to be sufficiently far that the evanescent electric field is approximately zero.

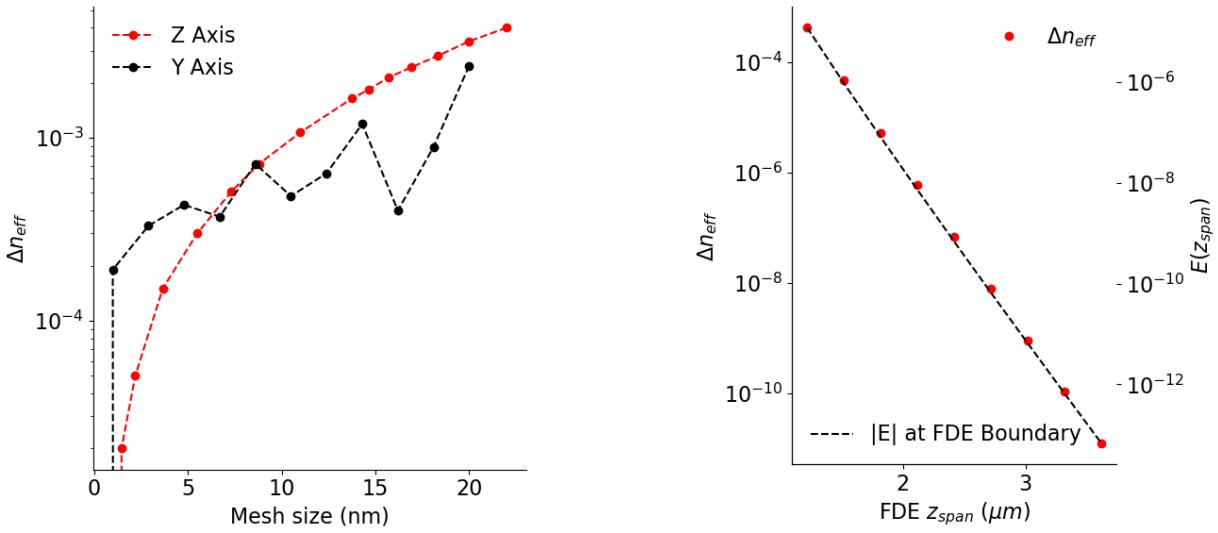

(a) Mesh size.

(b) Mesh Extent.

Figure 15: Analysis of FDE convergence.

Figures 18 and 19 show the effective TOC against width and the thermal dependence of the waveguides in Table 9. The strip waveguide design was specified as for 410 nm width as the device layer has to be greater than 400 nm under an open oxide region. Although not perfectly athermal at 410 nm, the design exhibits an order of magnitude reduction in TOC compared with the natural state of silicon. The same constraint is respected for the rib waveguide where a 410 nm slab, and 250 nm rib is selected and a similar improvement of an order of magnitude is exhibited. Narrow waveguides have the advantage that they are single mode. Figures 16 and 17 show the effective index of the waveguide against width and that the waveguides in Table 9 will be single mode. This is desirable since higher order modes will have different propagation constants within the waveguide. Single mode waveguides will better preserve coherence due to the single optical propagation path.

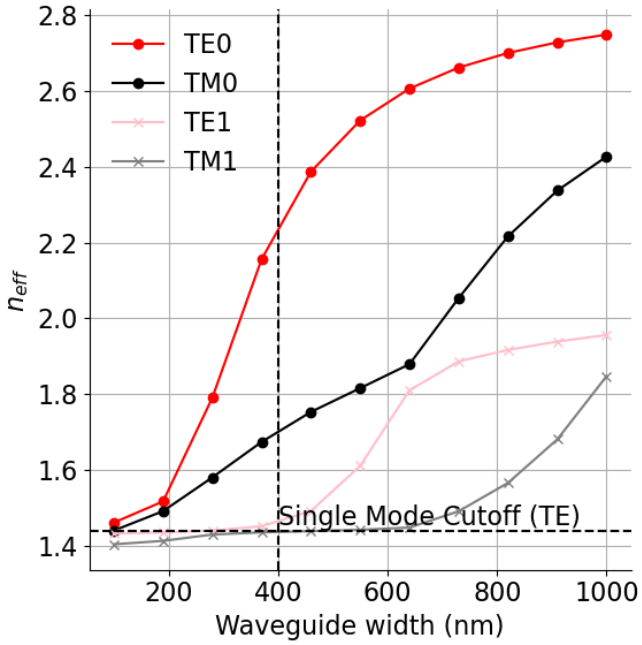

Figure 16: Effective index of strip waveguide on 220 nm SOI stack with varying waveguide thickness for cladding OC-431A. Wavelength of 1550 nm.

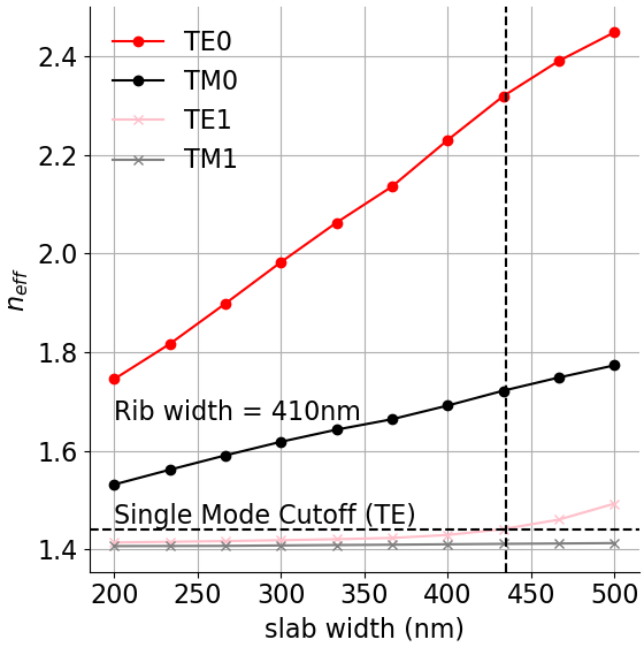

Figure 17: Effective index of rib waveguide on 220 nm SOI stack with varying waveguide thickness for cladding OC-431A. Wavelength of 1550 nm.

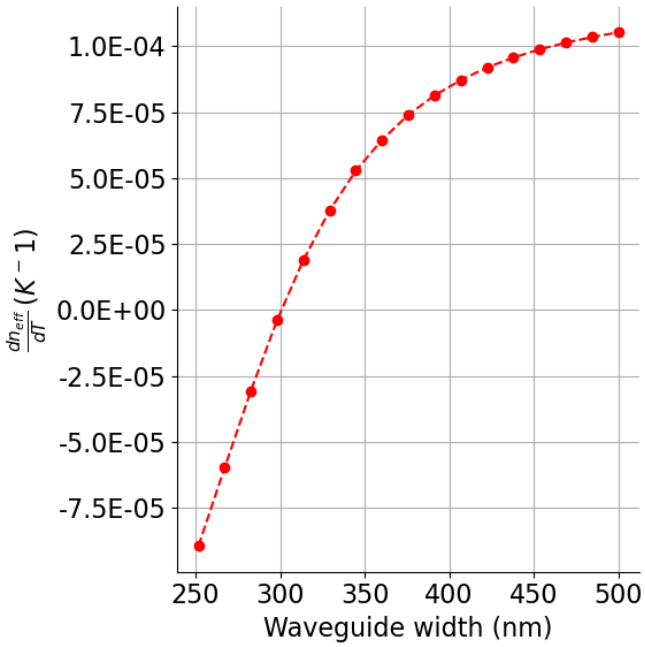

Figure 18: Thermo-optic coefficient of strip waveguide on 220 nm SOI stack with varying waveguide thickness for cladding OC-431A. Wavelength of 1550 nm.

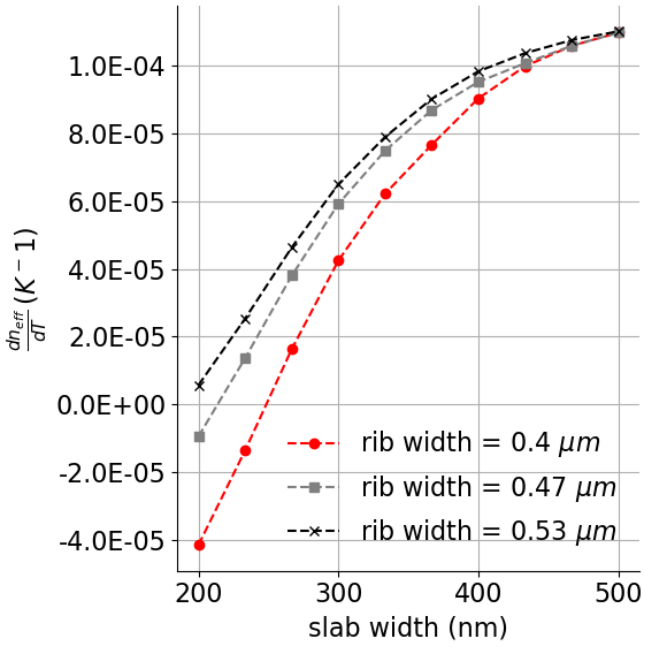

Figure 19: Thermo-optic coefficient of rib waveguide on 220 nm SOI stack with varying waveguide slab and rib thickness for cladding OC-431A. Wavelength of 1550 nm.

The corner cases of the manufacturing variation were simulated for each of the waveguide designs and are

shown in Figures 20a - 21b. The uncertainty in the TOC due to the corner cases of the process variation is at the same order of magnitude as the expected design value. However, at the corner cases for both the strip and rib waveguides, the designs are an improvement over the TOC of silicon.

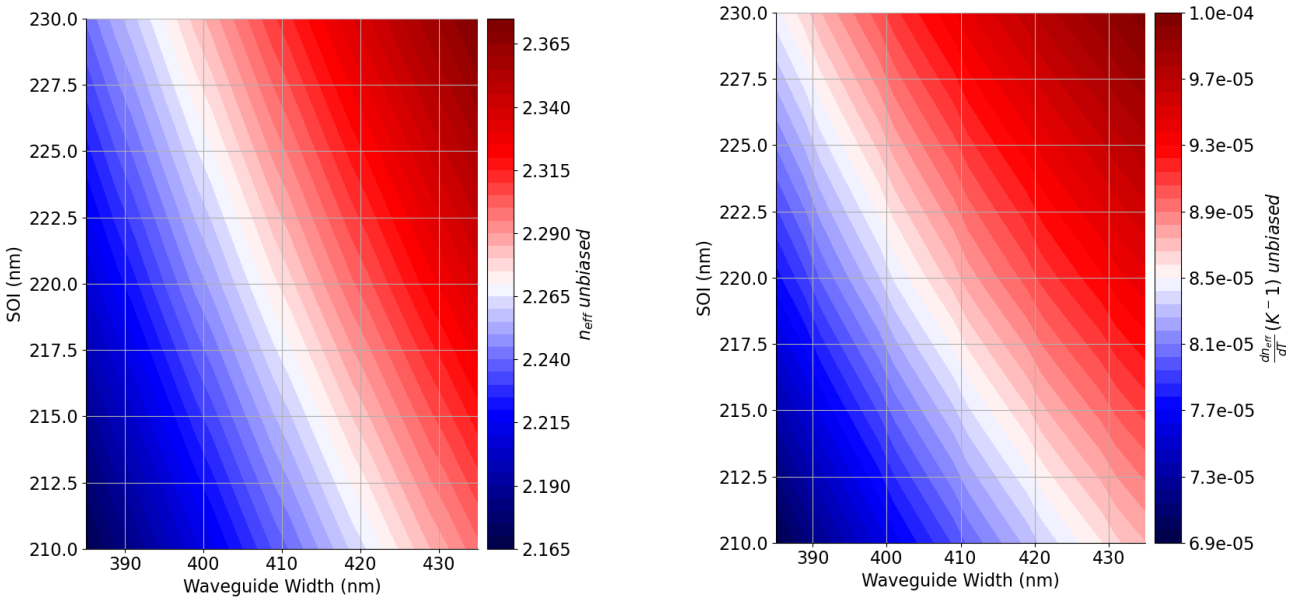

(a) n_{eff} corner cases.

(b) $\frac{dn_{eff}}{dT}$ corner cases.

Figure 20: AMF manufacturing tolerances for strip waveguide.

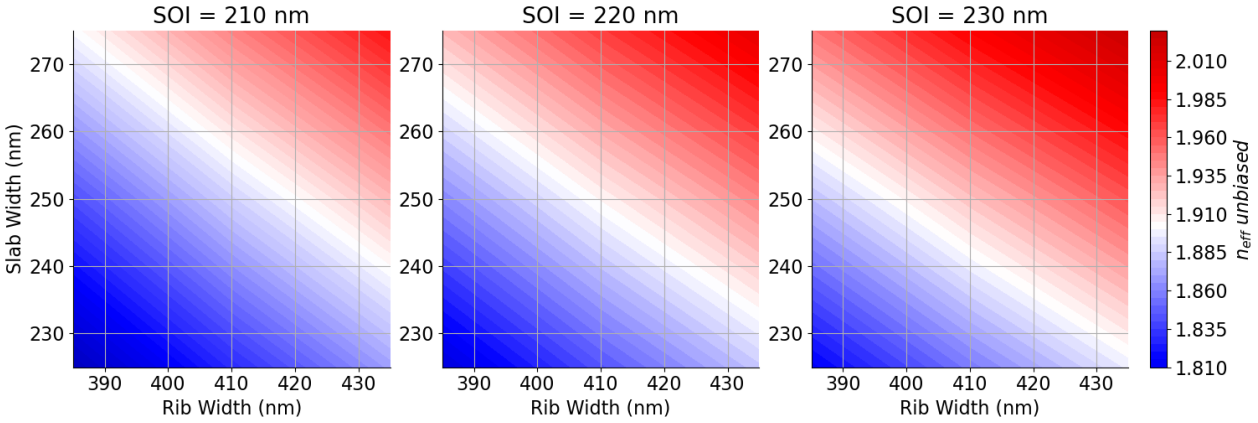

(a) n_{eff} corner cases.

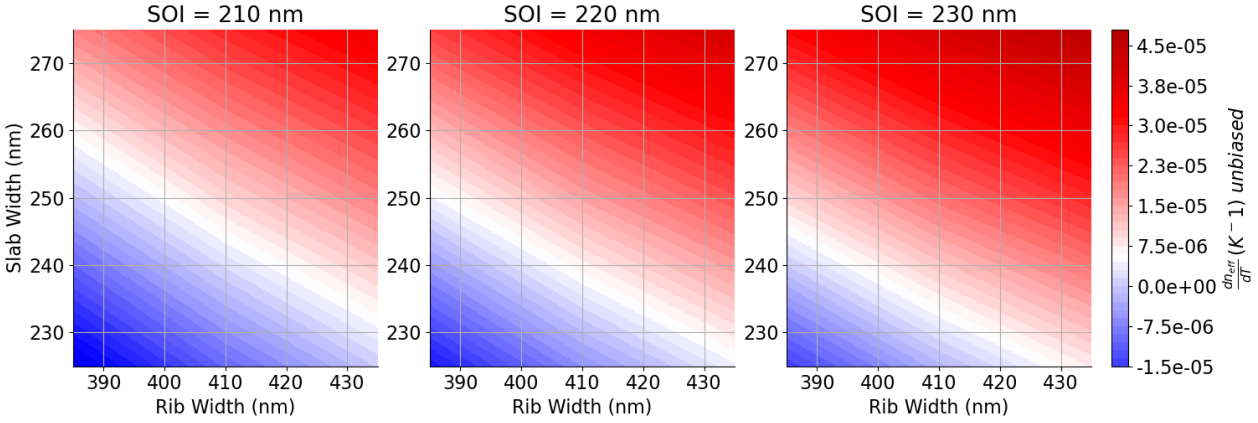

(b) $\frac{dn_{eff}}{dT}$ corner cases.

Figure 21: AMF manufacturing tolerances for rib waveguide.

To go from design to layout, the design of a custom waveguide core requires investigating the distance at which crosstalk is negligible. The confinement of the fundamental waveguide mode sets a lower bound on the minimum separation, with lower-confinement cores experiencing greater crosstalk than higher-confinement cores. A common mitigation strategy is to implement a design rule that separates all waveguides on a chip by a minimum distance to minimize crosstalk. To quantify such a distance, the coupling length between adjacent waveguides was determined by FDE of the custom core for adjacent and identical waveguide structures. With the coupling length relationship Figures 22a and 23a, and the relations derived through CMT, the gap distance between waveguides required to achieve levels crosstalk was estimated; Figures 22b and 23b.

Finally, in addition to waveguide separation, the layout rules governing minimum bend radius must be established before proceeding to optical layout. FDE of the custom core was used to identify the loss of the

waveguide as a function of the bend radius. Shown in Figures 22c and 23c, is the loss contributions as a function of bend radius for strip and rib waveguides respectively. The loss for the waveguide was simulated in FDE by displacing the mode to represent a bent waveguide and calculating the mode overlap, refer to Section 2.3.6. The mode mismatch is the square of the mode overlap. Negligible radiation loss was found in the strip waveguide case, and the mode mismatch term dominates. For the rib waveguide, mode mismatch is greater than the radiation loss, although the radiation loss is still significant for small bend radii. The propagation losses such as scattering and substrate leakage dominate for large bends in both waveguide designs.

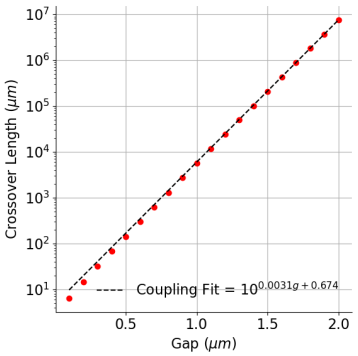

(a) Strip waveguide coupling length.

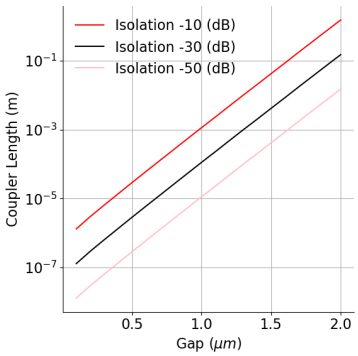

(b) Strip waveguide crosstalk.

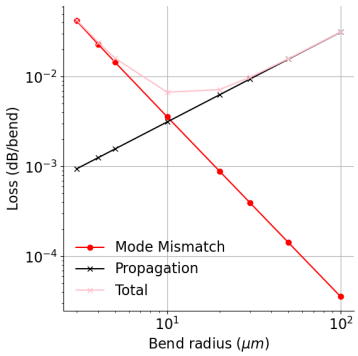

(c) Strip waveguide bending loss.

Figure 22: Analysis of coupled mode and bending losses for 410x220 nm strip waveguide.

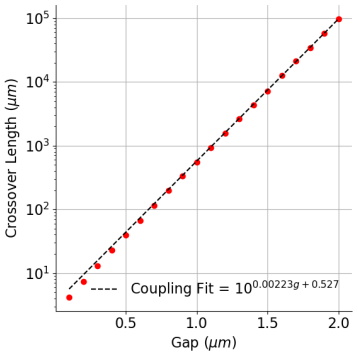

(a) Rib waveguide coupling length.

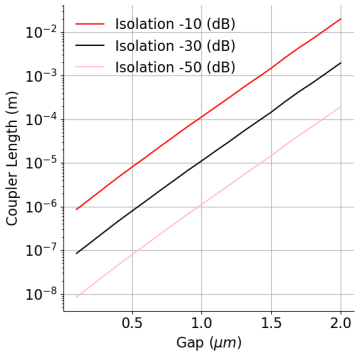

(b) Rib waveguide crosstalk.

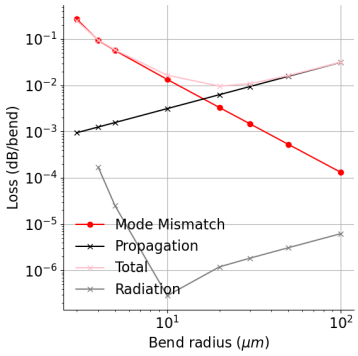

(c) Rib waveguide bending loss.

Figure 23: Analysis of coupled mode and bending losses for 410x250x220 nm rib waveguide.

3.2.3 Mode Tapers

If connecting waveguides of different widths, the mismatch in effective area of the mode will lead to poor coupling efficiency at the interface of the structures. This may be understood through the mode overlap 2.3.6. Alternatively, allowing the mode shape to slowly evolve over a fixed length, by means of slowly expanding or contracting the width of the waveguide, allows the transition between structures to be adiabatic for a sufficiently long length. The simplest function to connect two different waveguide widths is a linear taper. The linear taper can be imposed on both the rib and slab layers if connecting a strip waveguide to a rib waveguide as in Figure 24.

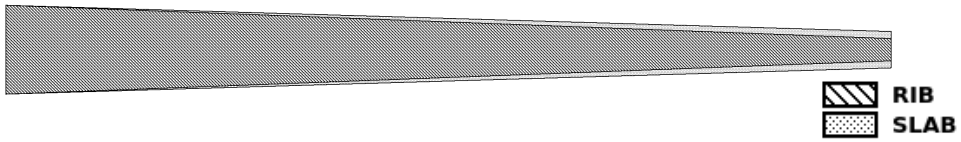

Figure 24: Linear strip waveguide to rib waveguide mode taper.

Commonly, linear tapers are featured where space is not constrained. Otherwise adiabatic horn shaped tapers proposed by Milton and Burns [95] can be made more compact. The adiabatic horn taper, based on the first order mode spreading is compared against linear taper in Figure 25. Fu, Ye, Tang, *et al.* [96] also compare tapers based on different functional shapes. Other forms of compact mode converting include sinusoidal tapers [97], [98], and lens focusing [99].

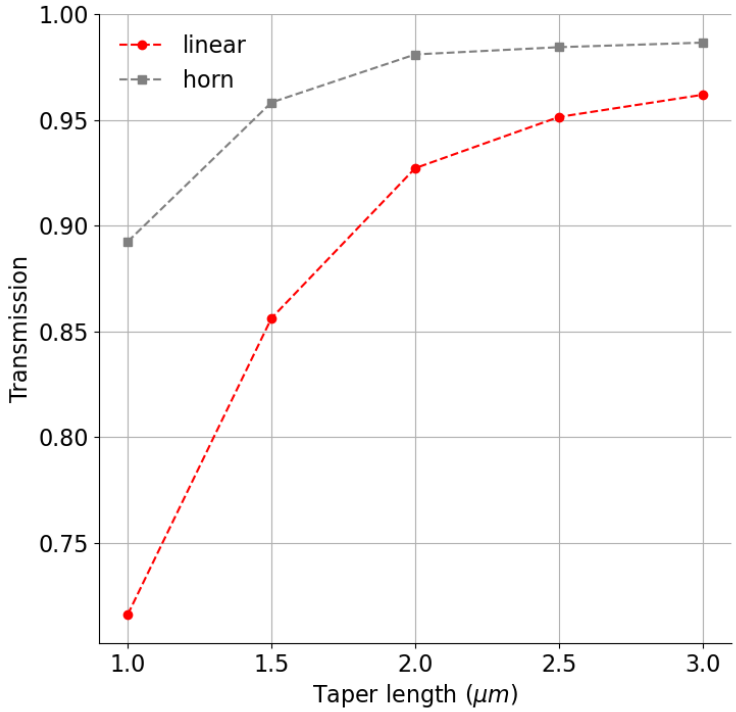

Figure 25: Transmission after coupling loss when tapering from a 0.5 to 2 μm waveguide.

Simulation of mode converters are possible by EME techniques [76], [100]. The standard waveguide size for the AMF and SiEPIC PDK at optical c-band is 500 nm. To connect the custom waveguides devices in the AMF PDK, mode tapers are required. The designed mode tapers in some cases need to have the dual function of adapting a rib waveguide geometry to a strip waveguide geometry; as for design 3 in Table 9. The required input and output dimensions for the mode converters are described in Table 8 .Lumerical EME simulations were used to estimate the transmission characteristics of the mode converts using linear tapers. The EME simulations are used to determine the length required to transition from a 500 nm waveguide to the design waveguide sizes in Table 9. In Figures 27 and 28 the results of these simulations show that 20 μm long tapers are sufficient to have adiabatic transitions between the waveguide geometries for the linear tapers. In the layout shown in Figure 31, the tapers between the waveguides and PDK cells are 20 μm.

Table 8: Mode taper requirements for coupling custom waveguides to AMF PDK.

Input Waveguide	Output Waveguide	Input (nm)	Output (nm)
Strip	Strip	500	410
Strip	Rib	500	250 rib, 410 slab

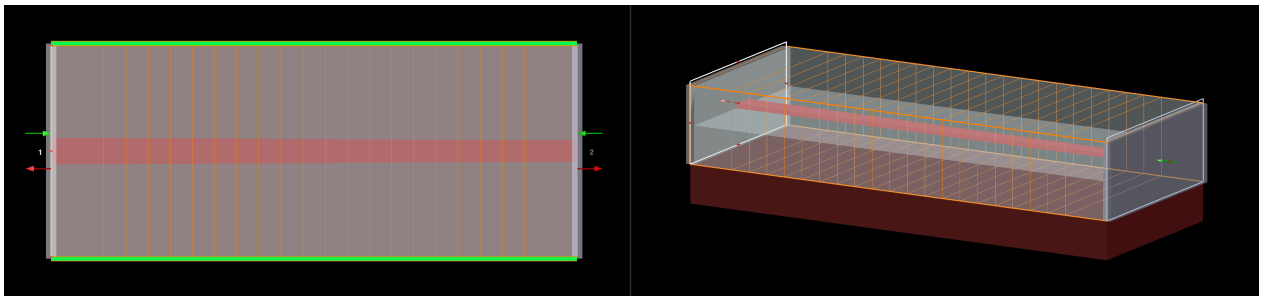

Figure 26: EME simulation of linear taper for a strip waveguide.

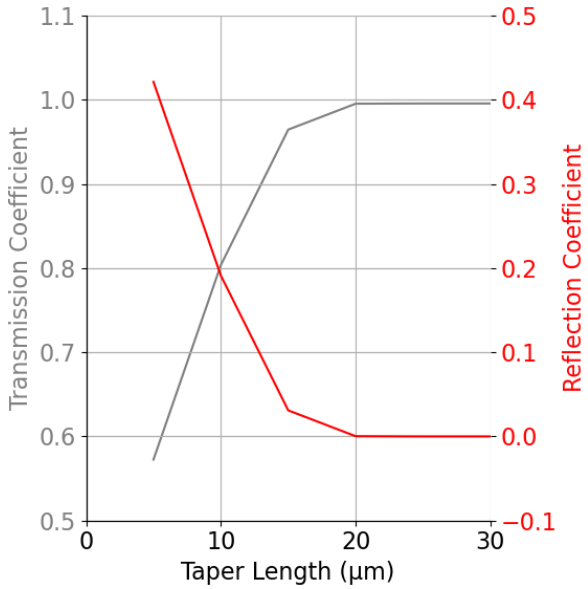

Figure 27: Transmission and reflection as a function of length for linear strip waveguide taper. Input is 500 nm strip waveguide, output is 410 nm strip waveguide.

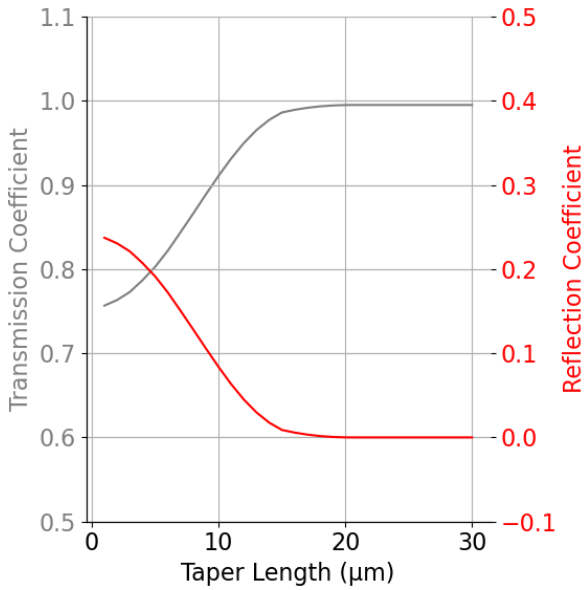

Figure 28: Transmission and reflection as a function of length for linear strip to rib waveguide taper. Input is 500 nm strip waveguide, output is rib waveguide with 410 nm slab and 250 nm rib.

3.3 Feed Network

Phased arrays are often implemented as linear or dense arrays [41], [66], The array factor equation for a linear array is given in Equation 3.5. The array factor has a notable condition $\frac{\pi d}{\lambda}$. Grating lobes appear in the case where the pitch, $d > \frac{\lambda}{2}$. Grating lobes limit the steering range and in routing of an OPA, care must be taken to select the pitch. i.e. care must be given to grating lobe suppression. sparse array variants of the dense array configuration can help with suppression of grating lobes [66]. While Circular and conformal array configuration are possible [101], the subject here was limited to the implementation of a linear array. Examples of linear, dense, and sparse array layouts are shown in Figure 29.

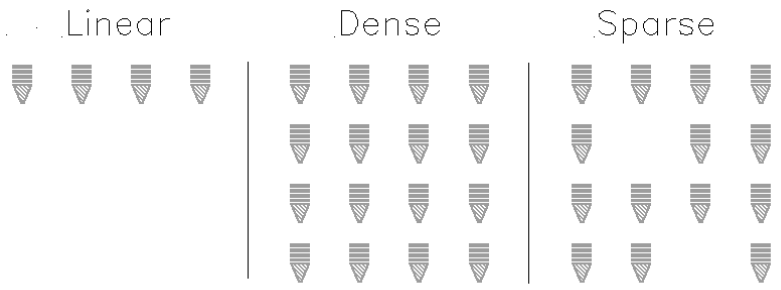

Figure 29: Antenna array configurations.

Linear arrays are often used in photonics [102], [103]. A modern account of implementation of OPA's in literature is given by Guo, Guo, Li, *et al.* [102]. However linear arrays often depend on wavelength control to obtain 2D steering. While wavelength steering possible for Optical Intersatellite Links (OISL), this conflicts if the communication system uses Wavelength Division Multiplexing (WDM) for splitting communication channels. In such cases, dense arrays are preferred as the wavelength dimension cannot be used for steering. However, a linear array of channels may still be used to drive a dense array of antennas. Ashtiani and Aflatouni demonstrated the ability to drive dense array of antennas with only a linear array of phase modulators and without need for wavelength tuning [66]. The array factor for an N element linear array is shown in Equation (3.5).

$$AF(\theta,\Delta\Phi) = \frac{sin(N[\frac{\pi d}{\lambda}sin(\theta) - \frac{\Delta\Phi}{2}])}{Nsin([\frac{\pi d}{\lambda}sin(\theta) - \frac{\Delta\Phi}{2}])} \tag{3.5}$$

3.3.1 Thermal Management

The thermal sensitivity of a length of waveguide, L, may be calculated by the change in phase velocity. The phase velocity, v_p, is related to the propagation constant. Substituting Equations 2.3 and 2.7 into Equation 3.6, Equation 3.7 is obtained. Equation 3.7 is the phase shift for a change in reference temperature. An analytical means to calculate the thermal sensitivity of the waveguides.

$$v_p = \frac{\omega}{\beta} \tag{3.6}$$

$$\Delta\phi = \frac{2\pi L}{\lambda}\frac{dn_{eff}}{dT}\Delta T \tag{3.7}$$

A novel scheme for thermal management of optical phased arrays was addressed in three parts. First by introducing optical phase symmetry, second by reducing the TO effect in the silicon waveguides of the array, and finally by using EO phase modulators.

$$\frac{\Delta\phi_1}{\Delta T} = \frac{\Delta\phi_2}{\Delta T} \tag{3.8}$$

Here optical phase symmetry is defined as equal wrapped phase angle and equal rate of change phase angle due to temperature. The desire for optical phase symmetry comes from the consideration for how temperature of an OPA can change. This condition is important since temperature sensitivity can be defined in two ways. The case where temperature of the wafer changes uniformly and the case where temperature does not change uniformly, for example in the presence of a non-uniform heat distribution on the surface; hot spot. That's adjacent to saying when temperature of all the waveguides changes by the same amount in the uniform case, and when temperature of the waveguides changes by different amounts in the hotspot case. The optical phase symmetry condition eliminates the thermal sensitivity in the uniform temperature change case since relative phase between channels is preserved. Relative phase of the channels is the parameter that determines steering in the the array factor equation. By the array factor, Equation 3.5, it is understood that the relative phase shift between the emitters $\Delta\Phi$ determines the steering angle of the phase θ. Thus, a linear array feed network whose temperature drifts uniformly will not experience a change in steering angle due to temperature sensitivity of the individual waveguides phase angle. In the case of non-uniform temperature change, such as a hotspot, which produced non-uniform distribution of temperature on the chip, it is advantageous to reduce the TO effect. The case where temperature does not change uniformly is handled by the athermal design of the waveguides. With reduced or eliminated TO effect in the waveguides, the use of EO effect for phase modulation becomes necessary as phase modulation through the Joule heating becomes weakened or impossible. Extending the concept of optical phase symmetry to dense arrays is possible by maintaining an integer multiple of the wavelength between columns in the array. This preserves the wrapped phase between antennas when the routing lengths are not the same. However, care must be taken to also adjust the phase change rate.

The first optical phase symmetry condition occurs when routing lengths are the same, this is expanded from Equation (3.8) in Equations (3.9). It is clear that the phase symmetry condition can be satisfied when all routing lengths are the same. In some cases, preserving the routing length may not be possible. The second optical phase symmetry may be expanded as in Equation (3.10) for cases of unequal routing length. The term $\frac{N\lambda}{n}$ is the additional length required for a 2π phase shift so relative phase can be preserved. In this case

differing the TOC may be used to preserve the phase symmetry. Although, there is a degenerate solution if the TOC's are zero. In the degenerate case, phase symmetry is preserved as there is no change of phase due to temperature.

$$\frac{2\pi L_1}{\lambda \Delta T}\frac{dn_1}{dT} = \frac{2\pi L_2}{\lambda \Delta T}\frac{dn_2}{dT} \tag{3.9a}$$

$$L_1\frac{dn_1}{dT} = L_2\frac{dn_2}{dT} \tag{3.9b}$$

$$L_1 \overset{\frac{dn_1}{dT}=\frac{dn_2}{dT}}{=} L_2 \tag{3.9c}$$

$$\frac{2\pi L_1}{\lambda \Delta T}\frac{dn_1}{dT} = \frac{2\pi L_2}{\lambda \Delta T}\frac{dn_2}{dT} \tag{3.10a}$$

$$\frac{2\pi L_1}{\lambda \Delta T}\frac{dn_1}{dT} = \frac{2\pi(\frac{L_1 n_1}{n_2} + \frac{N\lambda}{n_2})}{\lambda \Delta T}\frac{dn_2}{dT} \tag{3.10b}$$

$$L_1\frac{dn_1}{dT} = \left(\frac{L_1 n_1}{n_2} + \frac{N\lambda}{n2}\right)\frac{dn_2}{dT} \tag{3.10c}$$

$$L_1\dot{n_1} \overset{\frac{dn}{dT}=\dot{n}}{=} L_1 n_1\frac{\dot{n_2}}{n_2} + N\lambda\frac{\dot{n_2}}{n_2} \tag{3.10d}$$

Consider the hypothetical phased array layout in Figure 30. Then, with models for the refractive index and TOC as a function of the waveguide width, the conditions that lead to optical phase symmetry for the array may be calculated using Equation (3.10). Assume the layout is routed using the custom strip waveguides described in Figure 20a and 20b. In such a case we have both n and $\frac{dn}{dT}$ as a function of the waveguide width. Thus it is possible to express the symmetry conditions as function which can be solved by inversion for the width of the waveguide. With respect to a given a reference waveguide $L_1,\ n_1,\ \frac{dn_1}{dT}$ and length multiple N. The derived result is shown in Equation (3.11a). The solution of problem may be vectorized, and is shown in tensor form in Equation (3.11b).

$$w \overset{f=\frac{\dot{n_2}(w)}{n_2(w)}}{=} f^{-1}\left(\frac{L_1\dot{n}_1}{L_1 n_1 + N\lambda}\right) \tag{3.11a}$$

$$w_{jk} = f^{-1}\left(\frac{L_1 \dot{n}_1}{L_1 n_1 + N_{jk}\lambda}\right) \tag{3.11b}$$

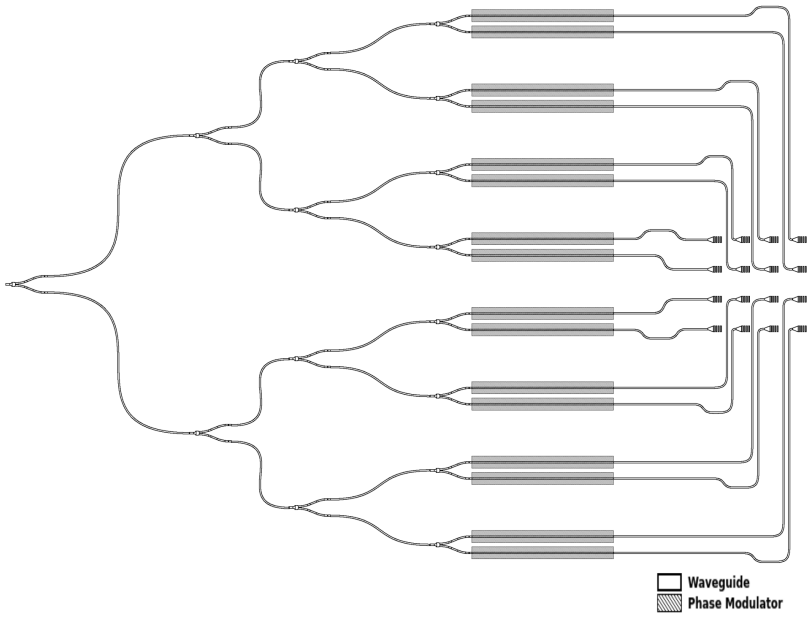

Figure 30: 4x4 OPA layout.

To calculate the width required for optical phase symmetry to each of the antennas. The tensor N_{jk} represent the length multiples of the routing requirement in the layout of the OPA in Figure 30. The reference length L_1 is 35 μm. The solution then depends on the assumed starting width. Here the calculation is seeded with an initial width of 0.5μm. The waveguide widths required to achieve phase symmetry were solved with (3.11b). The resulting width tensor, w_{jk} for optical phase symmetry is shown below.

$$N_{jk} = \begin{bmatrix} 0 & 1 & 2 & 3 \\ 0 & 1 & 2 & 3 \\ 0 & 1 & 2 & 3 \\ 0 & 1 & 2 & 3 \end{bmatrix}$$

$$w_{jk} = \begin{bmatrix} 0.5 & 0.47 & 0.45 & 0.43 \\ 0.5 & 0.47 & 0.45 & 0.43 \\ 0.5 & 0.47 & 0.45 & 0.43 \\ 0.5 & 0.47 & 0.45 & 0.43 \end{bmatrix} \mu m$$

3.3.2 Layout and Limitations

The layout submitted to the AMF MPW features three design variations of a 4 element linear array. A reference SOI design, and less temperature sensitive designs using the strip and rib waveguides discussed in Section 3.2.

Design	waveguide	dimensions (nm)	cladding
1	strip	500x220	SiO_2
2	strip	410x220	OC-431A
3	rib	410x250x220	OC-431A

Table 9: OPA design variations

All the design variations shown in Figure 31 are optically phase symmetric; Section 3.3.1. Each design can be coupled to using a 1x8 fibre array with 127 μm pitch on the right hand side of the chip. Each design variations uses the the first and last grating coupler in the layout for loop-back alignment of the fibre array. The first and second are for an embedded Mach-Zehnder Interferometer (MZI). The remaining fibres are for the input and output of the OPA. There are arrays of bond pads to drive the phase modulators which can be coupled to with a 1x8 electrical probe array with 150 μm pitch. This gives simultaneous control of all the phase modulators on one design variation. The waveguides in the second and third design variations feature open-oxide regions where the cladding can be substituted with OC-431A. The first embedded MZI is for

characterizing the V*pi* of the phase modulator. The second and third embedded MZI have open-oxide regions and are for characterizing the TOC of the custom waveguides.

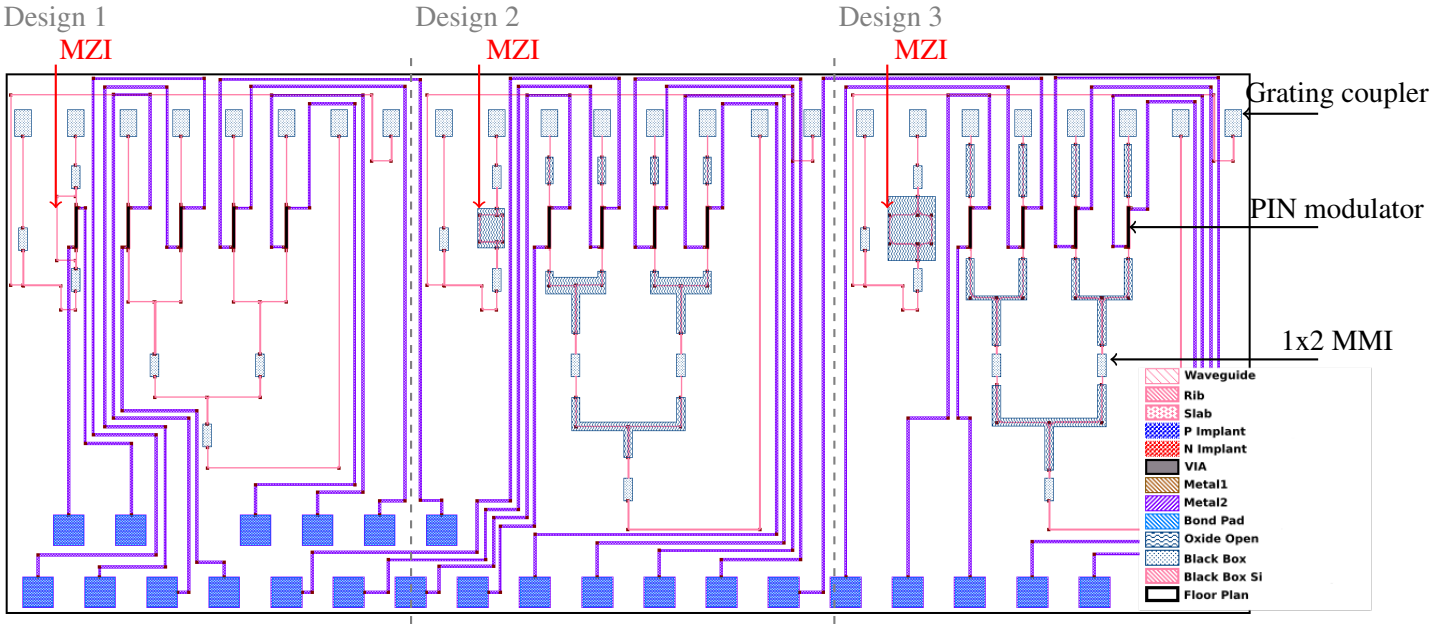

Figure 31: Layout of OPA with three design variations.

Finally the routed OPA has limitations. As the pitch of the gratings were selected to be compatible with a standard fibre array, the layout is considered as an OPA feed network. Furthermore, no attempt was made in this iteration of producing athermal phase modulators or athermal power splitters. As those components in the OPA are either from the SiEPIC or AMF PDK respectively.

3.3.3 Thermal Sensitivity

Assuming the routing length between the phase modulators and the emitters, the thermal sensitivity of the waveguides in each design variation is calculated using Equation (3.7), shown in Table 10. The uniform temperature sensitivity is negated since the linear arrays satisfy the phase symmetry conditions.

Design	$\frac{dn_{eff}}{dT}(K^{-}1)$	uniform $\Delta\phi(degK^{-}1)$	hotspot $\Delta\phi(degK^{-}1)$
1	1.8e-4	-	7.2
2	9.5e-5	-	3.6
3	1.2E-5	-	0.5

Table 10: Thermal sensitivity of the optical phased array design variations.

The change in temperature gradient supporting the thermal management an OPA in literature, Section 1.2. was an order of magnitude. This is equivalent with reducing the thermal dependence by the same scale. Which is shown to be possible by athermal design with the AMF MPW constraints. Furthermore the inclusion of optical phase symmetry eliminates uniform temperature change sensitivity.

4 Athermal Antenna

4.1 Constraints

In SOI design, the capability of emitting light out of the chip orthogonal to the propagation axis is limited by planar design constraints. Silicon devices are produced by etching. The ability to design structures that vary along the etched dimension is constrained by the partial etch capability available from the foundry. The etched dimension is invariant in a single etch only process. However, diffracting light out of the optical waveguide is possible by means of a grating.

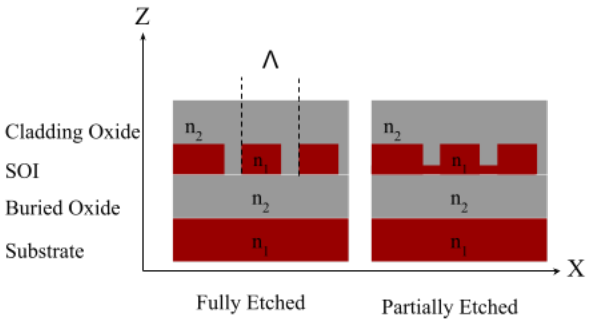

Figure 32: Fully and partially etched grating on SOI.

Design of grating couplers was extensively analyzed by Tamir and Peng [104]. However, review on the modern approaches to design of grating couplers is given by Cheng, Mao, Li, *et al.* [105]. Modern grating design often features partial etching, or material hybridization. However, the design constraints selected for this study were uniform etching, minimum features of 70 nm, and a silicon layer thickness of 220 nm. These constraints are representative of fabrication available from Advanced Nano Tools (ANT).

4.2 Grating Couplers

Gratings despite their advantage in being able to couple light out of a chip with a planar structure, can exhibit significant temperature dependence, back reflections, substrate penetration, and mode mismatch with fibres.

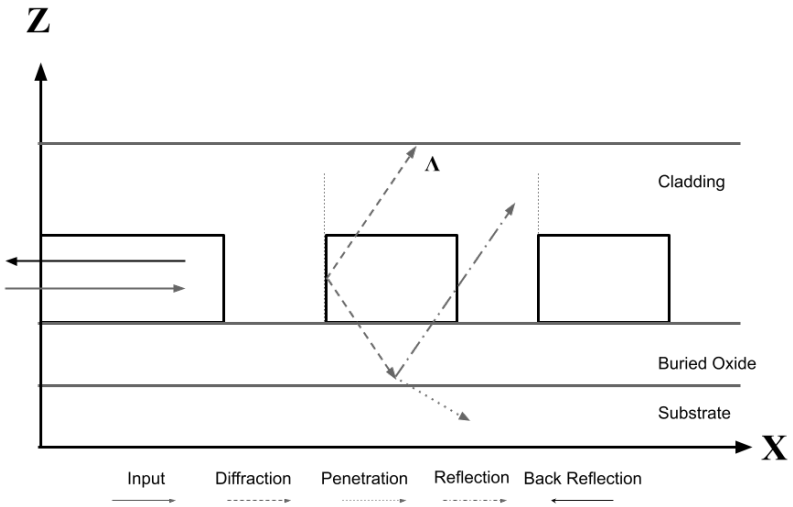

Figure 33: Diffraction, reflection, and penetration effects in grating coupler.

The phase match or Bragg condition, Equation 4.3, of the grating may be used to design for the emission angle of the grating. The general form of the Bragg condition is Equation (4.1), where $\frac{2\pi}{\Lambda}$ is the periodicity of the grating, $\beta = \frac{2\pi}{n_{eff}\lambda_0}$ and β_x is the wave vector of the diffracted wave in the direction of propagation, M is the diffraction order. The diffraction angle can be related through Snell's law as in Equation (4.2). Then with substitution of Equation (4.1) into Equation (4.2) form of Equation (4.3) is derived.

$$\beta - \beta_x = M \cdot \frac{2\pi}{\Lambda} \tag{4.1}$$

$$sin(\theta) = \frac{\beta_x}{\beta} \tag{4.2}$$

$$\frac{n_{eff}(\lambda)}{\lambda} = \frac{n_{clad} sin(\theta)}{\lambda} + \frac{M}{\Lambda} \tag{4.3}$$

When the wavelength inside the grating, $\frac{\lambda_0}{n_{eff}}$ matches its period, then the first order, M=1, diffraction is vertical. While the second order diffraction is a back reflection, which can be as high as 30% in a full etch process [71]. Often gratings are designed to output at an off-vertical angle. In this case the wavelength is smaller than the grating period and there is no significant back reflection. Note that a grating will also diffract light into the substrate due to symmetry and in a full etch process the penetration in to the substrate can be a loss of more than 50% [71].

Furthermore, Doerr, Chen, Chen, *et al.* [106] relate the bandwidth of the grating and the refractive index through the phase matching condition and showed that the bandwidth of the grating may be increased by decreasing the effective index of the waveguide. Chen, Xu, Cheng, *et al.* [107] extended this relationship to show the contribution of the dispersion to the bandwidth, Equation 4.4. From which it can be understood that increasing the pitch and dispersion will lead to larger bandwidths for the grating coupler [107]. The grating can be divided in to apodized and uniform sections to support suppression of back reflections [107] within the operating bandwidth.

$$\lambda_{1dB} \propto \left| \frac{-n_{clad} cos(\theta)}{\frac{n_{eff}(\lambda) - n_{clad} sin(\theta)}{\lambda_0} - \frac{dn_{eff}}{d\lambda}} \right| \tag{4.4}$$

For single polarization grating design, Mekis, Gloeckner, Masini, *et al.* suggest three primary design considerations, emission angle, grating apodization, and lateral layout [108]. The emission angle has been treated above. Although the grating apodization is typically for dealing with mode mismatch, it can also be used to improve radiation efficiency [109], as it is a means to control the distribution of the scattered light. Finally, lateral expansion involves expanding the mode from the waveguide to the lateral size of the diffraction grating. Broadband grating couplers which follow the conditions from Mekis, Gloeckner, Masini, *et al.* are common. Wang, Shi, Wang, *et al.* [48], additionally fill the low index region of the grating with a subwavelength grating structure to achieve finer control refractive index in the low index region.

Of particular interest for phased arrays is the miniaturization of grating couplers, as the pitch of the gratings is directly related with the steering capability of the phased array [66]. However, grating couplers, even those proposed for optical phased arrays can be orders of magnitude larger than the operating wavelength [110], without consideration for the size of the taper. Miniaturization of the antenna comes with the advantage of increased field of view (FOV), however, with increase in the FOV of the antenna comes a decrease in the effective aperture [44]. Fundamentally, the challenge in designing a small planar grating is the loss of efficiency.

Modern grating design is complex on SOI even before allowing augmentation of the material stack, and may not necessarily be based on the Bragg condition; demonstrated by Cheben, Xu, Janz, *et al.* [111]. For example, Melati, Dezfouli, Grinberg, *et al.* [112] approach the design of small gratings by means of

dimensionality reduction, starting from a grating definitions with a large number of parameters. Melati, Dezfouli, Grinberg, *et al.* use parameterized cells that include partial etch and secondary subwavelength structures in a cell, where the cell can also be apodized along the periodic dimension. Khajavi, Melati, Cheben, *et al.* [113] follow a similar scheme and also considers apodization along the lateral expansion dimensions. Additionally Khajavi, Melati, Cheben, *et al.* [114] demonstrate the use of near field phase engineering to enhance the efficiency for small gratings by including a Bragg mirror. A Bragg mirror is a grating which has its band gap at the device operating wavelength, resulting in total reflection of incident fields. The mirror is useful for recovering non-upward diffraction. Notably, the results from [112] and [113] produce gratings which are integer orders of the resonant length without considering the length of the taper, on the order of 2λ.

Table 11: Comparison of small grating couplers for OPA.

Source	Grating Length μm	S11 (dB)	Bandwidth (nm)	Radiation Efficiency (%)
[112]	3.6	< -20	160	92
[113]	7.6	< -10	230	89
[114]	3.1	< -10	-	82
[42]	3.55[a]	-	-	51
[40]	3.55	-	-	50
[66]	3	-	-	30
[41]	3.55	-	-	20[a]

[a] Estimated where direct statement not available.

The design of gratings with dimensions of approximately 2λ was explored in simulation. Techniques from the design of modern gratings were applied. The definition of the grating used is shown in Figure 34 and features cells with secondary subwavelength structures and allowed apodization. A parameter sweep was performed for the grating definition before apodization. The designs were simulated for coupling at 0 degrees emission angle. A collection of design results for the uniform gratings are shown in Figure 35. Each data point in Figure 35 represents a unique design, where each of the unique designs has return loss better than -10 dB. All of these designs satisfy the representative foundry constraints. However, the upward diffraction efficiency is limited. This is expected as the total length for each design is less than 2λ at λ =

1550 nm and no mirror layers or structures are involved in recovering the non-upward diffraction. There is a design in the set which both maximizes the bandwidth and minimizes the return loss. The design parameters are $[L_1 = 813.75, L_2 = 90.42, L_3 = 501.54, L_4 = 116.79]$ However this must also be traded off against the upward diffraction efficiency.

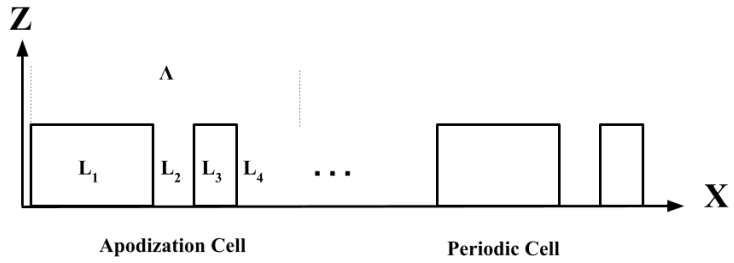

Figure 34: Grating definition inspired by modern literature of grating design

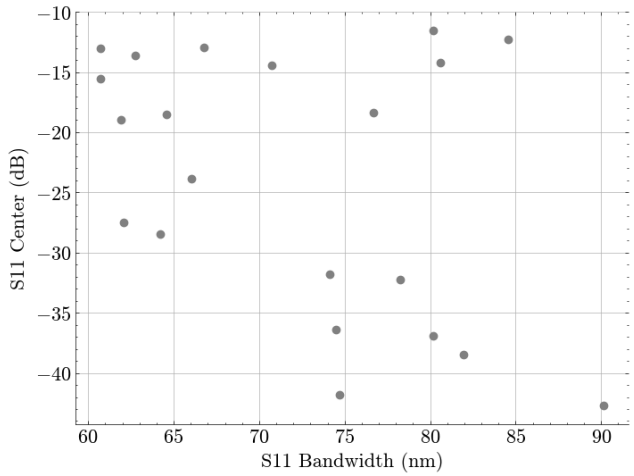

Figure 35: Results of 2D FDTD for uniform gratings with grating length less than 2λ and λ=1550nm. SOI thickness 220 nm, minimum feature size 70 nm and single etch.

The maximum theoretical efficiency of such a grating couplers is around 35% when increasing the number of periods, for example [44] discuss uniform gratings with this theoretical efficiency. Fatemi, Khachaturian, and Hajimiri [42] got around 50% efficiency at the same size scale by adding mirrors in the plane of the grating. While efficiencies of up to 90% are possible with the larger sizes and the inclusion of mirror structures [115]. However, compact designs with 90% efficiency are also possible, but require access to partial etching [112], transverse apodization [113], [114] and larger slab thickness.

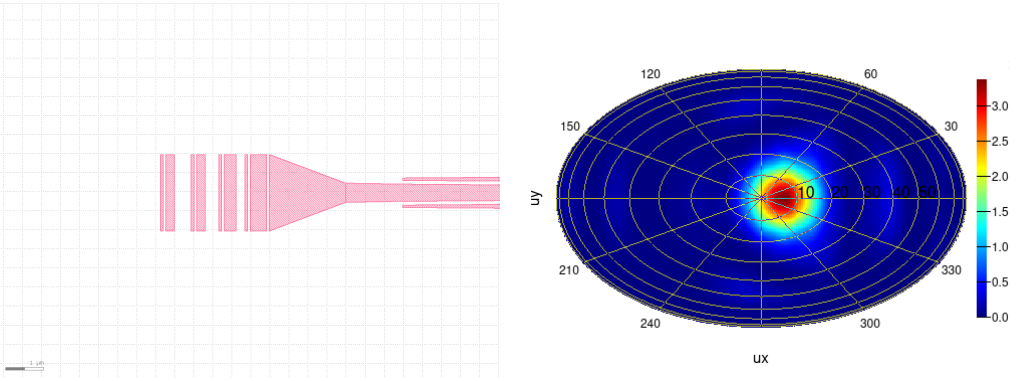

Figure 36: (left) Layout of apodized design. (right) Far field emission, arbitrary units. Grating length ≈ 2.8 x 2 um.

Figure 36 shows an apodized design variant with a Gaussian far field distribution. The design features a radiation efficiency of 20%, bandwidth of 100 nm. The design is competitive in bandwidth compared with literature Table 11. However the efficiency is at the low end of whats currently being achieved in research for similar scales of designs. It could be improved by the addition of mirrors or partial etching as with the other design which are achieving larger efficiencies.

4.3 Athermal Grating Couplers

One of the applications for the developed semi-analytic approach for athermal design of Bragg gratings [65] is in constraining the design and optimization of an athermal optical antenna. This is because the primary difference between a subwavelength waveguide and grating coupler is the pitch. As the pitch becomes greater than half the effective wavelength, the structure will radiate by means of diffraction of light. However, it is important to note that as the pitch increases, the approximation of the grating as an effective medium may not be valid if it exceeds the long-wavelength condition; Equation (2.47). The effective medium approximation is useful to constrain or seed an optimization in a numerical solver such as FDTD.

The first step is to find the approximate dimensions at which the subwavelength structure has net zero effective TOC, then using the Bragg condition find the pitch at which that structure will diffract light at the desired emission angle. Those parameters then can be used to seed an FDTD simulation where further optimization can be performed.

To demonstrate how this is done. The effective dispersion was first obtained by solving the band-structure

in FDTD. The geometric parameters for an approximately athermal grating were used in the simulation, Table 12. For SU8, Geometry 1 was applied. For OC-431A, Geometry 2 was applied. The geometry for both cases was estimated using Equation 3.4.

Geometry	DC (%)	W_1 (nm)	W_2 (nm)
1	42	200	490
2	42	310	490

Table 12: Geometric parameters of Bragg grating used for simulation of band structure.

Geometry	Cladding	n_{eff}	$\frac{dn_{eff}}{d\lambda}(nm^{-}1)$	$\frac{dn_{eff}}{dT}(K^{-}1)$
1	SiO_2	1.66	7.7E-4	1.8E-4
1	SU8	1.77	8.19E-4	0
2	SiO_2	1.95	1.12E-3	1.8E-4
2	OC-431A	1.95	1.12E-3	0

Table 13: Material properties of material stack for applied cladding at λ = 1550nm.

Geometry	Cladding	θ	$\Lambda(nm)$	$\lambda_{1dB}(nm)$
1	SiO_2	0	929.1	93.67
1	SU8	0	875.4	96.2
2	SiO_2	0	793.5	79.9
2	OC-431A	0	791.9	79.8

Table 14: Bandwidth and pitch of grating coupler with 0 degree emission for applied cladding at λ = 1550nm.

After obtaining the parameters that promote an athermal structure, the first order diffraction (M=1), pitch and bandwidth for the required emission angle may be calculated. Summarized in Table 14. The equivalent geometric structure with an SiO_2 cladding is compared to the athermal structure with alternative cladding. In specific cases, for example with SU8, the bandwidth of the grating coupler appears improved by being made athermal despite having a larger refractive index compared with SiO_2; shown in Table 13. While in the case of OC-431A, the parameters of the grating with an SiO_2 oxide may be maintained while improving the thermal dependence of the grating. Both cases may be advantageous.

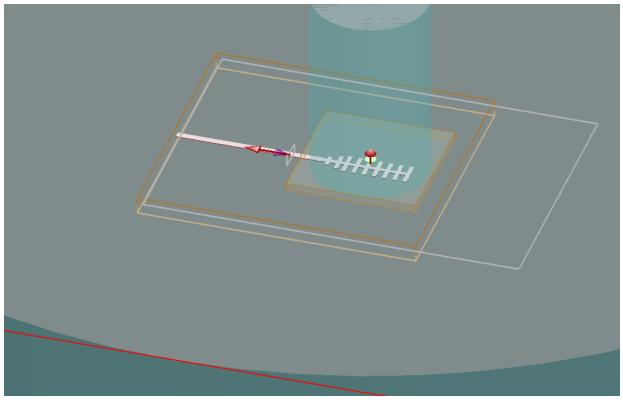

(a) FDTD Simulation.

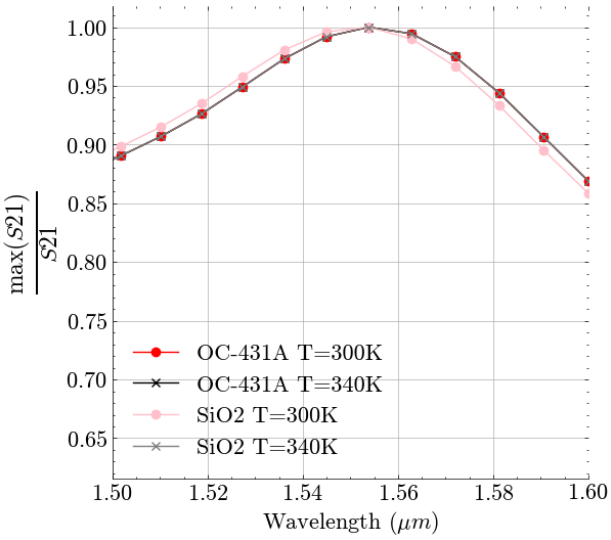

(b) Results of FDTD simulation.

Figure 37: Athermal Antenna $\approx 5x2\mu m$

.

An FDTD simulation was initialized with the parameters for Geometry 2 from Table 12. The pitch was adjusted to obtain 1550 nm center wavelength, and the design was simulated with thermal dependence of both SiO_2 and OC-431A, shown in Figure 37. From which it can be seen that with OC-431A, the bandwidth shifts less due to temperature compared with the reference SiO_2 design. However, the simulated efficiency was poor, and such a design may still require optimization depending on the efficiency requirements.

5 Experiments

5.1 Interferometers

Embedded in the layout are test structures to characterize the PIN modulator, and the TOC's of the augmented waveguides. These structures can be seen in Figure 31. The test structures are MZI. The generalized form for the transfer function for an MZI is defined in Equation 5.1. The derivation for this equation can be found in [71].

$$I_O = \frac{I_i}{4}\left|e^{-i\beta_1 L_1 - \frac{\alpha_1}{2}L1} + e^{-i\beta_2 L_2 - \frac{\alpha_2}{2}L2}\right|^2 \tag{5.1}$$

Specific variations of the MZI transfer function, Equation 5.1 intensity can be derived for either lossless, balanced, or imbalanced cases as this simply refers to the attenuation and propagation constants. In the lossless case $\alpha = 0$, in the balanced case $L1\beta_1 = L_2\beta_2$. Which may be used to simplify the generalization in Equation 5.1. Coherent measurements benefit from the use of these structures as the amplitude response can be used to infer phase. For an interferometer, the phase can be inferred by measuring the amplitude with a single photo-detector since the intensity response contains the phase information through the propagation constants. As shown in Equation (5.1).

The phase for the feed network of the phased array was tested with a coherent receiver, constructed from a balanced photo-detector. In this specific case the interferometer is constructed with a balanced detector. A balanced detector electronically mixes the amplitude response of two photo-diodes with equal responsivity. Internally the paths to the photo-diodes have balanced propagation paths, similar to the balanced case for the MZI. Balanced detectors ar commonly featured in coherent receivers as they suppress laser Relative Intensity Noise (RIN) and Amplified Spontaneous Emission (ASE) noise sources; typically described by their common mode rejection [116]. The principle of coherent detection in coherent receiver architectures is fundamentally related to the concept of interferometric analysis as the received signal is mixed with local oscillator to infer phase [117]. The transfer function of a balanced receiver is reproduced from Tang, Yi, and Shieh [117]. The received electric fields for a single polarization are represented as a complex amplitude modulated by a plane wave with the phase (ϕ) of the signal (S) and local oscillator (LO) in

Equations (5.2a) and (5.2b) respectively. The intermediate frequency (IF) of the detector is given in Equation (5.2c). The interference produced by the mixing in a balanced detector is the difference between the intensity of the signal and local oscillator. The difference is derived in Equation 5.2d and explicitly depends on the phase of the signal and local oscillator.

$$\vec{E}_S = \vec{A}_S e^{i\omega_s t + i\phi_s} \tag{5.2a}$$

$$\vec{E}_{LO} = \vec{A}_{LO} e^{i\omega_{LO} t + i\phi_{LO}} \tag{5.2b}$$

$$\omega_{IF} = \omega_S - \omega_{LO} \tag{5.2c}$$

$$I(t) = I_S - I_{LO} = 2R\sqrt{P_S(t)P_{LO}}cos(\omega_{if} t + \phi_S(t) - \phi_{LO}(t)) \tag{5.2d}$$

$$I(t) \overset{\omega_{IF}=0}{=} 2R\sqrt{P_S(t)P_{LO}}cos(\phi_S(t) - \phi_{LO}(t))) \tag{5.3}$$

In the homodyne configuration, the local oscillator and signal arm are mixed at the same frequency; Equation 5.3. In this condition the intermediate frequency is zero. However, in the homodyne condition This means that the phase information retrieved from the measurement has an inherent π ambiguity. Meaning the measurement is insensitive to whether the phase shift is positive or negative, since the phase is the argument of a cosine. For this reason the design of homodyne receiver considers two conditions. First $\phi_s - \phi_{LO} = 0$ the in-phase (I) component. Second, $\phi_s - \phi_{LO} = \frac{\pi}{2}$, the quadrature (Q) component. Two balanced receivers are often used to construct an IQ receiver to resolve the phase ambiguity. Two balanced detectors form I and Q channels by separating the phase by $\frac{\pi}{2}$. However this requires twice the hardware. In this thesis, a homodyne receiver was constructed with only one balanced detector.

5.2 Measurement Equipment

The measurement equipment is listed in Table 15. The equipment was arranged in either of two test configuration; Figures 38 and 39 respectively. These two test configurations represent if the interferometer was constructed off the wafer containing the OPA, or embedded in the chip containing the OPA. In either case Polarization Maintaining (PM) parts were used throughout the optical paths, and all components, including the splitter preserve the polarization. Polarization maintenance is required for the use of Equation 5.3 as it was derived explicitly for a single polarization.

Equipment	Manufacturer	Model
Analyzer	Keysight	InfiniiVision 3034A
Balanced Detector	Thorlabs	PDB470C
Cavity Laser	Thorlabs	SFL1550P
DAC	National Instruments	9264
DC Probe Array	Picoprobe	8 probe x 150 μm pitch
Fiber Array	Precision Micro-Optics	Lidless 8 PM probe x 127 μm pitch
Fiber Coupler	Thorlabs	PNH1550R5F2
Laser Controller	Thorlabs	CLD1015
Photodetector	Thorlabs	DET01CFC
PM Fiber	Thorlabs	PM1550-XP

Table 15: Measurement equipment.

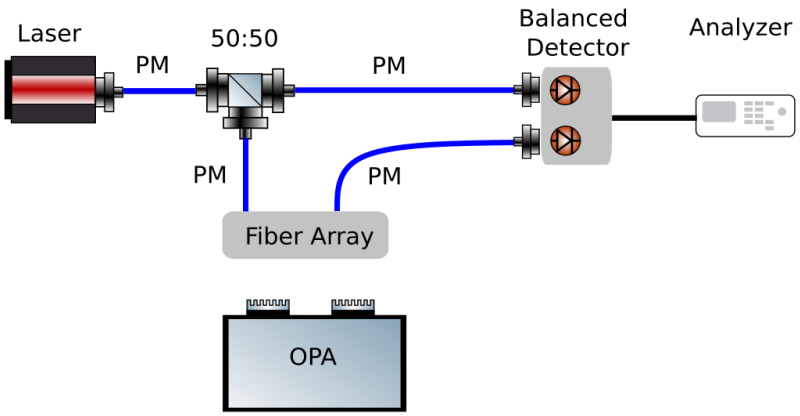

Figure 38: Homodyne test configuration of measurement equipment.

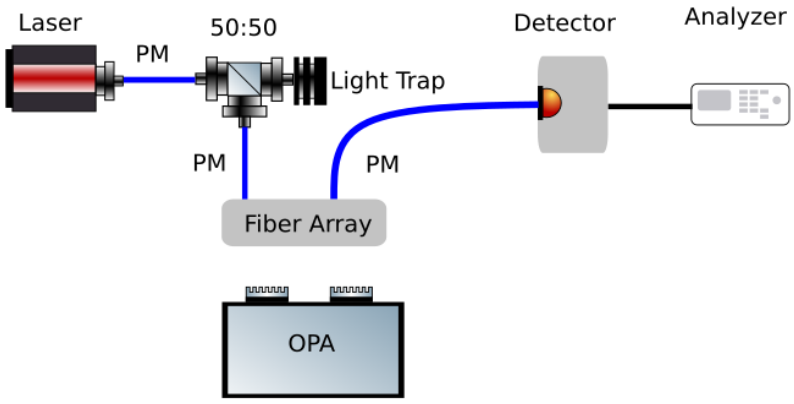

Figure 39: Embedded MZI test configuration of measurement equipment. The interferometer is embedded on the OPA.

To align the fibre array on the OPA, a probe station was constructed from translational stages. To heat the wafer, the author designed a custom PCB and heater controller. On the wafer heater there is an array of NTC thermistors for measuring the wafer temperature. The accuracy of the sensors is $\pm 0.5C$. The sensor closest to the design variant can be selected and a PID algorithm sets the target temperature based on feedback from the target sensor. Testing the device required aligning both a DC probe array on the bond pads for the phase modulator, and aligning a fibre array on the grating couplers for input and output. After alignment, coordination of the measurement equipment was achieved by a custom probe station software designed by the author Figure 41.

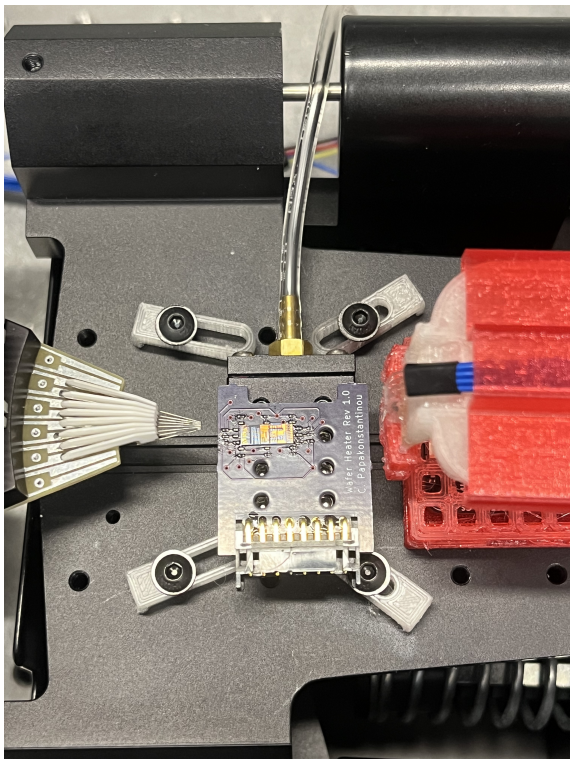

(a) Wafer Heater

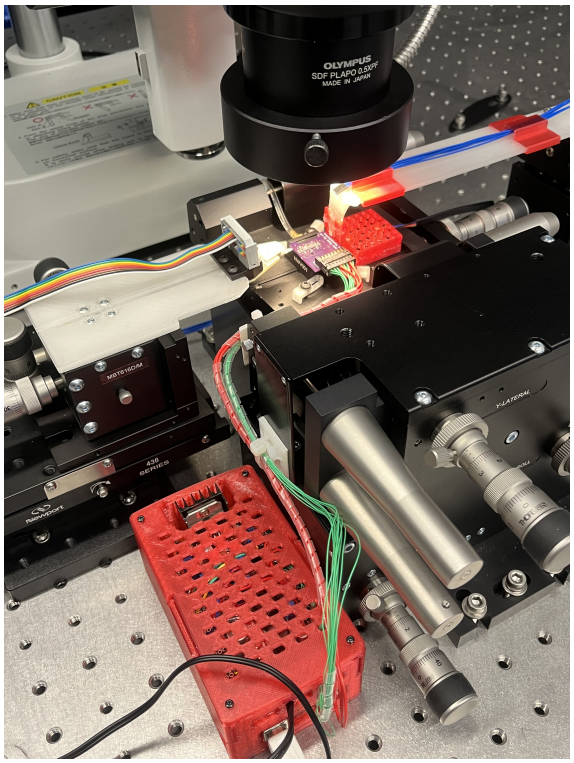

(b) Controller

The probe station software was designed to manage the measurement equipment for three kinds of tests. Each test has a unique sequence where raw measurements from the equipment are recorded to a database. Analysis of the tests queries the measured data and fits a transfer function derived for the interferometer. The transfer function is fit by least squares for the parameters of interest. In the $V\pi$ test, the change in the refractive index is estimated. In the TOC test the thermo-optic coefficient is estimated Finally in homodyne test, the relative phase is estimated.

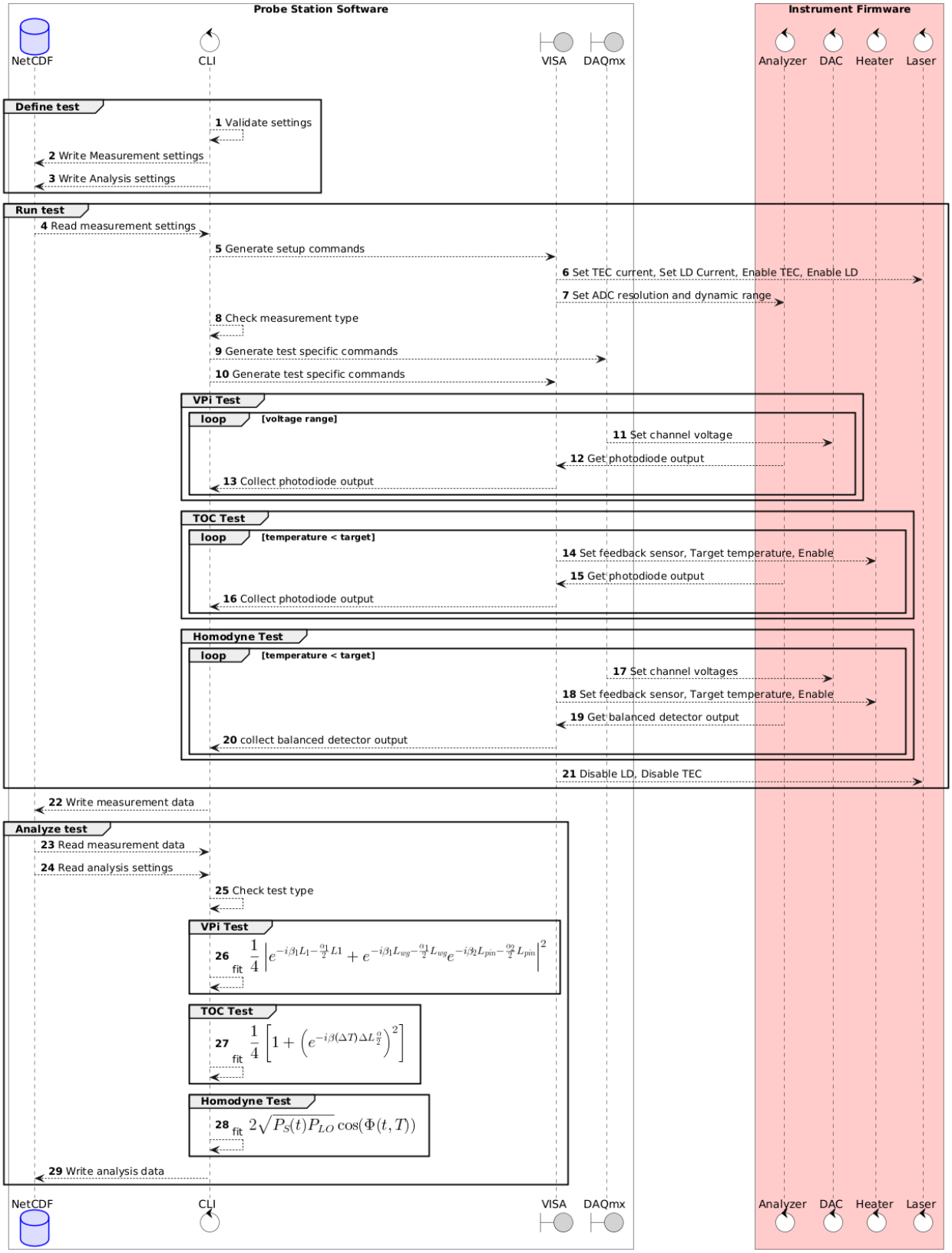

Figure 41: Probe station sequence Diagram.

5.3 $V\pi L$

For characterizing the phase modulator, the requirement was measuring the refractive index; as the real and imaginary components describe the time delay and attenuation for an applied voltage. The primary figure of merit is the $V\pi$, the voltage at which a π phase shift is achieved; Section 2.2.2. This test results in a calibration table by which known phase shifts can be actively introduced in each of the phased array channels. Which may be achieved by a bias voltage applied to the phase modulator. The test structure for characterizing the PIN modulator is an MZI where one of the arms contains the waveguide with a PIN junction. The test structure was modelled in Lumerical interconnect using the SiEPIC and AMF PDK. It represents the routing length and elements used in the layout; Section 3.3.2. The simulation also reflects the experiment configuration, Figure 39, where the laser block contains the power and linewidth of the cavity laser.

The transfer function for this device was derived by the author. It can be seen that there are passive waveguides preceding and following the active waveguide which need to be included in the model for the MZI in Equation 5.1. Here the terms $e^{-i\beta_1 L_{wg} - \frac{\alpha_1}{2} L_{wg}} e^{-i\beta_2 L_{pin} - \frac{\alpha_2}{2} L_{pin}}$ represent the arm of the MZI containing the passive waveguides and PIN modulator. While the term $e^{-i\beta_1 L_1 - \frac{\alpha_1}{2} L1}$ represents the arm with only a passive waveguide. The addition of the terms were included in the transfer function model, Equation 5.4.

$$\frac{I_O}{I_i} = \frac{1}{4} \left| e^{-i\beta_1 L_1 - \frac{\alpha_1}{2} L1} + e^{-i\beta_1 L_{wg} - \frac{\alpha_1}{2} L_{wg}} e^{-i\beta_2 L_{pin} - \frac{\alpha_2}{2} L_{pin}} \right|^2 \tag{5.4}$$

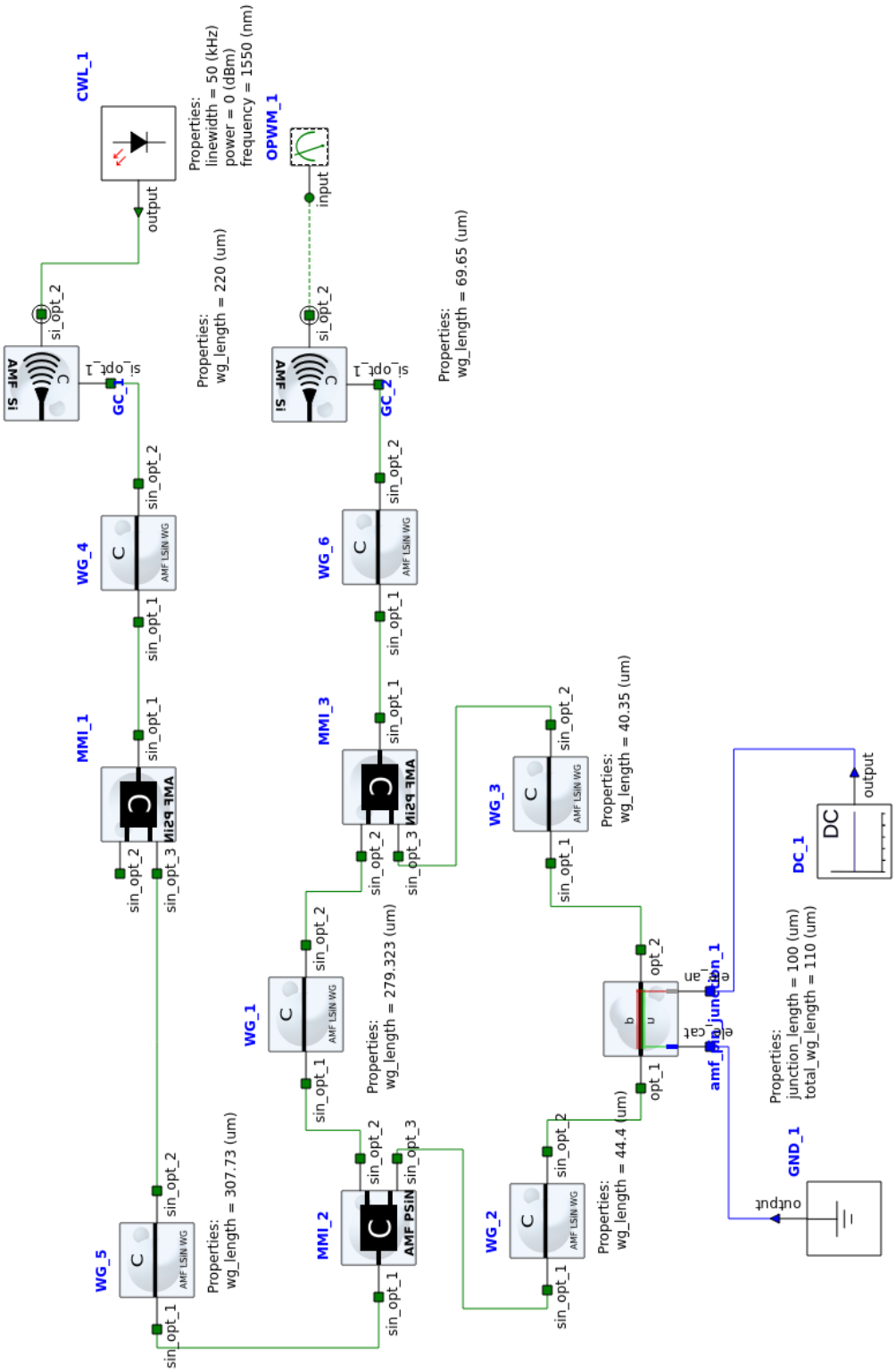

Figure 42: Lumerical Interconnect model of the MZI with PIN junction in arm.

The simulation of the PIN modulator was used to estimate the change in the real and imaginary coefficients of the waveguide with voltage. The output of the MZI was measured with a photo-diode for a range forward bias voltages applied to the PIN modulator. The obtained curve was fitted against the derived transfer function model to obtain the experimental change of the real and imaginary components of the refractive index. The raw data and the fit model are shown in Figure 43. The uncertainty in the measured power is from the Analyzer, 2% of the full scale voltage which was set to 200 mV. The uncertainty in the applied bias is from the DAC, 1% of the range which was fixed at 10.5 V.

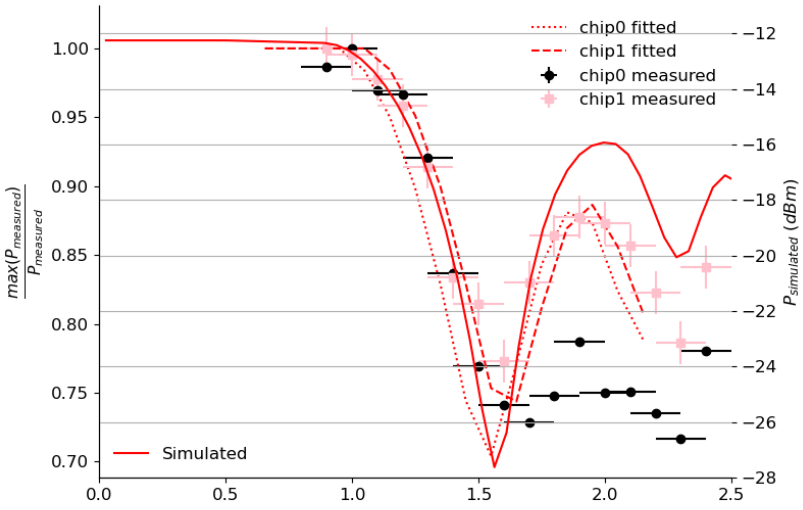

Figure 43: Transfer function fitted to experiment data.

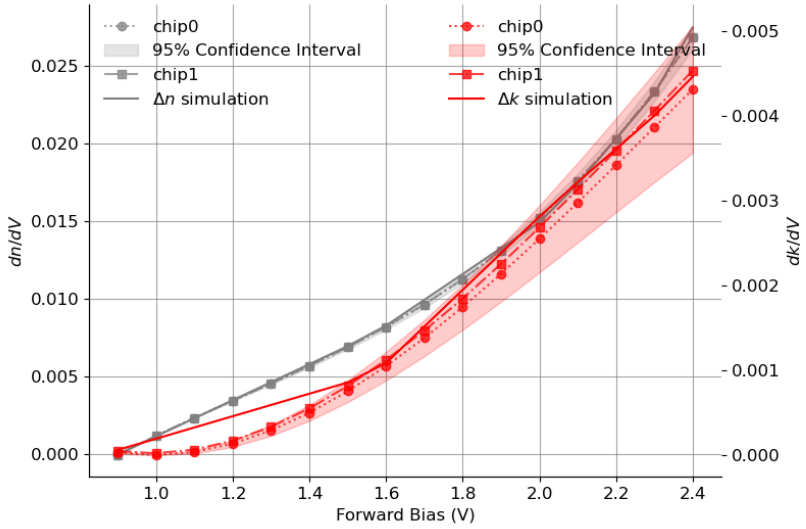

Figure 44: Transfer function estimates of the change in refractive index as a function of voltage.

Voltage (V)	Simulated $\frac{(\Delta\phi)}{\pi}$	Measured $\frac{(\Delta\phi)}{\pi}$
1.1	0.30	0.30±0.002
1.2	0.45	0.45±0.005
1.3	0.60	0.59±0.008
1.4	0.75	0.73±0.012
1.5	0.90	0.89±0.017
1.6	1.07	1.06±0.022
1.7	1.28	1.25±0.028
1.8	1.50	1.45±0.035
1.9	1.71	1.69±0.042
2	1.93	1.96±0.051

Table 16: PIN modulator change in phase as a function of voltage. Normalized by $\frac{1}{\pi}$.

As a result of the experiment, the change in refractive index was obtained, shown in Figure 44. The fitted coefficients were used to calculate the phase change as a function of voltage by applying Equation 2.9a. The $V\pi$ was then obtained per the relation in Equation 2.11. The PIN junction modulator has a π phase shift at approximately 1.55 V corresponding to a VπL of 0.048 V-cm. The deviation between measurements of

the test structure on different wafer copies was small using the analysis method described above, less than 1%. The VπL obtained is comparable with the efficiency for similar modulators in literature. Patel, Ghosh, Chagnon, *et al.* fabricated a lateral PIN junction modulator on SOI obtaining 0.058 V-cm [118]. The measurement.

5.4 Thermo-Optic Coefficient

For characterizing the TOC of the custom waveguides, the TOC was directly obtained by fitting the interferometer output. The test structure is an imbalanced MZI, $L_1 \neq L_2$ with identical waveguides, $\beta = \beta_1 = \beta_2$ and $\alpha = \alpha_1 = \alpha_2$. The transfer function was derived by the author by substitution of a temperature dependence term into Equation 5.1. The thermal dependence of the refractive index, Equation 2.7 was included in Equation 2.3 to represent the temperature dependence. Equation (5.5) was substituted into Equation (5.1) to obtain Equation (5.6). Which provides an explicit means to fit the TOC.

$$\beta(\Delta T) = \frac{2\pi(n + \frac{dn}{dT}\Delta T)}{\lambda} \tag{5.5}$$

$$\frac{I_0}{I_i} = \frac{1}{4}\left[1 + (e^{-i\beta(\Delta T)\Delta L\frac{\alpha}{2}})^2\right] \tag{5.6}$$

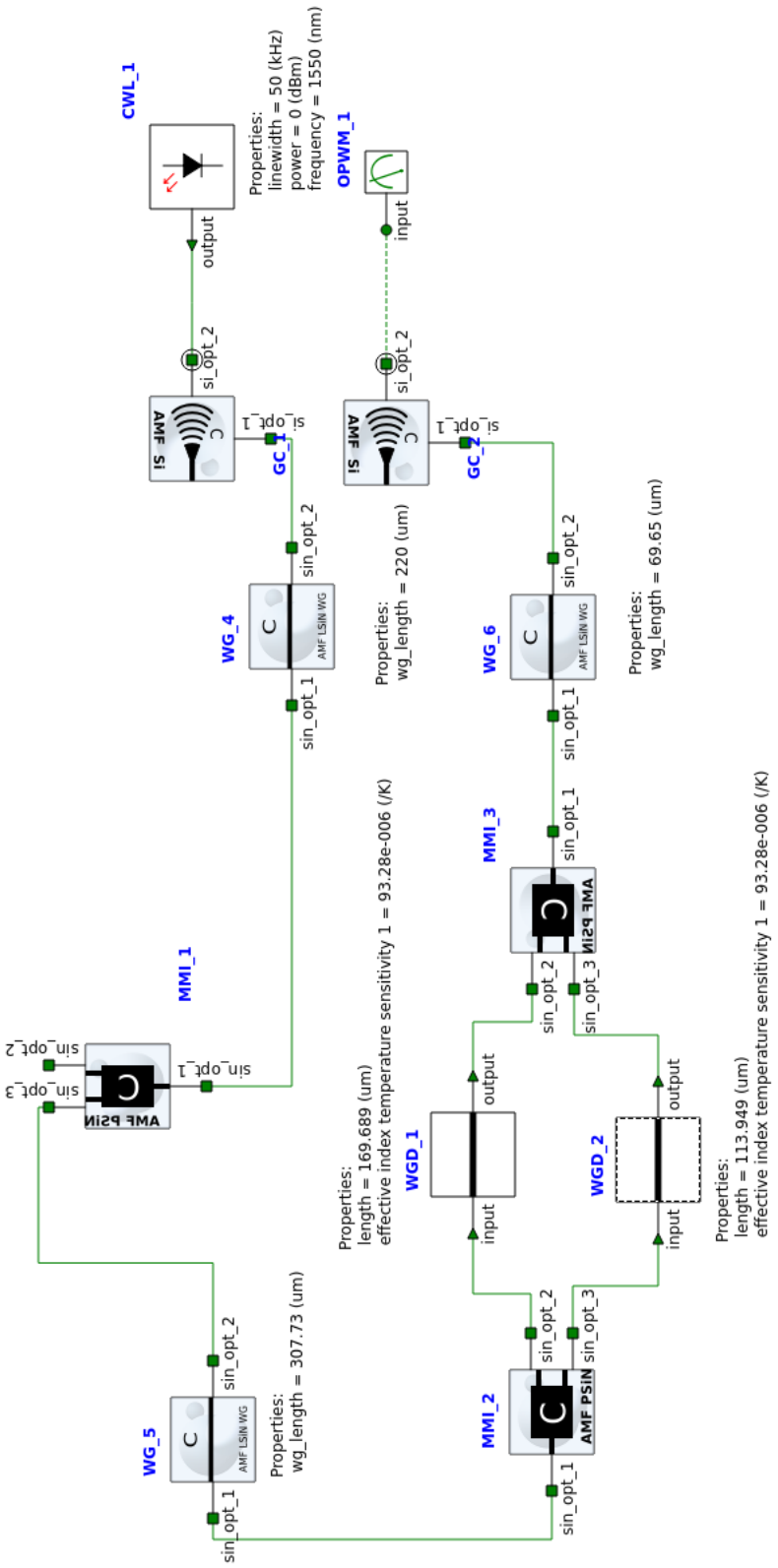

Figure 45: Lumerical Interconnect model of the MZI with OC-431A cladding on balanced 410 nm strip waveguides.

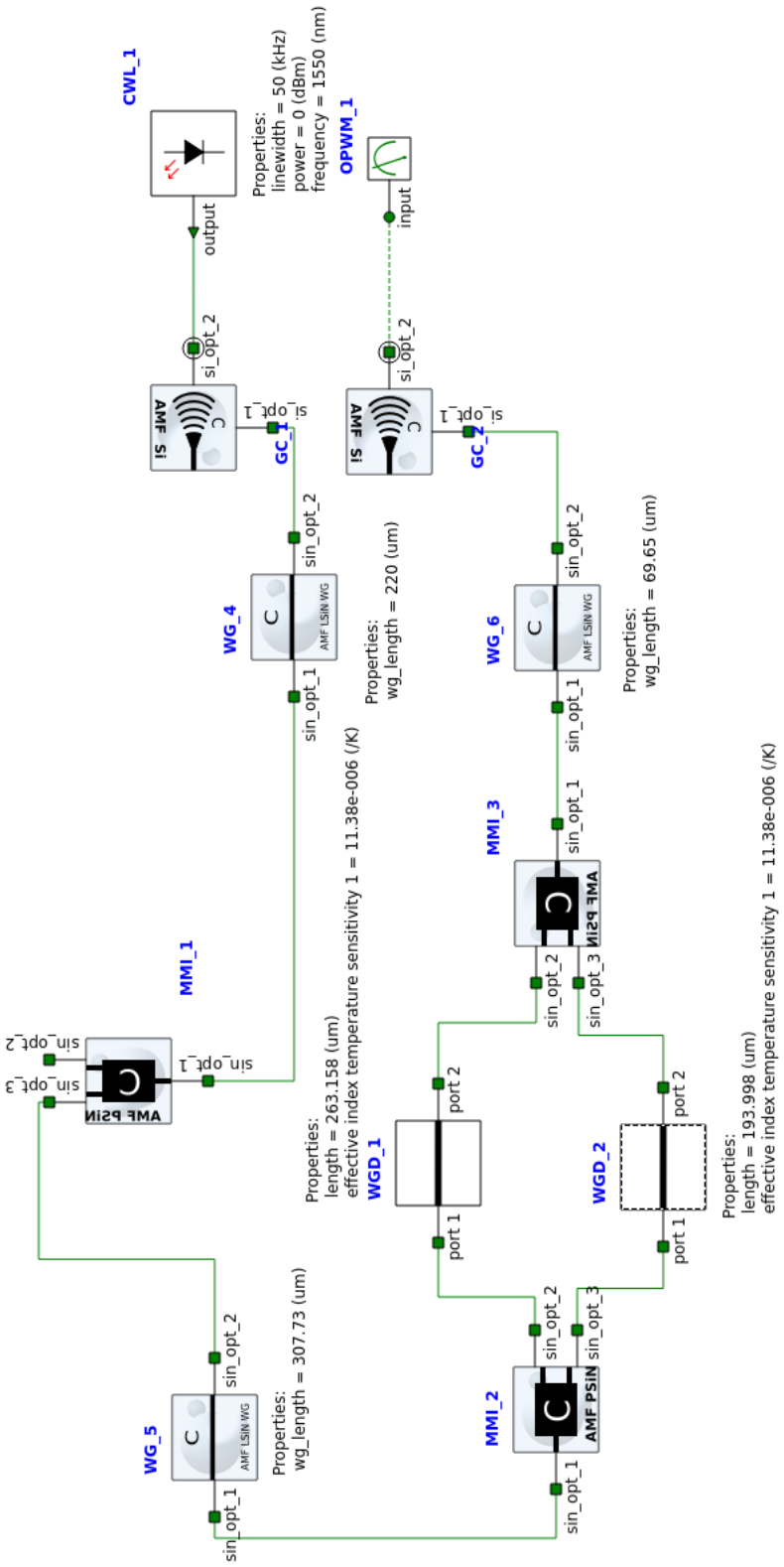

Figure 46: Lumerical Interconnect model of the MZI with OC-431A cladding on balanced 410x250 nm rib waveguides.

The waveguides have an open oxide region where the cladding layer was replaced. The cladding was replaced with Nye Lubricants OC-431A. Which is available as a commercial off the shelf part, from Thorlabs as G608N3. The properties are shown in Table 17. The material was applied to the surface with a doctor blade. the position of the doctor blade was adjusted for a 2 μm coating thickness. The coating applied was not uniform of the entire surface of the chip, shown in Figure 47, however the primary function of the coating is to fill the open oxide regions and uniformity over the surface of the chip was not required.

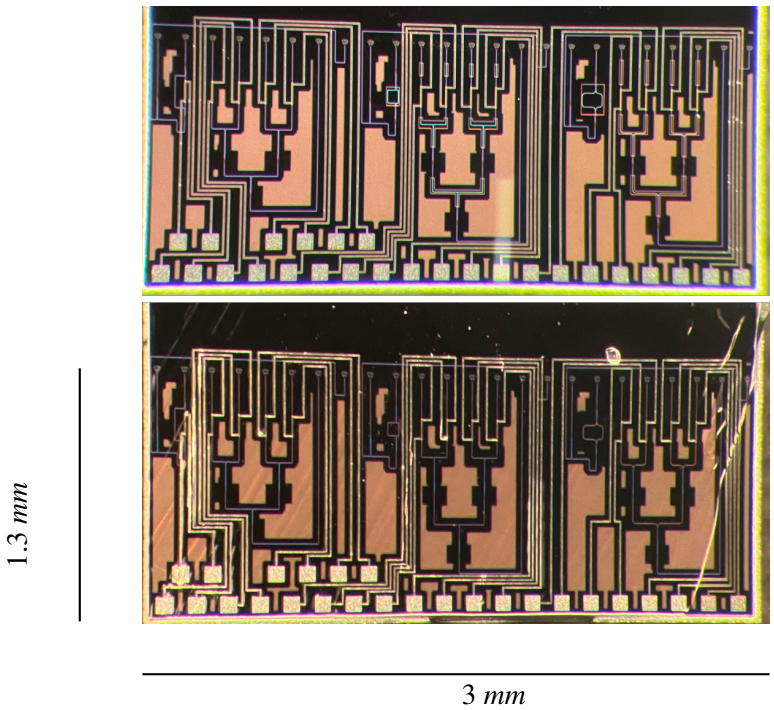

Figure 47: (Top) Microscope image of chip before coating. (Bottom) Microscope image of chip after coating.

material	n	$\frac{dn}{dT}(K^{-}1)$	$C_{TE}(K^{-}1)$
OC-431A	1.4378	-3.5E-4	6E-4

Table 17: Material properties of cladding polymer at 25C and λ = 1550nm.

The output of the MZI was measured with a photo-diode for a range temperatures applied to the wafer. A temperature perturbation of 10C was applied, as the TOC non-linearity is small, approximately 3E-6 in this range, per Table 2. The obtained curve was fitted against the derived transfer function to obtain the experimental change of the of the refractive index. The results are shown in Table 18. The measured results on average agreed with the process-biased simulation, Section 3.2.1, and generally was within the bounds of the manufacturing variation, Figure 20b and 21b. The strip waveguide case had a much larger deviation

than the rib waveguide. This is likely due to the core confinement being stronger in the strip waveguide case. In practice roughness at the material interface will cause scattering, Section 2.3.7 and this effect is pronounced for strongly confined cores, whereas in lower confinement core the field propagates more freely in the cladding. There is also some contribution from the temperature uncertainty on the variance. As the thermo-optic coefficient is not strictly linear Section 2.1, and the temperature sensor accuracy is $0.5C$.

Design	Simulated $\frac{dn_{eff}}{dT}(K^{-}1)$	Measured $\frac{dn_{eff}}{dT}(K^{-}1)$
2	$9.328E\text{-}5^{+0.66E\text{-}5}_{-2.41E\text{-}5}$	9.39E-5 $\pm$ 4.55E-5
3	$1.139E\text{-}5^{+4.74E\text{-}5}_{-5.91E\text{-}5}$	1.12E-5 $\pm$ 1.11E-5

Table 18: Measured and simulated thermo-optic coefficent at λ = 1550nm

5.5 Optical Phased Array Feed Network

The feed network was measured with a balanced detector in the homodyne configuration. The author derives a case of the homodyne detector that can be fit for a temperature perturbation of the OPA feed network. To begin, recall Equation (5.3). Suppose that the phase of the local oscillator and signal are a function of both time and temperature, then represent the mixed phase term with Φ as in Equation (5.7a). Substitution of the term back in to Equation (5.3) obtains the transfer function, Equation (5.7b) with a temperature and time dependence. P_S and P_{LO} are measured by the analyzer and the phase with respect to the local oscillator may be fit by least squares.

$$\Phi(T,t) = \phi_S(T,t) - \phi_{LO}(T,t) \tag{5.7a}$$

$$P(t) = \sqrt{P_S(t)P_{LO}}cos(\Phi(t,T))) \tag{5.7b}$$

The phase change of the signal arm due to temperature may be extracted from the fit by use of a time series differencing. To derive this, the phase of the local oscillator is approximated as constant with respect to

time, and temperature, $\phi_{LO}(t,T) = \phi_{LO}$. The local oscillator arm of the interferometer is independent of temperature because with the arm is independent of the wafer and not subject to the same temperature perturbation. Then the difference in phase over time and temperature is taken with respect to the time and temperature and initialization of the measurement. That is, $t = t_0,\ T = T_0$ as in Equations (5.8) which represents the simulation, and Equation (5.9a) which represents the measurement. In the case of Equation (5.9a), it represents the phase observed at the balanced detector. The equation can be expanded as in Equation (5.9b), in this case, taking the difference in phase over time and temperature eliminates the local oscillator term. This is true provided the local oscillator is approximated as constant.

$$\Delta\phi_{sim} = |\phi_{sim}(T = T_0, t = t_0) - \phi_{sim}(T,t)| \tag{5.8}$$

$$\Delta\Phi_{measured} = |\Phi(T = T_0, t = t_0) - \Phi(T,t)| \tag{5.9a}$$

$$\Delta\Phi_{measured} = |\phi_{LO} - \phi_S(t = t_0, T = T_0) - \phi_{LO} - \phi_S(t,T)| \tag{5.9b}$$

$$\Delta\Phi_{measured} = |\phi_S(t = t_0, T = T_0) - \phi_S(t,T)| \tag{5.9c}$$

Furthermore, when comparing the phase change, the time series between adjacent channels was used. This is because the initialization phases can also be dropped out, simplifying the comparison between the measured and simulated cases. As the initialization phases for the measured and simulated data are not necessarily equal, $\phi_{sim}(T_0,t_0) \neq \phi_S(T_0,t_0)$. To obtain the simulated change in phase over temperature, the OPA feed networks were modelled in Lumerical Interconnect using the SiEPIC and AMF PDKs. Waveguide models with the simulated temperature dependence were applied. The Interconnect model is shown in Figure 48. Compact models of the custom waveguides were used to connect the PDK elements, the compact models of the waveguides contain the simulated thermal dependence of the waveguides.

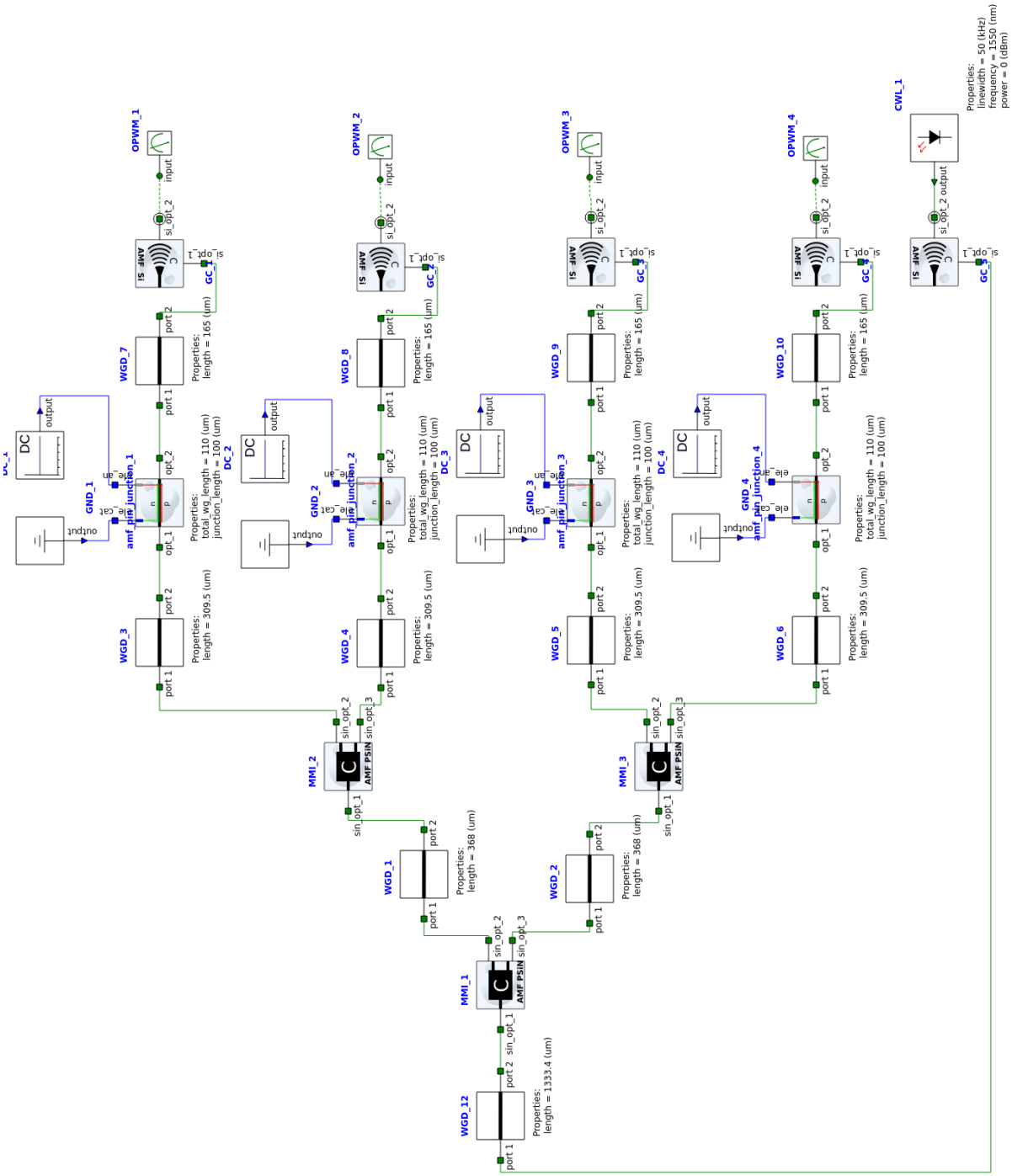

Figure 48: Lumerical Interconnect model of OPA feed network.

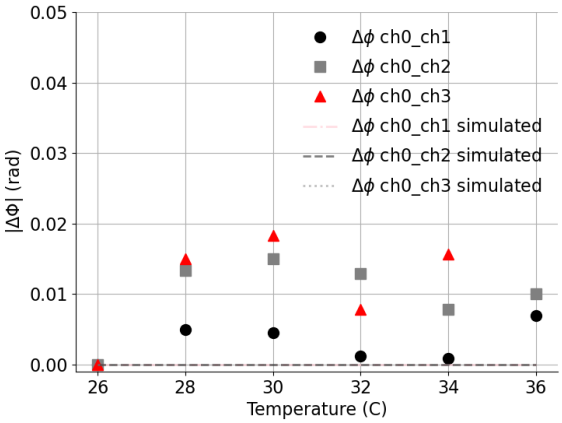

(a) Design 2.

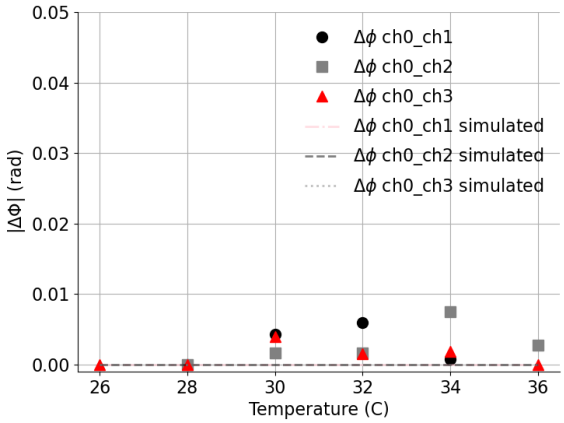

(b) Design 3.

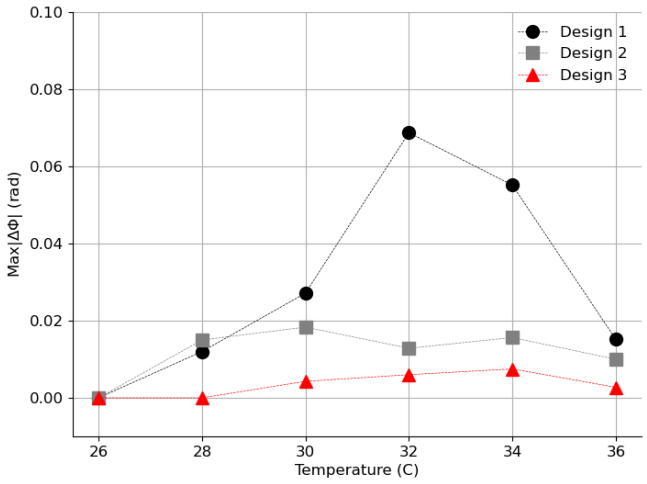

(c) Maximum observed phase difference between channels for all designs.

Figure 49: Phase drift between reference channel and adjacent channels as a function of temperature for uniform temperature change.

The measured phase was obtained during heating the wafer. The measured and simulated results for the design variants are shown in Figure 49a for Design 2, and 49b for Design 3. In this figure the temperature time series and phase time series were binned and averaged within the nearest temperature, time is an implicit dimension but not explicitly shown. The phase diverges before settling at the end of the heating period. This is believed to be due to non-uniform temperature change of the wafer during the heating cycle. However, it can be seen in Figure 49c that when looking at the maximum phase drift over the temperature range that the design with the lowest thermal dependence experience the smallest phase divergence.

6 Conclusion

6.1 Concluding Remarks

To the best of the authors knowledge, this work represents the first demonstration of an Optical Phased Array (OPA) implemented on Silicon on Insulator (SOI) which is temperature stable by means of the combined use of athermal design, phase symmetry, and Electro-Optic (EO) phase modulation.

The post-foundry procedures for the athermal design were applicable to Multi Project Wafer (MPW) runs, as the requirement for an open-oxide region was supported by Advanced Micro Foundry (AMF). The materials required to replace the cladding were commercially available as off-the-shelf optical parts; such as OC-431A. The Thermo-Optic Coefficient (TOC) of the SOI waveguides were reduced by an order of magnitude with respect to silicon in both simulation and test in Section 5.4.

The optical phase symmetry conditions were derived by the author and are shown to be scalable between linear and dense arrays in Section 3.3.1. An optically phase symmetric linear OPA layout was manufactured through AMF's MPW. The relative phase between emitters was maintained in a temperature sweep experiment in Section 5.5. Where a phase separation of less than 2 degrees was observed for the designs with custom waveguides.

Previous work in the area of thermal management deals with modulator-to-modulator distance. Both Wang, Liang, Chen, *et al.* [47] and Yepez, Scholz, Caspers, *et al.*[45] claimed modulator-to-modulator distances could be reduced to 3 μm without significantly changing the cross talk. The change in temperature gradient supporting this claim was an order of magnitude, which is equivalent with reducing the thermal dependence by the same scale. Such a demonstration was given in simulation and test given typical MPW constraints; Section 3.2. Furthermore at 3 μm the waveguides still have better than 50 dB of cross talk isolation for parallel traces with lengths at a scale of 100 μm.

Furthermore, the author derived a semi-analytic approach for the athermal design of subwavelength waveguides based on Bragg gratings in Section 3.2.1. The approach was used to show how the optimization of an athermal antenna could be constrained in Section 4.3.

6.2 Limitations of Thesis and Future Work

In this study, the use of athermal design was limited to waveguides and antennas. Although small athermal antennas were explored in simulation, the optimization and fabrication of these devices is outstanding. Since OPAs feature other integral components such as phase modulators and power splitters, the athermal design of those components should also be considered. As the temperature sensitivity in optical wave guiding devices depends explicitly on the length, the next largest components of the OPA should also be treated with athermal design. That is the phase shifter and power splitters should also be made athermal. An athermal directional coupler could be made using the custom waveguide cores as an alternate to the Multi-Mode Interferometer (MMI) used in the feed network designed for this study. Regarding athermal phase modulators, future considerations include removing the thermal sensitivity of the phase shifters by athermal design [119], [120]. Alternative to plasma dispersion techniques, obtaining a linear EO by use of polymers on slot waveguides has been demonstrated by Steglich, Mai, Villringer, *et al.* [121]. Slot waveguides may also be made athermal, demonstrated by Lee, Kim, Kim, *et al.*[62]. It is possible to consider making the polymer for obtaining an EO effect function as the thermal compensation layer. In the work of Steglich, Mai, Villringer, *et al.*, PMMA was used. PMMA has a TOC of approximately -1.3E-4 [51].

In this study layout of the OPA was limited to linear arrays and the design of a feed network. Future designs should pitch the antennas closer together using small antennas designed for vertical and free space emission rather than the large PDK grating couplers which were designed for fibre coupling. Then the feed network to those antenna designs could be routed for free space testing of the beam control. Furthermore, dense architectures should be demonstrated by following the optical symmetry conditions in Section 3.3.1.

References

[1] J. Wertz and W. J. Larson, *Space Mission Analysis and Design* (Space Technology Library), 3rd edition. Boston MA: Microcosm Press and Springer, 1999, 976 pp.

[2] S. Lambert and W. Casey, *Laser Communications in Space* (Artech House optoelectronics library). Artech House, 1995.

[3] K. S. Sebacher, S. G. Lambert, J. A. Pautler, and J. P. Carter, "Laser crosslink configurations for RF satellite communications systems," in *MILCOM 1985 - IEEE Military Communications Conference*, vol. 1, Oct. 1985, pp. 98–103.

[4] R. G. Marshalek, G. S. Mecherle, and P. Jordan, "System-level comparison of optical and rf technologies for space-to-space and space-to-ground communication links circa 2000," eng, in *Proceedings of SPIE*, vol. 2699, SPIE, 1996, pp. 134–145.

[5] W. D. Williams, M. Collins, D. M. Boroson, *et al.*, "RF and optical communications: A comparison of high data rate returns from deep space in the 2020 timeframe," Mar. 1, 2007.

[6] M. Toyoshima, "Recent trends in space laser communications for small satellites and constellations," presented at the IEEE International Conference on Space Optical Systems and Applications, Oct. 2019, pp. 1–5.

[7] M. Toyoshima, "Applicability of space laser communications for low earth orbit satellite constellations," in *Optical Fiber Communication Conference (OFC) 2022 (2022), paper M1B.3*, Optica Publishing Group, Mar. 6, 2022, M1B.3.

[8] P. Muri and J. McNair, "A survey of communication sub-systems for intersatellite linked systems and CubeSat missions," *Journal of Communications*, vol. 7, no. 4, pp. 290–308, Apr. 1, 2012.

[9] S. C. Burleigh, T. De Cola, S. Morosi, S. Jayousi, E. Cianca, and C. Fuchs, "From connectivity to advanced internet services: A comprehensive review of small satellites communications and networks," *Wireless Communications and Mobile Computing*, vol. 2019, no. 1, p. 6 243 505, 2019.

[10] R. Radhakrishnan, W. W. Edmonson, F. Afghah, R. M. Rodriguez-Osorio, F. Pinto, and S. C. Burleigh, "Survey of inter-satellite communication for small satellite systems: Physical layer to network layer view," *IEEE Communications Surveys & Tutorials*, vol. 18, no. 4, pp. 2442–2473, 2016, Conference Name: IEEE Communications Surveys & Tutorials.

[11] H. Hauschildt, N. l. Gallou, S. Mezzasoma, *et al.*, "Global quasi-real-time-services back to europe: EDRS global," in *International Conference on Space Optics — ICSO 2018*, vol. 11180, SPIE, Jul. 12, 2019, pp. 353–357.

[12] D. Tröndle, P. M. Pimentel, C. Rochow, *et al.*, "Alphasat-sentinel-1a optical inter-satellite links: Run-up for the european data relay satellite system," in *Free-Space Laser Communication and Atmospheric Propagation XXVIII*, vol. 9739, SPIE, Mar. 15, 2016, p. 973 902.

[13] Y. Satoh, Y. Miyamoto, Y. Takano, S. Yamakawa, and H. Kohata, "Current status of japanese optical data relay system (JDRS)," in *2017 IEEE International Conference on Space Optical Systems and Applications (ICSOS)*, Nov. 2017, pp. 240–242.

[14] T. Tadono, Y. Mizukami, H. Watarai, J. Takaku, F. Ohgushi, and H. Kai, "CALIBRATION AND VALIDATION OF THE ADVANCED LAND OBSERVING SATELLITE-3 "ALOS-3"," *The International Archives of the Photogrammetry, Remote Sensing and Spatial Information Sciences*, vol. XLIII-B1-2020, pp. 135–140, Aug. 6, 2020, Conference Name: XXIV ISPRS Congress, Commission I (Volume XLIII-B1-2020) - 2020 edition Publisher: Copernicus GmbH.

[15] Y. Arikawa, Y. Kankaku, T. Motooka, and C. Kato, "ALOS-4 launch and early orbit operation result," in *Earth Observing Missions and Sensors: Development, Implementation, and Characterization VI*, vol. 13267, SPIE, Jan. 10, 2025, pp. 32–38.

[16] T. S. Rose, D. W. Rowen, S. LaLumondiere, *et al.*, "Optical communications downlink from a 1.5u cubesat: OCSD program," in *International Conference on Space Optics — ICSO 2018*, vol. 11180, SPIE, Jul. 12, 2019, pp. 201–212.

[17] B. L. Edwards, B. Robinson, A. Biswas, and J. Hamkins, "An overview of NASA's latest efforts in optical communications," in *2015 IEEE International Conference on Space Optical Systems and Applications (ICSOS)*, Oct. 2015, pp. 1–8.

[18] D. J. Israel, B. L. Edwards, R. L. Butler, *et al.*, "Early results from NASA's laser communications relay demonstration (LCRD) experiment program," in *Free-Space Laser Communications XXXV*, H. Hemmati and B. S. Robinson, Eds., San Francisco, United States: SPIE, Mar. 15, 2023, p. 2.

[19] C. Deprez and G. Giorgi, “Operational envelope and link scheduling for inter-satellite links in next-generation GNSSs,” in *2021 IEEE Aerospace Conference (50100)*, ISSN: 1095-323X, Mar. 2021, pp. 1–13.

[20] G. Giorgi, B. Kroese, and G. Michalak, “Future GNSS constellations with optical inter-satellite links. preliminary space segment analyses,” in *2019 IEEE Aerospace Conference*, ISSN: 1095-323X, Mar. 2019, pp. 1–13.

[21] G. Michalak, S. Glaser, K. H. Neumayer, and R. König, “Precise orbit and earth parameter determination supported by LEO satellites, inter-satellite links and synchronized clocks of a future GNSS,” *Advances in Space Research*, Scientific and Fundamental Aspects of GNSS - Part 2, vol. 68, no. 12, pp. 4753–4782, Dec. 15, 2021.

[22] R. M. Calvo, J. Poliak, J. Surof, and R. Wolf, “Evaluation of optical ranging and frequency transfer for the kepler system : Preliminary laboratory tests,” in *2020 European Navigation Conference (ENC)*, Nov. 2020, pp. 1–9.

[23] I. Del Portillo, B. G. Cameron, and E. F. Crawley, “A technical comparison of three low earth orbit satellite constellation systems to provide global broadband,” *Acta Astronautica*, vol. 159, pp. 123–135, Jun. 2019.

[24] C. Carrizo, M. Knapek, J. Horwath, D. D. Gonzalez, and P. Cornwell, “Optical inter-satellite link terminals for next generation satellite constellations,” in *Free-Space Laser Communications XXXII*, vol. 11272, SPIE, Mar. 2, 2020, pp. 8–18.

[25] S. Laverty, W. C. Chong, J. Osborne, M. Mitry, and V. Lewis, “The kepler satellite system,” in *Handbook of Small Satellites: Technology, Design, Manufacture, Applications, Economics and Regulation*, J. N. Pelton and S. Madry, Eds., Cham: Springer International Publishing, 2020, pp. 1075–1090.

[26] J. Rainbow. “Kepler demonstrates optical data relay service in LEO,” SpaceNews. (Jun. 11, 2024), [Online]. Available: `https://spacenews.com/kepler-demonstrates-optical-data-relay-service-in-leo/` (visited on 11/07/2024).

[27] "Kepler validates SDA-compatible optical technology for space data relay constellation – kepler." (Jun. 11, 2024), [Online]. Available: https://kepler.space/kepler-validates-sda-compatible-optical-technology-for-space-data-relay-constellation/ (visited on 11/07/2024).

[28] "Starlink latency," Starlink. (Feb. 12, 2024), [Online]. Available: https://www.starlink.com/public-files/Commitment%20to%20Space%20Sustainability.pdf (visited on 01/17/2025).

[29] "Starlink latency," Starlink. (Mar. 7, 2024), [Online]. Available: https://www.starlink.com/public-files/StarlinkLatency.pdf (visited on 01/17/2025).

[30] N. Yared and G. Jansson, "Telesat lightspeed: Enabling mesh network solutions for managed data service flexibility across the globe," in *Free-Space Laser Communications XXXV*, vol. 12413, SPIE, Mar. 15, 2023, pp. 42–52.

[31] "Telesat and MDA space complete key milestone for telesat lightspeed constellation telesat." (Dec. 4, 2024), [Online]. Available: https://www.telesat.com/press/press-releases/telesat-and-mda-space-complete-key-milestone-for-telesat-lightspeed-constellation/ (visited on 01/17/2025).

[32] S. Arnon, S. Rotman, and N. S. Kopeika, "Beam width and transmitter power adaptive to tracking system performance for free-space optical communication," *Applied Optics*, vol. 36, no. 24, pp. 6095–6101, Aug. 20, 1997, Publisher: Optica Publishing Group.

[33] S. Arnon, S. R. Rotman, and N. S. Kopeika, "Performance limitations of a free-space optical communication satellite network owing to vibrations: Heterodyne detection," *Applied Optics*, vol. 37, no. 27, pp. 6366–6374, Sep. 20, 1998, Publisher: Optica Publishing Group.

[34] K. Iwamoto, T. Nakao, T. Ito, *et al.*, "Small optical inter-satellite communication system for small and micro satellites," in *Free-Space Laser Communication and Atmospheric Propagation XXIX*, vol. 10096, SPIE, Feb. 24, 2017, pp. 212–218.

[35] H. Podmore, A. Chauhan, B. Poulsen, *et al.*, "Design and analysis of on-chip optical phase array systems for satellite communications," in *Smart Photonic and Optoelectronic Integrated Circuits 2023*, vol. PC12425, SPIE, Mar. 17, 2023, PC124250H.

[36] K. V. Acoleyen, W. Bogaerts, J. Jágerská, N. L. Thomas, R. Houdré, and R. Baets, "Off-chip beam steering with a one-dimensional optical phased array on silicon-on-insulator," *Optics Letters*, vol. 34, no. 9, pp. 1477–1479, May 1, 2009, Publisher: Optica Publishing Group.

[37] K. V. Acoleyen, H. Rogier, and R. Baets, "Two-dimensional optical phased array antenna on silicon-on-insulator," *Optics Express*, vol. 18, no. 13, pp. 13 655–13 660, Jun. 21, 2010, Publisher: Optica Publishing Group.

[38] J. K. Doylend, M. J. R. Heck, J. T. Bovington, J. D. Peters, L. A. Coldren, and J. E. Bowers, "Two-dimensional free-space beam steering with an optical phased array on silicon-on-insulator," *Optics Express*, vol. 19, no. 22, pp. 21 595–21 604, Oct. 24, 2011, Publisher: Optica Publishing Group.

[39] J. Sun, E. Timurdogan, A. Yaacobi, E. S. Hosseini, and M. R. Watts, "Large-scale nanophotonic phased array," *Nature*, vol. 493, no. 7431, pp. 195–199, Jan. 2013, Publisher: Nature Publishing Group.

[40] H. Abediasl and H. Hashemi, "Monolithic optical phased-array transceiver in a standard SOI CMOS process," *Optics Express*, vol. 23, no. 5, pp. 6509–6519, Mar. 9, 2015, Publisher: Optica Publishing Group.

[41] R. Fatemi, B. Abiri, A. Khachaturian, and A. Hajimiri, "High sensitivity active flat optics optical phased array receiver with a two-dimensional aperture," *Optics Express*, vol. 26, no. 23, p. 29 983, Nov. 12, 2018.

[42] R. Fatemi, A. Khachaturian, and A. Hajimiri, "A nonuniform sparse 2-d large-FOV optical phased array with a low-power PWM drive," *IEEE Journal of Solid-State Circuits*, vol. 54, no. 5, pp. 1200–1215, May 2019.

[43] D. R. Gozzard, L. E. Roberts, J. T. Spollard, P. G. Sibley, and D. A. Shaddock, "Fast beam steering with an optical phased array," *Optics Letters*, vol. 45, no. 13, pp. 3793–3796, Jul. 1, 2020, Publisher: Optica Publishing Group.

[44] R. Fatemi, P. P. Khial, A. Khachaturian, and A. Hajimiri, "Breaking FOV-aperture trade-off with multi-mode nano-photonic antennas," *IEEE Journal of Selected Topics in Quantum Electronics*, vol. 27, no. 1, pp. 1–14, Jan. 2021.

[45] P. A. K. Yepez, U. Scholz, J. N. Caspers, and A. Zimmermann, “Novel measures for thermal management of silicon photonic optical phased arrays,” *IEEE Photonics Journal*, vol. 11, no. 4, pp. 1–15, Aug. 2019, Conference Name: IEEE Photonics Journal.

[46] P.-A. Krochin-Yepez, U. Scholz, and A. Zimmermann, “CMOS-compatible measures for thermal management of phase-sensitive silicon photonic systems,” *Photonics*, vol. 7, no. 1, p. 6, Mar. 2020, Number: 1 Publisher: Multidisciplinary Digital Publishing Institute.

[47] Y. Wang, L. Liang, Y. Chen, *et al.*, “Improved performance of optical phased arrays assisted by transparent graphene nanoheaters and air trenches,” *RSC Advances*, vol. 8, no. 15, pp. 8442–8449, 2018, Publisher: Royal Society of Chemistry.

[48] Y. Wang, W. Shi, X. Wang, *et al.*, “Design of broadband subwavelength grating couplers with low back reflection,” *Optics Letters*, vol. 40, no. 20, p. 4647, Oct. 15, 2015.

[49] B. Cong, Y. Kong, Y. Ye, *et al.*, “A combined solution of thermoelectric coolers and microchannels for multi-chip heat dissipation with precise temperature uniformity control,” *Applied Thermal Engineering*, vol. 219, p. 119 370, Jan. 25, 2023.

[50] E.-S. Lee, J. Jin, K.-W. Chun, S.-S. Lee, and M.-C. Oh, “High-performance optical phased array for LiDARs demonstrated by monolithic integration of polymer and SiN waveguides,” *Optics Express*, vol. 31, no. 17, pp. 28 112–28 121, Aug. 14, 2023, Publisher: Optica Publishing Group.

[51] W. N. Ye, J. Michel, and L. C. Kimerling, “Athermal high-index-contrast waveguide design,” *IEEE Photonics Technology Letters*, vol. 20, no. 11, pp. 885–887, Jun. 2008, Conference Name: IEEE Photonics Technology Letters.

[52] J. H. Schmid, M. Ibrahim, P. Cheben, *et al.*, “Athermal silicon waveguides using the subwavelength grating effect,” in *Advanced Photonics (2011), paper IME3*, Optica Publishing Group, Jun. 12, 2011, IME3.

[53] J. H. Schmid, M. Ibrahim, P. Cheben, *et al.*, “Temperature-independent silicon subwavelength grating waveguides,” *Optics Letters*, vol. 36, no. 11, p. 2110, Jun. 1, 2011.

[54] M. Ibrahim, J. H. Schmid, A. Aleali, *et al.*, “Athermal silicon waveguides with bridged subwavelength gratings for TE and TM polarizations,” *Optics Express*, vol. 20, no. 16, pp. 18 356–18 361, Jul. 30, 2012, Publisher: Optica Publishing Group.

[55] H. Podmore, A. Scott, P. Cheben, *et al.*, "Athermal planar-waveguide fourier-transform spectrometer for methane detection," *Optics Express*, vol. 25, no. 26, pp. 33 018–33 028, Dec. 25, 2017, Publisher: Optica Publishing Group.

[56] W.-B. Lee, Y.-J. Kwon, D.-H. Kim, Y.-H. Sunwoo, and S.-S. Lee, "Hybrid integrated thin-film lithium niobate–silicon nitride electro-optical phased array incorporating silicon nitride grating antenna for two-dimensional beam steering," *Optics Express*, vol. 32, no. 6, pp. 9171–9183, Mar. 11, 2024, Publisher: Optica Publishing Group.

[57] Y. Kim, J.-H. Han, D. Ahn, and S. Kim, "Heterogeneously-integrated optical phase shifters for next-generation modulators and switches on a silicon photonics platform: A review," *Micromachines*, vol. 12, no. 6, p. 625, Jun. 2021, Number: 6 Publisher: Multidisciplinary Digital Publishing Institute.

[58] G. Kang, S.-H. Kim, J.-B. You, *et al.*, "Silicon-based optical phased array using electro-optic p-i-n phase shifters," *IEEE Photonics Technology Letters*, vol. 31, no. 21, pp. 1685–1688, Nov. 2019, Conference Name: IEEE Photonics Technology Letters.

[59] S. Arnon, "Use of satellite natural vibrations to improve performance of free-space satellite laser communication," *Applied Optics*, vol. 37, no. 21, pp. 5031–5036, Jul. 20, 1998, Publisher: Optica Publishing Group.

[60] S. R. Biddle, "Reliability implications of derating high-complexity microcircuits," *COTS Journal*, 2001.

[61] J. Jin, E.-S. Lee, K.-W. Chun, S.-S. Lee, and M.-C. Oh, "Practical in-situ beamforming method for optical phased array LiDAR monitoring a single far-field point," *Journal of Lightwave Technology*, vol. 43, no. 2, pp. 589–595, Jan. 15, 2025, Publisher: IEEE.

[62] J.-M. Lee, D.-J. Kim, G.-H. Kim, O.-K. Kwon, K.-J. Kim, and G. Kim, "Controlling temperature dependence of silicon waveguide using slot structure," *Optics Express*, vol. 16, no. 3, p. 1645, 2008.

[63] J.-M. Lee, D.-J. Kim, H. Ahn, S.-H. Park, and G. Kim, "Temperature dependence of silicon nanophotonic ring resonator with a polymeric overlayer," *Journal of Lightwave Technology*, vol. 25, no. 8, pp. 2236–2243, Aug. 2007, Conference Name: Journal of Lightwave Technology.

[64] K. B. Gylfason, A. Mola Romero, and H. Sohlström, "Reducing the temperature sensitivity of SOI waveguide-based biosensors," presented at the SPIE Photonics Europe, Brussels, Belgium, Jun. 1, 2012, 84310F.

[65] C. A. Papakonstantinou and R. Lee, "Effective medium theory for athermal design of bragg gratings," in *2024 Photonics North (PN)*, ISSN: 2693-8316, May 2024, pp. 1–2.

[66] F. Ashtiani and F. Aflatouni, "N × n optical phased array with 2n phase shifters," *Optics Express*, vol. 27, no. 19, p. 27 183, Sep. 16, 2019.

[67] G. Ghosh, *Handbook of Optical Constants of Solids: Handbook of Thermo-Optic Coefficients of Optical Materials with Applications*. Academic Press, Jun. 24, 1998, 337 pp.

[68] M. N. Polyanskiy, "Refractiveindex.info database of optical constants," *Scientific Data*, vol. 11, no. 1, p. 94, Jan. 18, 2024, Publisher: Nature Publishing Group.

[69] S. RYTOV, "Electromagnetic properties of a finely stratified medium," *Soviet Physics JEPT*, vol. 2, pp. 466–475, 1956.

[70] K. Oughstun and N. Cartwright, "On the lorentz-lorenz formula and the lorentz model of dielectric dispersion," *Optics Express*, vol. 11, no. 13, p. 1541, Jun. 30, 2003.

[71] L. Chrostowski and M. E. Hochberg, *Silicon photonics design*. Cambridge ; New York: Cambridge University Press, 2015, 418 pp.

[72] H. H. Li, "Refractive index of silicon and germanium and its wavelength and temperature derivatives," *Journal of Physical and Chemical Reference Data*, vol. 9, no. 3, pp. 561–658, Jul. 1, 1980.

[73] R. Soref and B. Bennett, "Electrooptical effects in silicon," *IEEE Journal of Quantum Electronics*, vol. 23, no. 1, pp. 123–129, Jan. 1987, Conference Name: IEEE Journal of Quantum Electronics.

[74] M. Nedeljkovic, R. Soref, and G. Z. Mashanovich, "Free-carrier electrorefraction and electroabsorption modulation predictions for silicon over the 1–14- \mu\hboxm infrared wavelength range," *IEEE Photonics Journal*, vol. 3, no. 6, pp. 1171–1180, Dec. 2011, Conference Name: IEEE Photonics Journal.

[75] A. W. Snyder, *Optical waveguide theory*, in collab. with J. D. Love. London ; Chapman and Hall, 1983, viii+734.

[76] P. Bienstman and R. Baets, "Optical modelling of photonic crystals and VCSELs using eigenmode expansion and perfectly matched layers," *Optical and Quantum Electronics*, vol. 33, no. 4, pp. 327–341, Apr. 1, 2001.

[77] K. Kawano and T. Kitoh, *Introduction to optical waveguide analysis: solving Maxwell's equations and the Schrödinger equation*. New York: Wiley, 2004.

[78] C. Yeh, *The essence of dielectric waveguides*, 1st ed. 2008., in collab. with F. I. Shimabukuro. New York ; Springer, 2008, 534 pp.

[79] W. J. Westerveld and H. P. Urbach, *Silicon Photonics: Electromagnetic theory*. IOP Publishing, Dec. 1, 2017.

[80] Y. A. Vlasov and S. J. McNab, "Losses in single-mode silicon-on-insulator strip waveguides and bends," *Optics Express*, vol. 12, no. 8, p. 1622, 2004.

[81] P. K. Tien, "Light waves in thin films and integrated optics," *Applied Optics*, vol. 10, no. 11, p. 2395, Nov. 1, 1971.

[82] A. Sakai, H. Go, and T. Baba, "Sharply bent optical waveguide silicon-on-insulator substrate," in *Physics and Simulation of Optoelectronic Devices IX*, vol. 4283, SPIE, Jul. 9, 2001, pp. 610–618.

[83] N. W. Ashcroft, *Solid state physics*, in collab. with N. D. Mermin. New York: Holt, Rinehart and Winston, 1976, xxi+826.

[84] H. Kogelnik and C. V. Shank, "Coupled-wave theory of distributed feedback lasers," *Journal of Applied Physics*, vol. 43, no. 5, pp. 2327–2335, May 1, 1972.

[85] T. C. Choy, *Effective Medium Theory: Principles and Applications*. Oxford University Press, Dec. 1, 2015.

[86] P. J. Bock, P. Cheben, J. H. Schmid, *et al.*, "Subwavelength grating periodic structures in silicon-on-insulator: A new type of microphotonic waveguide," *Optics Express*, vol. 18, no. 19, p. 20 251, Sep. 13, 2010.

[87] W.-P. Huang and J. Mu, "Complex coupled-mode theory for optical waveguides," *Optics Express*, vol. 17, no. 21, p. 19 134, Oct. 12, 2009.

[88] N. A. F. Jaeger, "Lecture notes on coupled mode theory," Unpublished lecture notes, CMC-UBC-Laval SiEPIC Passives Workshop — ELEC 582/GEL 7070, 2024.

[89] A. Yariv, "Coupled-mode theory for guided-wave optics," *IEEE Journal of Quantum Electronics*, vol. 9, no. 9, pp. 919–933, Sep. 1973, Conference Name: IEEE Journal of Quantum Electronics.

[90] Z. Zhu and T. Brown, "Full-vectorial finite-difference analysis of microstructured optical fibers," *Optics Express*, vol. 10, no. 17, p. 853, Aug. 26, 2002.

[91] J.-P. Berenger, "A perfectly matched layer for the absorption of electromagnetic waves," *Journal of Computational Physics*, vol. 114, no. 2, pp. 185–200, Oct. 1994.

[92] Lumerical. "INTERCONNECT: Time and frequency domain simulation of bidirectional, multimode and multichannel circuit topologies." (), [Online]. Available: https://www.lumerical.com/learn/whitepapers/interconnect-time-and-frequency-domain-simulation-of-bidirectional-multimode-and-multichannel-circuit-topologies/ (visited on 01/31/2025).

[93] Microchem. "SU-8 3000," Kayaku. (), [Online]. Available: https://kayakuam.com/products/su-8-3000/ (visited on 07/18/2024).

[94] Thorlabs. "Thorlabs - g608n3 index matching gel, 3 cc syringe." (), [Online]. Available: https://www.thorlabs.com/thorproduct.cfm?partnumber=G608N3 (visited on 07/18/2024).

[95] A. Milton and W. Burns, "Mode coupling in optical waveguide horns," *IEEE Journal of Quantum Electronics*, vol. 13, no. 10, pp. 828–835, Oct. 1977.

[96] Y. Fu, T. Ye, W. Tang, and T. Chu, "Efficient adiabatic silicon-on-insulator waveguide taper," *Photonics Research*, vol. 2, no. 3, A41, Jun. 1, 2014.

[97] P. Sethi, A. Haldar, and S. K. Selvaraja, "Ultra-compact low-loss broadband waveguide taper in silicon-on-insulator," *Optics Express*, vol. 25, no. 9, pp. 10 196–10 203, May 1, 2017, Publisher: Optica Publishing Group.

[98] P. Sethi and S. K. Selvaraja, "Alignment-tolerant broadband compact taper for low-loss coupling to a silicon-on-insulator photonic wire waveguide," *Applied Optics*, vol. 58, no. 23, pp. 6222–6227, Aug. 10, 2019, Publisher: Optica Publishing Group.

[99] J. Zhang, J. Yang, H. Xin, J. Huang, D. Chen, and Z. Zhaojian, "Ultrashort and efficient adiabatic waveguide taper based on thin flat focusing lenses," *Optics Express*, vol. 25, no. 17, p. 19 894, Aug. 21, 2017.

[100] D. F. G. Gallagher and T. P. Felici, "Eigenmode expansion methods for simulation of optical propagation in photonics: Pros and cons," presented at the Integrated Optoelectronics Devices, Y. S. Sidorin and A. Tervonen, Eds., San Jose, CA, Jun. 17, 2003, p. 69.

[101] R. Hansen, *Phased Array Antennas*, 1st ed. John Wiley & Sons, Ltd, 2009, _eprint: https://onlinelibrary.wiley.com/doi/pdf/10.1002/9780470529188.

[102] Y. Guo, Y. Guo, C. Li, H. Zhang, X. Zhou, and L. Zhang, "Integrated optical phased arrays for beam forming and steering," *Applied Sciences*, vol. 11, no. 9, p. 4017, Jan. 2021, Number: 9 Publisher: Multidisciplinary Digital Publishing Institute.

[103] K. Shang, C. Qin, Y. Zhang, *et al.*, "Uniform emission, constant wavevector silicon grating surface emitter for beam steering with ultra-sharp instantaneous field-of-view," *Optics Express*, vol. 25, no. 17, p. 19 655, Aug. 21, 2017.

[104] T. Tamir and S. T. Peng, "Analysis and design of grating couplers," *Applied physics*, vol. 14, no. 3, pp. 235–254, Nov. 1, 1977.

[105] L. Cheng, S. Mao, Z. Li, Y. Han, and H. Y. Fu, "Grating couplers on silicon photonics: Design principles, emerging trends and practical issues," *Micromachines*, vol. 11, no. 7, p. 666, Jul. 2020, Number: 7 Publisher: Multidisciplinary Digital Publishing Institute.

[106] C. R. Doerr, L. Chen, Y.-K. Chen, and L. L. Buhl, "Wide bandwidth silicon nitride grating coupler," *IEEE Photonics Technology Letters*, vol. 22, no. 19, pp. 1461–1463, Oct. 2010.

[107] X. Chen, K. Xu, Z. Cheng, C. K. Y. Fung, and H. K. Tsang, "Wideband subwavelength gratings for coupling between silicon-on-insulator waveguides and optical fibers," *Optics Letters*, vol. 37, no. 17, p. 3483, Sep. 1, 2012.

[108] A. Mekis, S. Gloeckner, G. Masini, *et al.*, "A grating-coupler-enabled CMOS photonics platform," *IEEE Journal of Selected Topics in Quantum Electronics*, vol. 17, no. 3, pp. 597–608, May 2011.

[109] R. Orobtchouk, A. Layadi, H. Gualous, D. Pascal, A. Koster, and S. Laval, "High-efficiency light coupling in a submicrometric silicon-on-insulator waveguide," *Applied Optics*, vol. 39, no. 31, pp. 5773–5777, Nov. 1, 2000, Publisher: Optica Publishing Group.

[110] P. F. Wang, G. Z. Luo, H. Y. Yu, *et al.*, "Improving the performance of optical antenna for optical phased arrays through high-contrast grating structure on SOI substrate," *Optics Express*, vol. 27, no. 3, p. 2703, Feb. 4, 2019.

[111] P. Cheben, D.-X. Xu, S. Janz, and A. Densmore, "Subwavelength waveguide grating for mode conversion and light coupling in integrated optics," *Optics Express*, vol. 14, no. 11, p. 4695, 2006.

[112] D. Melati, M. K. Dezfouli, Y. Grinberg, *et al.*, "Design of compact and efficient silicon photonic micro antennas with perfectly vertical emission," *IEEE Journal of Selected Topics in Quantum Electronics*, vol. 27, no. 1, pp. 1–10, Jan. 2021.

[113] S. Khajavi, D. Melati, P. Cheben, *et al.*, "Compact and highly-efficient broadband surface grating antenna on a silicon platform," *Optics Express*, vol. 29, no. 5, p. 7003, Mar. 1, 2021.

[114] S. Khajavi, D. Melati, P. Cheben, J. H. Schmid, C. A. A. Ramos, and W. N. Ye, "Highly efficient ultra-broad beam silicon nanophotonic antenna based on near-field phase engineering," *Scientific Reports*, vol. 12, no. 1, p. 18 808, Nov. 5, 2022, Number: 1 Publisher: Nature Publishing Group.

[115] M. Raval, C. V. Poulton, and M. R. Watts, "Unidirectional waveguide grating antennas with uniform emission for optical phased arrays," *Optics Letters*, vol. 42, no. 13, p. 2563, Jul. 1, 2017.

[116] A. Beling and J. C. Campbell, "Advances in photodetectors and optical receivers," in *Optical Fiber Telecommunications*, Elsevier, 2013, pp. 99–154.

[117] Y. Tang, X. Yi, and W. Shieh, "Optical performance monitoring for coherent optical systems," in *Optical Performance Monitoring*, Elsevier, 2010, pp. 351–383.

[118] D. Patel, S. Ghosh, M. Chagnon, *et al.*, "Design, analysis, and transmission system performance of a 41 GHz silicon photonic modulator," *Optics Express*, vol. 23, no. 11, p. 14 263, Jun. 1, 2015.

[119] G. Zheng, J. Xu, L. Chen, H. Wang, and W. She, "Athermal design for the potassium titanyl phosphate electro-optical modulator," *Applied Optics*, vol. 46, no. 27, pp. 6774–6778, Sep. 20, 2007, Publisher: Optica Publishing Group.

[120] B. Guha, B. B. C. Kyotoku, and M. Lipson, "CMOS compatible athermal silicon microring resonators," *Optics Express*, vol. 18, no. 4, p. 3487, Feb. 15, 2010.

[121] P. Steglich, C. Mai, C. Villringer, and A. Mai, “Direct observation and simultaneous use of linear and quadratic electro-optical effects,” *Journal of Physics D: Applied Physics*, vol. 53, no. 12, p. 125 106, Jan. 2020, Publisher: IOP Publishing.